UNIVERSIDAD DE BUENOS AIRES
Facultad de Ciencias Exactas y Naturales
Departamento de Matemática

Métodos numéricos acelerados de alta precisión para problemas de scattering por superficies y colecciones de partículas—incluyendo anomalías de Wood

Tesis para optar al título de Doctor de la Universidad de Buenos Aires
en el área Ciencias Matemáticas

Lic. Martín Maas

Director de Tesis: Dr. Oscar Bruno
Director asistente: Dr. Francisco Grings
Consejero de estudios: Dr. Diego Rial

Lugar de trabajo: Instituto de Astronomía y Física del Espacio (UBA-CONICET)

Buenos Aires, 2018

Agradecimientos

Esta tesis es el resultado de múltiples esfuerzos y de valiosas fuentes de motivación y entusiasmo.

En primer lugar, quisiera agradecer a Oscar, bajo cuya orientación paciente y generosa pude desarrollar este trabajo y completar así mi formación científica—su pasión por la matemática y su perseverante búsqueda de la excelencia siempre me inspirará.

A los investigadores y becarios del grupo de teledetección del IAFE: Francisco Grings, Haydeé Karzembaum, Matías Barber, Mariano Franco, Cintia Bruscantini, Verónica Barraza, David "Wally" Rava, Esteban Roitberg, Mercedes Salvia, Federico Carballo, Ana Dogliotti y Juan Ignacio Gossn; grupo en el cual hemos compartido, junto con distintos colegas y amigos como Esteban Calzetta y Julio Jacobo Berlles, diversos proyectos en torno a los satélites argentinos de observación científica, así como animadas charlas sobre el sistema científico y el plan espacial nacional. Finalmente, a la memoria de un ser muy querido por todos y pionero de la actividad espacial en Argentina, Antonio Gagliardini, cuyas tempranas palabras de que en Argentina estaba todo por hacerse han sabido inspirar a una generación de científicos y profesionales a lo largo del país.

A los que nos hemos reunido en Buenos Aires en torno a las ecuaciones integrales y el scattering, en especial al Prof. Gabriel Acosta y a Juan Pablo Borthagaray, por la fructífera colaboración matemática que hemos sostenido y que considero sumamente valiosa, así como a Juan Domingo Gonzáles y a Edmundo Lavia, por nuestra colaboración en éste caso más incipiente.

A los compañeros y amigos que he podido visitar en Pasadena, para compartir unos muy valiosos meses en un entorno de una enorme libertad intelectual, entusiasmo y optimismo: Edwin Jimenez, Carlos Perez-Arancibia, Agustın Fernandez-Lado, Emmanuel Garza-Gonzales, Eldar Akhmet-galiyev y Thomas Anderson -

Al Prof. Diego Rial, mi consejero de estudios del Departamento de Matemática, y a los miembros del Jurado: los Profesores Ricardo Durán, Claudio Padra y Fabio Zyserman, por su interés en éste trabajo y sus valiosas sugerencias.

Por último, pero no menos importante, quisiera agradecer a mi familia, por su aliento y continuo apoyo durante todos estos años. A Flor, mi compañera en el amor y los proyectos: gracias por comprender y compartir conmigo tantas cosas como trae la vida—incluyendo esta tesis.

Métodos numéricos acelerados de alta precisión para problemas de scattering por superficies y colecciones de partículas—incluyendo anomalías de Wood

Resumen

Esta tesis introduce metodologías matemáticas y computacionales eficientes para el tratamiento de problemas de dispersión de ondas electromagnéticas por superficies rugosas y colecciones de partículas, con el objetivo de poder predecir la energía retrodispersada o emitida por medios naturales complejos—como la superficie del océano o los suelos agrícolas vegetados—en función de los ángulos de incidencia, longitudes de onda y polarizaciones. El objetivo de la presente tesis es, precisamente, desarrollar algoritmos que posibiliten la aplicación de la simulación numérica en configuraciones realistas, y así colaborar con la eliminación de discordancias entre teorías desarrolladas bajo suposiciones simplificadoras y las observaciones generadas en el área de teledetección en microondas. Los sucesivos capítulos de esta tesis introducen aspectos matemáticos y computacionales relativos a (1) Problemas de scattering en configuraciones periódicas; (2) Desarrollo y análisis de métodos basados en ecuaciones integrales para problemas que incluyen el Laplaciano fraccionario, y (3) Problemas de scattering electromagnéticos y acústicos en configuraciones tridimensionales.

El método de aceleración introducido en la presente tesis provee una nueva representación, basada en transformadas rápidas de Fourier (FFT), métodos espectrales de integración y ciertas "fuentes equivalentes desplazadas" que, por primera vez, ha permitido el tratamiento rápido y a alto orden para problemas periódicos *bajo cualquier frecuencia espacial* k*, incluyendo a las llamadas Anomalías de Wood.* Este método, que permite resolver problemas de muy grandes tamaños acústicos o eléctricos, no sufre de las importantes restricciones y deterioro que resultan de la existencia de las anomalías de Wood—y, por lo tanto, se puede aplicar con toda generalidad y con muy alta precisión, en tiempos de cómputo muy reducidos.

Por otro lado, el estudio del Laplaciano Fraccionario presentado en esta tesis introduce ciertas ecuaciones integrales asociadas que, según mostramos, están relacionadas con problemas de scattering por estructuras infinitamente delgadas. De este modo, este trabajo extiende ciertas ideas centrales en el área de ecuaciones integrales a otras áreas de aplicación. Las soluciones del Laplaciano Fraccionario desarrollan singularidades en los bordes del dominio, lo que ha ocasionado, así como en el caso análogo en electromagnetismo, dificultades en su resolución numérica y en la teoría de regularidad asociada. En particular, la tesis presenta un método numérico que converge *exponencialmente rápido* mientras que el previo estado del arte provee un orden de convergencia lineal. El análisis de regularidad de las soluciones para este problema involucra, entre otras metodologías, el uso de ciertos espacios de funciones (introducidos por Babuška y Guo en 2002) que no habian sido considerados previamente en el contexto del Laplaciano Fraccionario.

Finalmente, la tesis presenta un algoritmo aplicable a problemas de scattering electromagnético en configuraciones tridimensionales, que inlcuyen tanto superficies aleatorias como partículas que modelan elementos de vegetación. En gerenal, el conjunto de estos esfuerzos ha dado lugar a colaboraciones con investigadores en diversas áreas de aplicación, las cuales se mencionan, junto a planes para trabajos futuros, en el capítulo final de la tesis.

High order fast numerical methods for scattering problems by periodic surfaces and groups of particles—including Wood Anomalies

Abstract

This thesis introduces efficient mathematical and computational methodologies for the treatment of problems of scattering of electromagnetic waves by rough surfaces and groups of particles, with applicability to evaluation of energy backscattered or emitted by complex natural media—such as oceanic surfaces or vegetated agricultural soils—as a function of incidence angles, wavelengths and polarizations. The goal of this thesis is to develop algorithms that enable the accurate numerical simulation of realistic configurations, and thus, the elimination of discrepancies between theories developed under simplifying assumptions and observations generated in the area of microwave remote sensing. The successive chapters of this thesis introduce mathematical and computational aspects concerning (1) Scattering problems in periodic configurations; (2) Development and analysis of methods based on integral equations for problems concerning the Fractional Laplacian operator, and (3) Problems of electromagnetic and acoustic scattering in three-dimensional configurations.

The acceleration method introduced in this thesis provides a new representation, based on fast Fourier transforms (FFT), spectral integration methods and certain "shifted equivalent sources", which, for the first time, have allowed rapid and high order treatment of periodic problems *under any spatial frequency* k*, including so-called Wood Anomalies.* This method, which enables solution of problems of very large electrical sizes, does not suffer from the important restrictions and deterioration that result from the existence of Wood anomalies—and, therefore, can be applied with all generality, in computing times of the order of seconds and with very high accuracies.

On the other hand, the study concerning the Fractional Laplacian operator presented in this thesis introduces certain associated integral equations that, as we show, are related to problems of scattering by infinitely thin structures. Therefore, this work extends central ideas in the area of integral equations to other application areas. As it is known, the solutions of the Fractional Laplacian equations develop singularities at the edges of the domain, which causes, as in the analogous electromagnetic case, certain difficulties in their numerical solution and in the associated regularity theory. In particular, the thesis presents a numerical method for this problem that converges *exponentially fast*—while the previous state of art provides a linear convergence order only. The analysis of the regularity of solutions for this problem involves, among other tools, the use of certain function spaces (introduced by Babuška and Guo in 2002) that had not previously been considered in the context of the Fractional Laplacian.

Finally, the thesis presents an algorithm applicable to problems of electromagnetic scattering in three-dimensional configurations including both random surfaces and particles that model vegetation elements. In general, all these efforts have given rise to a series of collaborations with researches in relevant application areas, which are mentioned, along plans for future work, in the concluding chapter of this thesis.

Contents

Chapter 1

Introduction

In view of its great relevance in science and technology, studies of interactions of waves and structures have been vigorously pursued for several centuries. A variety of highly significant mathematical contributions in this area have been produced over the years, the most remarkable of which may be Maxwell's prediction of the existence of radio waves preceding their experimental observation. The solution of Maxwell's and related propagation, emission and scattering equations for electromagnetic, acoustic and elastic waves—possibly involving complex, realistic configurations under prescribed frequencies and polarizations—is often beyond the reach of even the most powerful supercomputers. The aim of this thesis is precisely to put forth highly efficient scattering solvers, thereby enabling solution of Maxwell's and related equations for the highly challenging scattering configurations that arise in applications.

A specific point of focus of the present thesis relates to the remarkable case of diffraction first observed by Prof. Wood in 1902 [80], subsequently referred to as "Wood anomalies" since no theoretical explanation could initially be provided. The mathematical treatment by Rayleigh in 1907 [66] produced an initial attempt at explaning these observations, by characterizing what are now known as Wood-Rayleigh anomalies. As it shall be mentioned in the present introduction, those configurations give rise to significant mathematical and computational challenges. The goal to resolve these difficulties has lead us to the development the efficient algorithms, presented in this thesis, for the prediction of the behavior of electromagnetic waves in complex and realistic natural and man-made configurations.

1.1 Historical overview of wave scattering

1.1.1 Early days of optics and acoustics

The theoretical study and practical utilization of optics and acoustics can be traced back to antiquity. The theory of geometrical optics, initiated by Euclid and Ptolemy, represents light as rays emanating from stars and, even, according to Plato (in his extramission theory), emanating from the eyes. The geometrical-optics theory then provided a satisfactory explanation of the focusing and magnification effects that take place as polished-crystal lenses are used to focus light—either as a fire-starting

method or as a rudimentary visual aid (Fig 1.1.1.a). The wave nature of sound was much better understood at that early time, as illustrated by the ideas of Aristotle, who suggested that sound consists of compressions and rarefactions of air which "falls upon and strikes the air which is next to it...". Not surprisingly, this early theoretical understanding had a practical counterpart, as is perhaps best illustrated by the work of the Roman architect and engineer Vitruvius, who wrote a treatise on the acoustic properties of theaters, including discussion of interference, echoes, and the placement of echeas—an echea (literally echoer), was a pot that is remarkably similar in function to a modern-day bass trap: the vases operated by resonance, enhancing key frequencies of the performers' voices and absorbing those of the audience.

(a) (b) (c) (d)

Figure 1.1.1: (a) The Nimrud lens is a 3000-year-old piece of rock crystal, which may have been used as a magnifying glass or as a burning glass to start fires. (b) The so called "reading stones" were introduced in the 8th century by Addas Ibn Firnas (c) Eyeglasses were invented in Pisa around 1290 (d) Galileo's original telescope, which he created in 1609 and could mangify objects 20 times, was also the first one to be pointed at the stars.

The evolution of optical theory has been in close connection with its applications, which were in turn constrained by the known manufacturing techniques, most notably, by the state of which the craft (and later the industry) of glass-making was developed at any given point in history. Historians have often referred to glass as the Roman plastic [53], as during that period it turned from a luxurious into a commonly available material, which was manufactured dominantly in colorless form. While serving mostly ornamental purposes, the first glass prisms also appeared around that time. The use of glass as a visual aid started in the 8th century, when the so-called reading stones (Fig 1.1.1.b), which were placed on top of text in order to magnify the letters, are believed to have been introduced by the Andalusian inventor Addas Ibn Firnas [25]. Around that time, the Muslim scholar Alhazen explained, for the first time [49], that vision occurs when light bounces on an object and then is directed to one's eyes. Ibn Sahl had already discovered the law of refraction (or Snell-Descartes law) by the 11th century, which he employed in the design of several lens shapes. The eyeglasses or spectecles were invented in northern Italy by about 1290 (Fig 1.1.1.c). As the optical theory of the time could not even explain how the eyeglasses could correct presbyopia or myopia (the first sucessful explanation of this phenomena is contained in Kepler's 1604 contibution Ad Vitellionem paralipomena), the development, mastery, and experimentation with lenses proceeded in a slow but steady empirical fashion. Subsequent development in the optical industry of grinding and polishing lenses, eventually lead to the invention of the optical microscope around 1595, and the refracting

telescope in 1608, both of which appeared in the Netherlands. A much improved version of the telescope, which could magnify objects 20 times instead of the previous 3, was produced by Galileo (Fig 1.1.1.d), who was also the first person to point a telescope at the stars.

1.1.2 The wave equation and wave theory of light: diffraction

The seventeenth century saw significant advances in optics and acoustics. Newton's developed his theory of light and colors, which was still largely based on rectilinear movement of light particles, by experimenting with prisms. By separating the colors with a first prism and combining them again into white light with a second prisms (Fig.1.1.2.a), he came to the conclusion that colors were already present in white light, and that the prisms didn't create the colors. He thus coined the word "spectrum" (appearance in Latin) to refer to the colors. The term diffraction, from the Latin "diffringere" (to break into pieces), was coined by Francesco Maria Grimaldi in the early seventeenth century, as he was able to demonstrate experimentally that light, as it passed through a hole, was far from moving in a rectilinear path but rather it took on the shape of a cone (Fig.1.1.2.b).

(a) (b)

Figure 1.1.2: (a) Newton used two prisms to show that light contains multiple "spectra". (b) One of Grimaldi's experiment, as depicted in this 1665 volume [26]: when light passes through a hole, the illuminated area IK is larger than the geometrical prediction.

In 1678, in an attempt to explain the phenomena of diffraction of light, Huygens was the first to propose that light behaved as a wave; in particular, he proposed the idea that every point to which a luminous disturbance reaches becomes a source of a spherical wave, and that the sum of these secondary waves determines the form of the wave at any subsequent time. However, the wave theory of light was largely disregarded, perhaps due to the imposing scientific stature of Isaac Newton, who supported the particulate theory. In this state of affairs, it was not optics but acoustics and vibration, which provided the motivation in the 18th century for D'alambert and Euler to study the the wave equation

$$u_{tt} = c^2 \Delta u \tag{1.1.1}$$

which is the first partial differential equation (PDE) that appeared in history. They obtained several important results which are, however, not related to Huygens' principle.

The standing of the wave theory in optics started to turn with Thomas Young's famous experiment in 1803 (Fig.1.1.3.a), where by passing light through two closely spaced slits and explaining

his observations by interference of the waves emanating from the two slits, he deducted that light must propagate as waves. It took several decades until Augustin Fresnel demonstrated in 1819 that diffraction can indeed be explained by applying Huygens' principle and Young's principle of interference of light waves. In particular, Fresnel was able to deduce that the diffracted field or "perturbance" could be expressed entirely in terms of an integral along the diffracting surface of some "diffraction coefficient" multiplied by a spherical point source located at the point of integration:

$$u(\mathbf{x}) = \int_S \mu(\mathbf{y}) \frac{e^{ik|\mathbf{x}-\mathbf{y}|}}{|\mathbf{x}-\mathbf{y}|} dSy, \tag{1.1.2}$$

where x is a point located away from the diffracting surface. This representation, now known as the Huygens-Fresnel principle (1.1.2), was difficult to apply in practice. (As we shall see, integral representations including (1.1.2) still provides the basis of some of today's most efficient numerical methods for wave problems.) As described in [31], in order to obtain analytical results that matched known experimental facts, Fresnel's had to resort to several ad-hoc procedures in the determination of the unknown coefficients $\mu(y)$. A remarkable fact ocurred when he submitted his work to the French Academy of Sciences: his paper was at first dismissed by Poisson, one of the members of the jury who defended the particle theory, who noted that the mathematical framework put forth by Fresnel implied the presence of a bright spot in the shadow area behind a circular disc, a fact which completely defeated common sense. Another member of the jury, Arago, then performed an experiment that confirmed the existence of this very spot in practice (Fig.1.1.3.b), thus providing a spectacular validation of the wave theory.

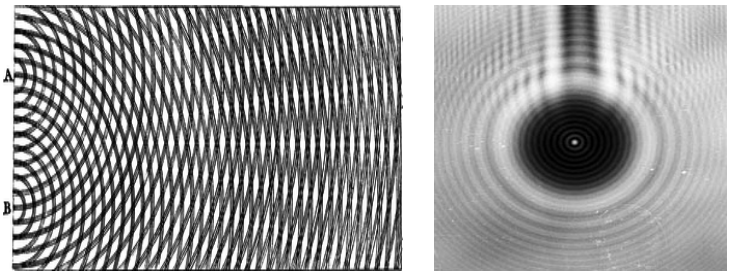

(a) (b)

Figure 1.1.3: (a) Thomas Young's diagram of his double-slit diffraction experiment (b Arago spot: laser shadow of a ball bearing suspended on a needle.

The theory of diffraction of light was put on a firm mathematical footing, on the basis of the wave equation (1.1.1), thanks to the work of Helmholtz and Kirchhoff. Around 1859, Helmholtz considered time-harmonic waves of the form $u(x,t) = e^{i\omega t}\phi(x)$, which, upon replacement in (1.1.1), lead to the equation for the field ϕ that now bears his name:

$$\Delta\phi + k^2\phi = 0, \quad \text{where} \quad k = \frac{\omega}{c}. \tag{1.1.3}$$

Importantly, Helmholtz obtained the integral representation formula

$$u(\mathbf{x}) = \frac{1}{4\pi}\int_S \frac{\partial}{\partial n}\left(\frac{e^{ik|\mathbf{x}-\mathbf{y}|}}{|\mathbf{x}-\mathbf{y}|}\right) u(\mathbf{y}) - \left(\frac{e^{ik|\mathbf{x}-\mathbf{y}|}}{|\mathbf{x}-\mathbf{y}|}\right) \frac{\partial}{\partial n} u(\mathbf{y}) dS(\mathbf{y}), \tag{1.1.4}$$

a relation that can be established on the basis of Green's identities [29], and thus provided, for the first time, a deduction of a form of the Huygens-Fresnel principle directly from the wave equation. Note that the quantities u and $\frac{\partial}{\partial n}u$ under the integral sign are still difficult to determine in practice. However, unlike Fresnel's "diffraction coefficients" μ in (1.1.2), the unknown fields u and $\frac{\partial}{\partial n}u$ are themselves *physical* fields that relate to u in an explicit manner. On the basis of this observation, and utilizing a simple ansatz known as the "tangent plane approximation" (that expresses the field u and its normal derivative at a point $\mathbf{x}$ on the surface S as it would result from an approximation of S by the tangent plane at $\mathbf{x}$), in 1882 Kirchhoff obtained an approximate integral expression for the field u that results throughout space as the surface S is illuminated by a given incident field. Further, as detailed in [10], employing an additional "high-frequency" ($k \to \infty$) asymptotic approximation of the resulting integral expression, currently known as the "stationary phase" approximation, celebrated closed-form expressions result for the diffracted field in various configurations of practical interest. These expressions were significantly more accurate than all previous approximations; Kirchhoff's ansatz continues to inspire both physics-based and numerical solution strategies for scattering problems.

1.1.3 Maxwell's equations and electromagnetic waves

In the meantime, the seemingly disconnected developments on electricity and magnetism were unified by James Clerk Maxwell. Maxwell's contributions during 1861 and 1862 introduce his celebrated system of differential equations, which in modern notation can be expressed in the form

$$\begin{cases} \nabla \cdot \mathbf{D} &= \rho \\ \nabla \times \mathbf{H} &= \mathbf{J} + \frac{\partial \mathbf{D}}{\partial t} \\ \nabla \times \mathbf{E} &= \frac{\partial \mathbf{B}}{\partial t} \\ \nabla \cdot \mathbf{B} &= 0 \end{cases} \tag{1.1.5}$$

In a non-ferromagnetic material or vacuum (or, more precisely, in a linear paramagnetic medium) of permittivity ε and permeability μ, we have $\mathbf{D} = \varepsilon\mathbf{E}$ and $\mathbf{B} = \mu\mathbf{H}$. In the absence of charges and currents ($\rho = 0$ and $\mathbf{J} = 0$), further, (1.1.5) leads to

$$\frac{\partial^2 \mathbf{E}}{\partial t^2} = c^2 \nabla \times \nabla \times \mathbf{E}, \qquad \text{where} \quad c = (\varepsilon\mu)^{-1/2}. \tag{1.1.6}$$

This equation admits (vectorial) plane-wave solutions of the form

$$\mathbf{E}(\mathbf{x}, t) = \mathbf{A}e^{-i\omega t}e^{i\mathbf{k}\cdot\mathbf{x}}, \qquad \text{such that} \quad |\mathbf{k}| = \frac{\omega}{c} \qquad \text{and} \quad \mathbf{A} \cdot \mathbf{k} = 0, \tag{1.1.7}$$

where the orthogonal vectors $\mathbf{A}$ and $\mathbf{k}$ denote the direction of oscillation and propagation, respectively. This led Maxwell to conjecture the existence of electromagnetic waves, and, in view of their speed of propagation in vacuum (which, he observed, numerically equals the speed of propagation of light) to suggest that light is itself an electromagnetic wave. In 1888, Hertz published his experimental discovery of such (transverse) electromagnetic waves, which propagated at the same speed as light, thus placing Maxwell's theory on a firm experimental footing. From a mathematical

standpoint, given suitable boundary conditions that depend on material properties, the old problem of evaluating the diffraction of light had been finally cast in terms of well-defined boundary value problem—which in fact coincides with the then-newly-discovered, much more general, framework of electromagnetic wave theory.

Maxwell's equations in the frequency domain

It will be useful to express the fields **E** and **H** in terms of corresponding frequency domain quantities $E(\mathbf{x},\omega)$ and $H(\mathbf{x},\omega)$, which are related to **E** and **H** via the Fourier transformation

$$\mathbf{E}(\mathbf{x},t)=\frac{1}{2\pi}\int_{-\infty}^{\infty}e^{-i\omega t}E(\mathbf{x},\omega)d\omega \qquad \text{and} \qquad \mathbf{H}(\mathbf{x},t)=\frac{1}{2\pi}\int_{-\infty}^{\infty}e^{-i\omega t}H(\mathbf{x},\omega)d\omega, \tag{1.1.8}$$

with analogous expressions for **J**, **D** and **B**. In paramagnetic dielectric media with frequency-dependent properties (conductivity, permittivity and permeability), we have the relations

$$J(x,\omega)=\sigma(\omega)E(\mathbf{x},\omega), \qquad D(\mathbf{x},\omega)=\varepsilon_b(\omega)E(\mathbf{x},\omega) \qquad \text{and} \qquad B(\mathbf{x},\omega)=\mu(\omega)H(\mathbf{x},\omega). \tag{1.1.9}$$

Throghout this thesis the time-hamonic fields for a fixed value of ω

$$\begin{cases} \mathbf{E}(\mathbf{x},t) & = e^{-i\omega t}E(\mathbf{x},\omega) \\ \mathbf{H}(\mathbf{x},t) & = e^{-i\omega t}H(\mathbf{x},\omega) \end{cases} \tag{1.1.10}$$

are considered, and, for notational simplicity the letter ω and the oscillatory factor $e^{-i\omega t}$ are suppressed from the notation. To maintain common practice, the vectors $E(\mathbf{x},\omega)$ and $H(\mathbf{x},\omega)$ (as well as their incident, scattered and transmitted counterparts) are not displayed in boldface: they are, in fact, the only vector quantities in this thesis to which this exception applies. Maxwell's equations (1.1.5) then simplify to

$$\begin{cases} \nabla\times H & = -i\omega\left(\varepsilon_b(\omega)+\frac{i\sigma(\omega)}{\omega}\right)E \qquad & \nabla\cdot E & = 0 \\ \nabla\times E & = i\omega\mu(\omega)H & \nabla\cdot H & = 0 \end{cases}$$

which leads to the equations

$$-\nabla\times\nabla\times E+\left(\varepsilon_b(\omega)+\frac{i\sigma(\omega)}{\omega}\right)\mu(\omega)\omega^2E=0, \quad \text{and} \quad \nabla\cdot E=0 \tag{1.1.11}$$

for the electric field E, and to similar equations for the magnetic field H. Note that the left hand equation in (1.1.11) is of very similar form to the Helmholtz equation (1.1.3), with Δu replaced by $-\nabla\times\nabla\times E=(\Delta E-\nabla\mathrm{div}E)$ (which, in view of the right-hand equation in (1.1.11), actually coincides with ΔE), and with a complex wavenumber

$$k^2(\omega)=\left(\varepsilon_b(\omega)+\frac{i\sigma(\omega)}{\omega}\right)\mu(\omega)\omega^2, \tag{1.1.12}$$

—which reflects the finitely conducting character of the material under consideration. The function

$$\varepsilon(\omega)=\varepsilon_b(\omega)+\frac{i\sigma(\omega)}{\omega} \tag{1.1.13}$$

is interchangeably called the permittivity or the (complex) dielectric constant. In practice, the function $\varepsilon(\omega)$ is most often obtained for each medium by careful measurement processes (but, more and more frequently, at present, computational modeling from first principles can also be found). Some cases of particular interest in the framework of remote sensing are the dielectric properties of soil and ocean water, which are reported, for instance, in [36] and [58], respectively.

Special single-frequency "plane-wave" solutions of equation (1.1.11) are given by the relations

$$E(\mathbf{x},t) = \mathbf{A}e^{i\mathbf{k}(\omega)\cdot\mathbf{x}}, \quad \text{where} \quad \mathbf{k}(\omega)\cdot\mathbf{k}(\omega) = k^2(\omega), \quad \text{and} \quad \mathbf{A}\cdot\mathbf{k}(\omega) = 0, \tag{1.1.14}$$

(note that here $\mathbf{k}(\omega)\cdot\mathbf{k}(\omega) = k_1^2+k_2^2+k_3^2$ denotes a complex-valued scalar product). The wavelength λ of the oscillations (which represents one period of spatial oscillation) depends only on the real part of $k(\omega)$, while the degree of attenuation usually represented by the "skin depth" δ (defined as the depth below the conducting surface at which the field intensity has fallen by a factor of $1/e = 1/2.71... \approx 0.37$) depends on the imaginary part of k. In terms of wavelength and skin depth, we have

$$\mathrm{Re}(k(\omega)) = \frac{2\pi}{\lambda} \qquad \text{and} \qquad \mathrm{Im}(k(\omega)) = \frac{1}{\delta}. \tag{1.1.15}$$

Remark 1.1.1. *There are of course two important limiting cases regarding the imaginary part of the dielectric constant, namely 1) it is close to zero (very low conductivity), and 2) it is close to the perfect conductor limit $\sigma = \infty$. In the first limit the dielectric constant is real, and, therefore, a "lossless" medium (without attenuation). In the second case the skin depth is zero—which implies that the electromagnetic field equals zero inside the material.*

Unique solutions of the Maxwell's equations are determined when appropriate interface/boundary conditions (typically concerning the "illumination" of the "scatterer" by an "incident field") are prescribed. We consider first the most general interface between two dielectric materials. Given a field (E^{inc}, H^{inc}) incident from the exterior of a domain D, and denoting by (E^{scat}, H^{scat}) and (E^{trans}, H^{trans}) the fields that are scattered to the exterior of D and transmitted into the interior of D, respectively, the dielectric boundary conditions are given by continuity of the tangential components of the total electric and magnetic fields, that is to say,

$$\nu \times (E^{inc} + E^{scat}) = \nu \times E^{trans} \tag{1.1.16}$$

$$\nu \times (H^{inc} + H^{scat}) = \nu \times H^{trans}. \tag{1.1.17}$$

In the case of perfectly conducting materials we have $E^{trans} = H^{trans} = 0$ (see Remark 1.1.1), and, thus, the total field by $E = E^{inc}+E^{scat}$ can be determined uniquely [28] by specifying the boundary condition

$$\nu \times E = 0. \tag{1.1.18}$$

Integral representation formulas analogous to that of Helmholtz (1.1.4) for (vectorial) electromagnetic fields were not available until 1939, when Stratton and Chu published their celebrated contribution [74]. The integral representations formulae we use are presented in Section 1.1.4 below.

Scattering by translation invariant (two-dimensional) geometries

When the geometry of a problem is translation-invariant in a given direction, say, the $\hat{y}$ direction, the Maxwell's equations become two-dimensional, and they thereby simplify considerably. Indeed, under translation invariance we have $\frac{\partial}{\partial y}(E, H) = 0$, which, as we shall see, give rise to two decoupled boundary-value problems, one for each "polarization" TE and TM. These two solutions can be combined to solve problems of scattering by the structure with incidences with arbitrary polarization, thus completely characterizing the problem of scattering.

In the TE (transverse electric) case, both the incident and scattered electric fields point in the "horizontal" direction $\hat{y}$ (so that the TE case is sometimes referred to as the "HH" case). As the total electric field does not depend on y, we have

$$\mathbf{E}^{inc} = \hat{y}\psi^{inc}(x, z) \quad \text{and} \quad \mathbf{E} = \hat{y}\psi(x, z) \tag{1.1.19}$$

When Ω is a perfect conductor, the corresponding boundary condition is

$$\nu \times \mathbf{E} = 0 \tag{1.1.20}$$

So, for the total electric field we have

$$\begin{cases} \Delta\psi + k^2\psi &= 0 \quad \in \Omega^C \\ \psi &= 0 \quad \in \partial\Omega \end{cases} \tag{1.1.21}$$

The magnetic field can be recovered from the curl of the electric field, leading to expressions for every component of the electromagnetic field $(\mathbf{E}, \mathbf{H})$.

In the TM (transverse magnetic) or VV case, in turn, the magnetic field points towards the direction $\hat{y}$. This is the other possible polarization which is parallel to the symmetry plane of the surface. We have

$$\mathbf{H}^{inc} = \hat{y}\psi^{inc}(x, z) \quad \text{and} \quad \mathbf{H} = \hat{y}\psi(x, z) \tag{1.1.22}$$

So the electric field is given by

$$-iw\epsilon^{+}\mathbf{E} = \hat{x}\left(-\frac{\partial\psi}{\partial z}\right) + \hat{z}\frac{\partial\psi}{\partial z} \tag{1.1.23}$$

In the perfectly conducting case, the boundary condition (1.1.20) leads to

$$\nu \times \left(-\hat{x}\frac{\delta\psi}{\delta z} + \hat{z}\frac{\partial\psi}{\partial z}\right) = -\hat{y}\left(n_x\frac{\partial\psi}{\partial x} + n_z\frac{\partial\psi}{\partial z}\right) = -\hat{y}\frac{\partial\psi}{\partial n} = 0 \tag{1.1.24}$$

so we arrive at the equation

$$\begin{cases} \Delta\psi + k^2\psi &= 0 \quad \in \Omega^C \\ \frac{\partial\psi}{\partial\nu} &= 0 \quad \in \partial\Omega \end{cases} \tag{1.1.25}$$

where ψ is, in this case, the total magnetic field.

In the case of a dielectric interface, and it is easily shown that the following equations are to be solved

$$\left\{\begin{array}{rcll} \Delta\psi_1 + k_1^2\psi_1 &=& 0 & \in \Omega_1 \\ \Delta\psi_2 + k_2^2\psi_2 &=& 0 & \in \Omega_2 \\ \psi_1 &=& \psi_2 & \in S \\ \frac{\partial\psi_1}{\partial\nu} &=& \rho\frac{\partial\psi_2}{\partial\nu} & \in S \end{array}\right. \quad f \tag{1.1.26}$$

with $\rho = 1$ in the TE case (corresponding to H polarization), or $\rho = \frac{k_1}{k_2}$ in TM (vertical polarization).

1.1.4 Green functions and integral equations

The method of boundary integral equations is based on integral representations of the solutions u to various equations that arise in mathematical physics. The basis of such formulations is the free-space Green function for the Helmholtz equation

$$G(r) = \left\{\begin{array}{ll} \frac{e^{ikr}}{r} & r \in \mathbb{R}^3 \\ H_0^1(kr) & r \in \mathbb{R}^2 \quad \text{and } k > 0 \\ \log(r) & r \in \mathbb{R}^2 \quad \text{and } k = 0. \end{array}\right. \tag{1.1.27}$$

In the case of the Helmholtz equation (1.1.3), the solutions can be represented in terms of the acoustic single or double layer potential operators

$$S[\mu](x) = \int_{\partial D} G(x - x')\mu(x')dS' \tag{1.1.28}$$

$$D[\mu](x) = \int_{\partial D} \frac{\partial G(x - x')}{\partial\nu(x')}\mu(x')dS', \tag{1.1.29}$$

that is, one might seek solutions to a boundary value problem, for example, in the form of a Double Layer potential

$$u(x) = D[\mu](x), \qquad x \in \mathbb{R}^3 \setminus D. \tag{1.1.30}$$

Upon imposing boundary conditions on the surface ∂D and careful evaluation of the quantity $D[\mu](x)$ for $x \in \partial D$, an integral equation is obtained. The evaluation of singular integral operators such as (1.1.28) for values of $x \in \partial D$ is carried out by means of the following

Theorem 1.1.2 (Jump Relations)**.** *Let ∂D be of class C^2 and μ continuous. Then the single and double layer potentials S and D, and their corresponding normal derivatives satisfy*

$$S(\mu)(x) = \int_{\partial D} \mu(y)\Phi(x, y)ds(y), \qquad x \in \partial D \tag{1.1.31}$$

$$\frac{\partial}{\partial\nu}S(\mu)_\pm(x) = \int_{\partial D} \mu(y)\frac{\partial\Phi(x, y)}{\partial\nu(x)}ds(y) \mp \frac{1}{2}\mu(x), \qquad x \in \partial D \tag{1.1.32}$$

$$D(\mu)_\pm(x) = \int_{\partial D} \mu(y)\frac{\partial\Phi(x, y)}{\partial\nu(y)}ds(y) \pm \frac{1}{2}\mu(x), \qquad x \in \partial D \tag{1.1.33}$$

$$\frac{\partial}{\partial\nu}D(\mu) = \int_{\partial D} \mu(y)\frac{\partial^2\Phi(x, y)}{\partial\nu(x)\partial\nu(y)}ds(y) \qquad x \in \partial D \tag{1.1.34}$$

where

$$\frac{\partial}{\partial \nu} S(\mu)_{\pm}(x) := \lim_{h \to 0} \nu(x) \cdot \nabla S(\mu)(x \pm h\nu(x))$$
$$D(\mu)(x)_{\pm}(x) := \lim_{h \to 0} D(\mu)(x \pm h\nu(x))$$

In the electromagnetic case, in turn, electric or magnetic fields can be represented in terms of various potential operators. For example, we have the magnetic field operator and the electric field operator

$$\mathcal{M}[a](x) = \nabla \times \int_{\partial D} G(x - x') a(x') dS' \tag{1.1.35}$$

$$\mathcal{E}[e](x) = \nabla \times \nabla \times \int_{\partial D} G(x - x') e(x') dS' \tag{1.1.36}$$

$$\tag{1.1.37}$$

which satisfy analogous properties to those of the scalar case [60], and lead to various integral equation formulations when imposing boundary conditions (1.1.16) or (1.1.18).

1.2 Electromagnetic scattering by periodic structures

1.2.1 Diffraction gratings

By passing sunlight through a bird feather and observing a resulting rainbow pattern, James Gregory is credited with the discovery of the diffraction grating in 1673. The first man-made diffraction grating, in turn, was made around 1785 by David Rittenhouse, who strung 50 hairs between two finely threaded screws, with an approximate spacing of about 40 lines per centimeter. However, it was not until Fraunhofer's work that diffraction gratings acquired a significant stand in science and technology. Fraunhofer (who started working as an apprentice to a glass-maker when he orphaned at 11 years old) was engaged in the development of perhaps the most striking applications of early 19th century optics. His various inventions, ranging from glass grinding and polishing machines, to several precision optical instruments, placed his native Bavaria at the center of the optics industry of the day. In particular, Fraunhoffer built the first wire diffraction grating in 1821, which created a thinly spaced periodic array of slits. Using his device in conjunction with a telescope, Fraunhofer found out that the spectra of Sirius and other first-magnitude stars differed from the sun and from each other, thus founding the field of stellar spectroscopy.

Diffraction gratings, and more generally, scattering by periodic structures containing surfaces and arrays of particles, are the main problem that is considered in this thesis.

1.2.2 The Rayleigh Expansion above the grooves

The first theoretical studies of scattering by such structures are due to Lord Rayleigh. His "Theory of Sound" published in 1896 [65] contains an analysis of scattering of an acoustic (scalar) plane

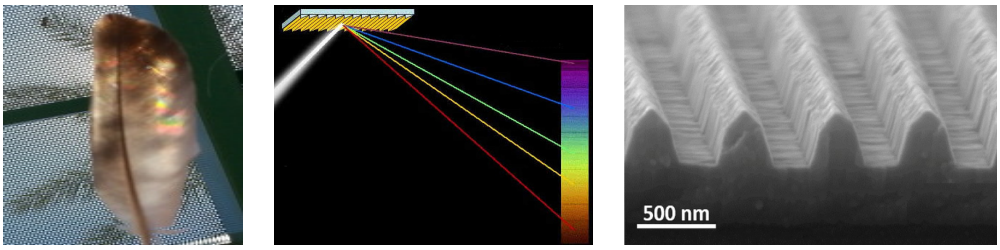

(a) (b) (c)

Table 1.2.1: (a) The first observation of a diffraction grating was made by James Gregory in 1673, by passing sunlight through a bird feather. (b) Diffraction gratings were later manufactured with the purpose of decomposing light in specific ways. (c) Micrograph of a translation-invariant reflective diffraction grating

wave, incident on a grating with a sinusoidal translation-invariant (two-dimensional) profile. In that contribution, Rayleigh considered the problem

$$\begin{cases} \Delta u^{scat} + k^2 u^{scat} = 0 & \text{when} \quad y > f(x) \\ u^{scat} = e^{i(\alpha x + \beta y)} & \text{when} \quad y = f(x) \\ u^{scat} \text{ satisfies a radiation condition as } y \to \infty \end{cases} \tag{1.2.1}$$

for a given plane-wave incident field of wavenumber $k = \omega/c$ incoming at an angle θ (so that the incident wave-vector is given by $(\alpha, \beta) = k(\sin(\theta), -\cos(\theta))$), and where f is a periodic function of period d (Rayleigh assumed $f(x) = \sin(x)$).

Central to Rayleigh's contribution was an expansion of the solution of (1.2.1) which now bears his name. In what follows, we briefly outline how Rayleigh's expansion can be obtained, following [64, Sect. 1.2.3]. In general, the prescribed boundary values (given by the incident wave $e^{ik(\alpha x+\beta y)}$ at $y = f(x)$) is not a periodic function of x, but it satisfies a property known as α-quasiperiodicity. A function $F(x)$ or $F(x, y)$ is said to be α-quasiperiodic in x with period d when it satisfies the relation

$$F(x, y) = T(x, y)e^{i\alpha x} \quad \text{where } T \text{ is a periodic function of } x, \tag{1.2.2}$$

or, equivalently, when it satisfies $F(x + d, y) = F(x, y)e^{-i\alpha d}$ for all $x \in \mathbb{R}$. As it can be easily checked, the function $u^{scat}(x + d, y)e^{-i\alpha d}$ is also a solution of (1.2.1). Thus, assuming uniqueness of solutions for that boundary value problem, the two solutions must coincide, and the solution u^{scat} itself must be is α-quasiperiodic: $u^{scat}(x, y) = T(x, y)e^{i\alpha x}$ for some x-periodic function T. Replacing the x-Fourier-expansion of T we obtain

$$u^{scat}(x, y) = \sum_{n=-\infty}^{\infty} t_n(y)e^{i\alpha_n x} \quad \text{where} \quad \alpha_n = \alpha + n\frac{2\pi}{d}, \tag{1.2.3}$$

where $t(y)$ are the Fourier coefficients of $T(x, y)$. Then, multiplying by $e^{-i\alpha x}$ and replacing (1.2.3) in (1.2.1) we obtain

$$\sum_{n=-\infty}^{\infty} \left[\frac{\partial^2}{\partial y^2} t_n(y) + (k^2 - \alpha_n^2) t_n(y) \right] e^{in\frac{2\pi}{d}x} = 0 \quad \text{for} \quad y > f(x). \tag{1.2.4}$$

Clearly, this equation is valid for all x provided $y > \max_{x\in(0,d)} f(x)$, and thus it follows that the Fourier series in x must have null coefficients. Solving the resulting ODE in the y variable leads to

$$t_n(y) = A_n e^{-i\beta_n y} + B_n e^{i\beta_n y} \qquad \text{if} \qquad y > \max_{x\in(0,d)} f(x), \tag{1.2.5}$$

where, letting U denote the finite set of integers n such that $k^2 - \alpha_n^2 > 0$ and using the positive branch of the square root, the values of β_n are given by

$$\beta_n := \begin{cases} \sqrt{k^2 - \alpha_n^2} & , \quad n \in U \\ i\sqrt{\alpha_n^2 - k^2} & , \quad n \notin U. \end{cases} \tag{1.2.6}$$

As the expression $e^{-i\beta_n y}$ is unbounded when $n \notin U$, and it represents an incident plane-wave towards the gratings, so in order to satisfy the radiation condition, $A_n = 0$. Therefore, we have the Rayleigh expansion

$$u^{scat}(x,y) = \sum_{n=-\infty}^{\infty} B_n e^{i\alpha_n x + i\beta_n y} \quad \text{for} \quad y > \max_{x\in(0,d)} f(x). \tag{1.2.7}$$

This expression can be interpreted in the following way. For $n \in U$, the functions $e^{i\alpha_n x + i\beta_n y}$ correspond to propagating waves. For $n \notin U$, the functions $e^{i\alpha_n x + i\beta_n y}$ are damped exponentially, and are thus referred to as evanescent waves. In particular, the famous grating formula for the angles of the propagating waves (which was already known to Fraunhofer)

$$\sin(\theta_n) = \sin(\theta) + n\lambda d, \tag{1.2.8}$$

follows directly from the interpretation of α_n and β_n in (1.2.7) as angles.

An aspect of particular relevance, besides the purely geometrical arguments given above, is the value of the coefficients B_n of the Rayleigh expansion. On the basis of these coefficients, for each $n \in U$, we define the associated *efficiency* as

$$e_n = \frac{\beta_n}{\beta}|B_n|^2. \tag{1.2.9}$$

This quantity represents the fraction of energy that is reflected in the n-th propagating mode. It can be shown that (via a simple integration argument [64, Sect. 1.2.6]), for a perfectly conducting surface, the finite set of all efficiencies satisfies the energy balance criterion

$$\sum_{n\in U} e_n = 1. \tag{1.2.10}$$

For a given numerical method, the following quantity, known as the "energy error"

$$\varepsilon = 1 - \sum_{n\in U} e_n \tag{1.2.11}$$

is often used to address its accuracy.

1.2.3 Wood Anomalies

The term "Wood-anomaly" relates to experimental observations reported by Wood in 1902. In [80], he details:

> On mounting the grating oll the table of a spectrometer I was astounded to find that under certain conditions the drop from maximum illumination to minimum, a drop certainly of from 10 to 1, occurred within a range of wave-lengths not greater than the distance between the sodium lines (...) A change of wavelength of 1/1000 is then sufficient to cause the illumination in the spectrum to chauge from a maximum to a minimum.

The first attempt at explaining this phenomena was made by Rayleigh in 1907 [66], where he states:

> "Prof. Wood describes the extraordinary behavior of a certain grating ruled upon speculum metal which exhibits what may almost be called discontinuities in the distribution of the brightness of its spectra. (...) at the time of reading the original paper I was inclined to think that the determining circumstance might perhaps be found in the passing off of a spectrum of higher order"

Rayleigh's observation refers to the case when a certain mode in the expansion (1.2.7) gets, as the problem parameters such as the wavelength or the incidence angle are modified, a coefficient $\beta_n = 0$. In such case, the function $e^{i\alpha_n x + i\beta_n y} = e^{i\alpha_n x}$ becomes a grazing plane wave (i.e. a wave that propagates parallel to the grating). Precisely around those points, Rayleigh conjectured and verified to a 5% accuracy using Prof. Wood's data, that large changes in the value of the efficiencies e_n could take place even when the changes in the wavelength are very small.

To illustrate the mathematical and computational difficulties that arise in relation with Wood-Rayleigh anomalies, let's consider the Green function of the problem, or the quasi-periodic Green function, which is a distribution that satisfies

$$\Delta G^{qper}(x) + k^2 G^{qper}(x) = \delta_y \tag{1.2.12}$$

together with a radiation condition at infinity, and α-quasi-periodicity ($G^{qper}(x,y) = T(x,y)e^{i\alpha x}$ for a certain x-periodic function T). Fourier analysis techniques very similar to those in the previous section (see [64, Sect. 1.2.9] for details) allow to reach the following expression for G^{qper}

$$G^{qper}(X,Y) = \frac{i}{2d} \sum_{n \in \mathcal{Z}} \frac{e^{i\alpha_n X + i\beta_n |Y|}}{\beta_n}. \tag{1.2.13}$$

Remark 1.2.1. *It is important to note that, for parameter values such that a grazing wave ($\beta_n = 0$) exists in this series, the series acquires an infinite coefficient and, thus, G^{qper} is not defined.*

Remark 1.2.2. *As pointed out in [56], it would be more appropriate to refer to the phenomenon as Wood-Rayleigh anomalies and frequencies, but, subsequently in this thesis, we use the Wood anomaly nomenclature in keeping with common practice [11, 57, 73].*

Certain aspects could not be fully explained by Rayleigh's theory, beyond its 5% accuracy. In particular, Rayleigh's theory made no reference to polarization, and Wood had noted that this sharp drops in certain efficiencies only took place for vertically polarized incident waves. Subsequent experimental and theoretical work led to the discovery and characterization of other "Anomalies" (sharp and sudden changes in efficiencies around certain problem parameters) in both polarizations. This non-Rayleigh anomalies do depend on the shape and properties of the scattering surface. While this thesis mainly focuses on Wood-Rayleigh anomalies (which, as pointed out in Remark 1.2.2, we will reefer to simple as Wood Anomalies) we have included some discussion about non-Rayleigh anomalies in Section 5.1.

1.3 Computational methods for problems of scattering by periodic and bi-periodic structures in $\mathbb{R}^d$ ($d = 2, 3$).

The problem of scattering by rough surfaces has received considerable attention over the last few decades in view of its significant importance from scientific and engineering viewpoints. Unfortunately, however, the numerical solution of such problems has generally remained quite challenging. For example, the evaluation of rough-surface scattering at grazing angles has continued to pose severe difficulties, as do high-frequency problems including deep corrugations and/or large periods, and problems at Wood-anomaly frequencies, most notably for bi-periodic structures in $\mathbb{R}^3$. (As mentioned in Section 1.2.3 above, at Wood frequencies the classical quasi-periodic Green Function ceases to exist, and associated Green-function summation methods such as those employed in [7, 24, 51] become inapplicable.) In spite of significant progress in the general area of scattering by periodic surfaces [6, 11, 15, 17, 22, 34, 52, 70], methodologies which effectively address the various aforementioned difficulties for realistic configurations have remained elusive.

The Wood-anomaly problem, which includes the famously problematic grazing-angle-incidence case, has historically presented significant challenges. As indicated in Chapter 4, Wood anomalies are specially pervasive in three-dimensional configurations, and they have therefore significantly curtailed solution of periodic scattering problems in that higher dimensional context. The extension [22] of the shifted Green function approach to three-dimensions gave rise, for the first time, to solvers which are applicable to Wood-frequency doubly periodic scattering problems in three-dimensional space. (An alternative approach to the Wood anomaly problem for two-dimensions was introduced in [11], but the three-dimensional, bi-periodic version [52] of that approach is restricted to frequencies away from Wood anomalies.) The contribution [22] does not include an acceleration procedure, and it can therefore prove exceedingly expensive—except when applied to relatively simple configurations.

In order to address this significant difficulty, the present thesis proposes a new fast and accurate integral-equation methodology which addresses these challenges in both the two- and three-dimensional cases. The method proceeds by introducing the notion of "shifted equivalent sources", which extends the applicability of the FFT-based acceleration approach [18] to the context of the Wood-anomaly capable two- and three-dimensional shifted Green functions [15, 22]. In the two-

dimensional context, single-core runs in computing times ranging from a fraction of a second to a few seconds suffice for the proposed algorithm to produce highly-accurate solutions in some of the most challenging configurations arising in applications, even at Wood frequencies. Short computing times also suffice for the new algorithms to treat large and complex three-dimensional configurations.

1.4 Integral-equation methods for the Fractional Laplacian

Another point of emphasis of the present thesis is the development and analysis of numerical methods of fast convergence for steady-state fractional diffussion problems. As we shall discuss in the present section, these problems are closely related to problems of scattering by infinitely thin structures, thus allowing the extension of certain central ideas in potential theory and integral equation theory to this highly-active application area.

According to the the long jump random walk approach to the Fractional Laplacian [78], the Fractional Laplacian operator $(-\Delta)^s$ corresponds, from a probabilistic point of view, to the infinitesimal generator of a stable Lévy process, where jumps of arbitrarily long distances are allowed. Lemma 3.2.3 of Chapter 3 shows that, in the case $s = \frac{1}{2}$, the steady-state fractional diffusion problem in (a, b) can be expressed as the integral equation

$$\frac{1}{\pi}\frac{d}{dx}\int_a^b \ln|x-y|\frac{d}{dy}u(y)dy = f(x) \tag{1.4.1}$$

which, surprisingly, coincides with the problem of zero-frequency scattering by an infinitely thin slab in $\mathbb{R}^2$, located in $(a, b) \times \{0\}$, posed in terms of the hypersingular operator $\frac{\partial}{\partial\nu}D$ introduced in section 1.1.4. This analogy motivates the generalization of previous successful approaches for the treatment of problems of scattering by infinitely thin structures, to this new area. For $s \neq \frac{1}{2}$, the integral equations provided by the aforementioned Lemma 3.2.3 are given by

$$C_s\frac{d}{dx}\int_a^b |x-y|^{1-2s}\frac{d}{dy}u(y)dy = f(x). \tag{1.4.2}$$

The development and analysis of high order numerical methods for this problems is quite challenging: in fact, as is detailed in the Section 1.4.1, prior to the present contribution (see also our related work [4]), the accuracy of previously existing algorithms for this problem was limited to first order [3]. The analysis developed in Chapter 3 lead to a Gegenbauer-based Nyström discretization that, in particular, converges *exponentially fast* for analytic right-hand sides. The overall strategy used to accomplish this is summarized in Section 1.4.2.

1.4.1 Previous work

Various numerical methods have been proposed recently for equations associated with the Fractional Laplacian $(-\Delta)^s$ in bounded domains. Restricting attention to one-dimensional problems, Huang and Oberman [44] presented a numerical algorithm that combines finite differences with a quadrature rule in an unbounded domain. Numerical evidence provided in that paper for smooth

right-hand sides (cf. Figure 7(b) therein) indicates convergence to solutions of (3.1.1) with an order $\mathcal{O}(h^s)$, in the infinity norm, as the mesh-size h tends to zero (albeith orders as high as $\mathcal{O}(h^{3-2s})$ are demonstrated in that contribution for singular right-hand sides f that make the solution u smooth). Since the order s lies between zero and one, the $\mathcal{O}(h^s)$ convergence provided by this algorithm can be quite slow, specially for small values of s. D'Elia and Gunzburger [33], in turn, proved convergence of order $h^{1/2}$ for a finite-element solution of an associated one-dimensional nonlocal operator that approximates the one-dimensional fractional Laplacian. These authors also suggested that an improved solution algorithm, with increased convergence order, might require explicit consideration of the solution's boundary singularities.

The contribution [3], finally, studies the regularity of solutions of the Dirichlet problem (3.1.1) and it introduces certain graded meshes for integration in one- and two-dimensional domains. The rigorous error bounds and numerical experiments provided in [3] demonstrate an accuracy of the order of $h^{1/2}|\log h|$ and $h|\log h|$ for all s, in certain weighted Sobolev norms, for solutions obtained by means of uniform and graded meshes, respectively.

Difficulties in the numerical treatment of the Dirichlet problem (3.1.1) stem mainly from the singular character of the solutions of this problem near boundaries. A recent regularity result in this regards was provided in [67]. In particular, this contribution establishes the global Hölder regularity of solutions of the general n-dimensional version of equation (3.1.1) ($n \geq 1$) and it provides a certain boundary regularity result: the quotient $u(x)/\omega^s(x)$ remains bounded as $x \to \partial\Omega$, where ω is a smooth function that behaves like $\text{dist}(x, \Omega^c)$ near $\partial\Omega$. This result was then generalized in [41], where, using pseudo-differential calculus, a certain regularity result is established in terms of Hörmander μ-spaces: in particular, for the regular Sobolev spaces $H^r(\Omega)$, it is shown that if $f \in H^r(\Omega)$ for some $r > 0$ then the solution u may be written as $w^s\phi + \chi$, where $\phi \in H^{r+s}(\Omega)$ and $\chi \in H_0^{r+2s}(\Omega)$. Interior regularity results for the Fractional Laplacian and related operators have also been the object of recent studies [5, 30].

Remark 1.4.1. *A number of operators related to $(-\Delta)^s$ have been considered in the mathematical literature. Here we mention the so called* spectral *fractional Laplacian $\mathcal{L}_s$, which is defined in terms of eigenfunctions and eigenvalues (v_n, λ_n)* of the standard Laplacian $(-\Delta)$ operator with Dirichlet boundary conditions in $\partial\Omega$*: $\mathcal{L}_s[v_n] = \lambda_n^s v_n$. The operator $\mathcal{L}_s$ is different from $(-\Delta)^s$— since, for example, $\mathcal{L}_s$ admits smooth eigenfunctions (at least for smooth domains) Ω while $(-\Delta)^s$ does not; see [72]. A finite element approach for problems concerning the operator $\mathcal{L}_s$ was proposed in [62] on the basis of extension ideas first introduced in [23] for the operator $(-\Delta)^s$ in $\mathbb{R}^n$ which were subsequently developed in [13] for the bounded-domain operator $\mathcal{L}_s$. As far as we know, however, approaches based on extension theorems have not as yet been proposed for the Dirichlet problem* (3.1.1).

1.4.2 Overall solution strategy and associated regularity theory

The proposed approach for the fractional-Laplacian algorithm is based on use of a factorization of solutions as a product of a certain (explicit) edge-singular weight ω times a "regular" unknown.

That is, we seek a decomposition of the solution u to equations (1.4.1) and (1.4.2) in the form

$$u(x) = \omega(x)\phi(x), \tag{1.4.3}$$

so as to incorporate the explicit weight $\omega(x)$ analytically into an associated quadrature-based numerical method for the smooth solution ϕ—instead of directly solving for u. The performance of such methods depends on the regularity of ϕ, instead of that of u. In particular, if the edge-singularity is characterized to all orders (i.e. the weight ω is determined so that $\phi(x)$ has a maximum degree of regularity), the numerical methods associated with this analysis can be expected to perform in a higly efficient manner. This simple argument provides the link between the design of high-order numerical methods and the development of regularity theory.

In order to proceed with this plan, the first few Sections in Chapter 3 present an asymptotic analysis—that leads to a complete characterization of the singular weight ω, with a specific singular exponent, and which, for example, yields an infinitely differentiable factor ϕ for infinitely differentiable right hand side, for all values of the Laplacian exponent s. More generally, this study gives rise to a sharp characterization of the smoothness of the regular unknown ϕ in various function spaces (including adequately chosen weighted Sobolev spaces, spaces of analytic functions, and classical regularity). This analysis is based on use of a full eigendecomposition for a certain *weighted integral operator*, in terms of the aforementioned Gegenbauer polynomial basis.

The sharp error estimates presented in Chapter 3 allow us to ensure that the proposed Gegenbauer-Nyström algorithm is spectrally accurate, with convergence rates that only depend on the smoothness of the right-hand side. In particular, the exponentially fast convergence (resp. faster than any power of the mesh-size) for analytic (resp. infinitely smooth) right-hand sides is rigorously established and verified by means of an efficient numerical implementation.

1.5 Content and Layout of the thesis

This thesis introduces efficient mathematical and computational methodologies for the treatment of problems of mathematical-physics via integral equations techniques. The thesis is organized as follows.

Chapter 2 studies scattering problems in periodic two-dimensional configurations. After some preliminary results regarding the "quasi-periodic shifted Green functions" G_j^{qper}, a hybrid strategy to evaluate G_j^{qper} is presented, that converges exponentially fast for most of the required points, and algebraically fast (at a user-prescribed order) for the remainder. After a suitable high-order discretization strategy is presented and its convergence properties discussed, the proposed acceleration method is introduced. This acceleration algorithm provides a new representation, based on fast Fourier transforms (FFT), spectral integration methods and certain "shifted equivalent sources", which, for the first time, have allowed rapid and high order treatment of periodic problems *under any spatial frequency* k, *including Wood Anomalies*. This method, which enables solution of problems of very large electrical sizes, does not suffer from the restrictions and deterioration that

result from the presence of Wood anomalies—and, therefore, can be applied with all generality, in computing times of the order of seconds and with very high accuracies.

Chapter 3 studies integral equations methods for the Fractional Laplacian operator. We first introduce certain associated integral equations that, as we show, are related to problems of scattering by infinitely thin structures. As is known, the solutions of the Fractional Laplacian equations develop singularities at the edges of the domain, which causes, as in analogous electromagnetic case, difficulties in its numerical solution and in the associated regularity theory. In particular, the thesis presents a numerical method for this problem that converges *exponentially fast*—while the previous state of art provides a linear convergence order. The analysis of the regularity of solutions for this problem involves the use of certain function spaces (introduced by Babuska and Guo in 2002) that had not previously been considered in the context of the Fractional Laplacian. In this way, the proposed method enables the solution, in computing times of hundredths of a second, of problems for which other recent approaches would provide significantly lower accuracies in computing times of the order of several minutes.

Chapter 4 concerns electromagnetic scattering problems in bi-periodic three-dimensional configurations, which include both random surfaces (such as oceanic or bare agricultural soils) and a combination of surfaces with particles that model vegetation elements (such as the case of vegetated agricultural soils). A variety of numerical results presented in that chapter demonstrate the efficiency of the proposed approach.

Chapter 5, finally, outlines certain related contributions and collaborations that developed around the present work, some of which represent a part of an ongoing long-term and broadly multidisciplinary collaboration that is expected to be continue as part of the future work of the author of this thesis.

Chapter 2

Fast periodic-scattering Nyström solvers in 2D, including Wood anomalies

2.1 Introduction

This chapter introduces a fast algorithm, applicable throughout the electromagnetic spectrum, for the numerical solution of problems of scattering by periodic surfaces in two-dimensional space. In particular, the proposed algorithm remains highly accurate and efficient for challenging configurations including randomly rough surfaces, deep corrugations, large periods, near grazing incidences, and, importantly, Wood-anomaly resonant frequencies. The proposed approach is based on use of certain "shifted equivalent sources" which enable FFT acceleration of a Wood-anomaly-capable quasi-periodic Green function introduced recently [15]. The Green-function strategy additionally incorporates an exponentially convergent shifted version of the classical *spectral* series for the Green function. Finally, use of specialized high order Nyström quadrature rules together with the iterative linear algebra solver GMRES [69] complete the proposed methodology. Single-core runs of this algorithm in computing times ranging from a fraction of a second to a few seconds suffice for the proposed algorithm to produce highly-accurate solutions in some of the most challenging contexts arising in applications. The algorithm is additionally demonstrated for certain extreme geometries featuring hundreds of wavelengths in period and/or depth, for which accurate solutions are obtained in single-core runs of the order of a few minutes.

This Chapter is organized as follows: after the problem parameters are laid down in Section 2.2, Section 2.3 describes the shifted Green function method [15, 22], and it introduces a hybrid spatial-spectral strategy for the efficient evaluation of the shifted Green function itself. Our high order quadrature rules and their use of the hybrid evaluation strategy are put forth in Section 2.4. Section 2.5 then introduces the central concepts of this chapter, namely, the shifted-equivalent-source concept and the associated FFT acceleration approach. Section 2.6 demonstrates the new overall methodology by means of a variety of applications, including, e.g., grazing-angle problems for large

and very rough random Gaussian surfaces whose solutions, including near-field evaluation and display, are produced in computing times that grow only sub-linearly with the size of the problem. In practice, computing times of the order of a few seconds suffice for random rough-surface problems usually considered in the literature, and a few minutes are required for extreme cases—such as a Gaussian surface one-thousand wavelengths in period and fourteen wavelengths in peak-to-peak height. Other general diffraction-grating problems at Wood anomalies are also considered in this section; once again typical problems of interest are tackled by the new method in computing times ranging from a fraction of a second to a few seconds with full single-precision accuracy. Thus, the method is general and highly competitive for both Wood and non-Wood frequencies alike. Section 2.7, finally, provides a few concluding remarks.

2.2 Problem setup

We consider the problem of scattering of a transverse electric incident electromagnetic wave of the form $u^{inc}(x,y) = e^{\mathrm{i}(\alpha x - \beta y)}$ by a perfectly conducting periodic surface $\Gamma = \{(x, f(x)), x \in \mathbb{R}\}$ in two-dimensional space, where f is a smooth periodic function of period d: $f(x+d) = f(x)$. Letting $\mathrm{k}^2 = \alpha^2 + \beta^2$, the scattered field u^{scat} satisfies

$$\begin{cases} \Delta u^{scat} + \mathrm{k}^2 u^{scat} = 0 & \text{in} \quad \Omega_f^+ \\ u^{scat} = -u^{inc} & \text{in} \quad \Gamma, \end{cases} \tag{2.2.1}$$

where $\Omega_f^+ = \{(x,y) : y > f(x)\}$. The incidence angle $\theta \in (-\frac{\pi}{2}, \frac{\pi}{2})$ is defined by $\alpha = \mathrm{k}\sin(\theta)$ and $\beta = \mathrm{k}\cos(\theta)$. As was discussed in Section 1.2.2, the scattered field u^{scat} is quasi-periodic and, for all (x,y) such that $y > \max_{x\in\mathbf{r}} f(x)$, it can be expressed in terms of the Rayleigh expansion (1.2.7).

2.3 Shifted Green function

As shown in [15, 22], a suitable modification of the Green function (1.2.13) which does not suffer from the difficulties mentioned in Remark 1.2.1, and which is therefore valid throughout the spectrum, can be introduced on the basis of a certain "shifting" procedure related to the method of images. In what follows, the construction [15] of a multipolar or "shifted" quasi-periodic Green function is reviewed briefly, and a new hybrid spatial-spectral strategy for its evaluation is presented.

2.3.1 Quasi-periodic multipolar Green functions

Rapidly decaying multipolar Green functions G_j of various orders j can be obtained as linear combinations of the regular free-space Green function G with arguments that include a number j of shifts. For example, we define a multipolar Green function of order $j = 1$ by

$$G_1(X,Y) = G(X,Y) - G(X,Y+h) \tag{2.3.1}$$

This expression provides a Green function for the Helmholtz equation, valid in the complement of the shifted-pole set $P_1 = \{(0,-h)\}$, which decays faster than G (with order $|X|^{-\frac{3}{2}}$ instead of

$|X|^{-\frac{1}{2}}$) as $X \to \infty$—as there results from a simple application of the mean value theorem and the asymptotic properties of Hankel functions [48].

A suitable generalization of this idea, leading to multipolar Green functions with arbitrarily fast algebraic decay [15], results from application of the finite-difference operator $(u_0, \ldots, u_j) \to \sum_{\ell=0}^{j} (-1)^\ell \binom{j}{\ell} u_\ell$ ($j \in \mathbb{N}$) that, up to a factor of $1/h^j$, approximates the j-th order Y-derivative operator [47, eq. 5.42]. For each non-negative integer j, the resulting multipolar Green functions G_j of order j is thus given by

$$G_j(X,Y) = \sum_{m=0}^{j} (-1)^m C_m^j \, G(X, Y + mh), \quad \text{where} \quad C_m^j = \binom{j}{m} = \frac{j!}{m!(j-m)!}. \tag{2.3.2}$$

Clearly, G_j is a Green function for the Helmholtz equation in the complement of the shifted-pole set

$$P_j = \{(X,Y) \in \mathbb{R}^2 : (X,Y) = (0, -mh) \text{ for some } m \in \mathbb{Z} \text{ with } 1 \le m \le j\}. \tag{2.3.3}$$

As shown in [15], further, for Y bounded we have

$$G_j(X,Y) \sim |X|^{-q} \text{ as } X \to \infty, \quad \text{with} \quad q = \frac{1}{2} + \left\lfloor \frac{j+1}{2} \right\rfloor, \tag{2.3.4}$$

where $\lfloor x \rfloor$ denotes the largest integer less than or equal to x.

For sufficiently large values of j, the spatial lattice sum

$$\tilde{G}_j^{qper}(X,Y) = \sum_{n=-\infty}^{\infty} e^{-\mathrm{i}\alpha n d} G_j(X + nd, Y) \tag{2.3.5}$$

provides a rapidly (algebraically) convergent quasi-periodic Green function series defined for all (X,Y) outside the periodic shifted-pole lattice

$$P_j^{qper} = \{(X,Y) \in \mathbb{R}^2 : (X,Y) = (nd, -mh) \text{ for some } n, m \in \mathbb{Z} \text{ with } 1 \le m \le j\}. \tag{2.3.6}$$

The Rayleigh expansion of $\tilde{G}_j^{qper}$, further, can be readily obtained by applying equation (1.2.13); the result is

$$\tilde{G}_j^{qper}(X,Y) = \sum_{n=-\infty}^{\infty} \frac{\mathrm{i}}{2d\beta_n} e^{\mathrm{i}\alpha_n X} \left(\sum_{m=0}^{j} (-1)^m C_m^j e^{\mathrm{i}\beta_n |Y + mh|} \right) \qquad \text{for } Y \neq -mh, \quad 0 \le m \le j. \tag{2.3.7}$$

And, using the identity $\sum_{m=0}^{j} (-1)^m C_m^j e^{\mathrm{i}\beta_n (Y+mh)} = e^{\mathrm{i}\beta_n Y}(1 - e^{\mathrm{i}\beta_n h})^j$ there results

$$\tilde{G}_j^{qper}(X,Y) = \sum_{n=-\infty}^{\infty} \frac{\mathrm{i}}{2d\beta_n} (1 - e^{\mathrm{i}\beta_n h})^j e^{\mathrm{i}\alpha_n X + \mathrm{i}\beta_n Y} \qquad \text{for } Y > 0. \tag{2.3.8}$$

As anticipated, no problematic infinities occur in the Rayleigh expansion of $\tilde{G}_j^{qper}$, even at Wood anomalies ($\beta_n = 0$), for any $j \ge 1$. The shifting procedure has thus resulted in rapidly-convergent spatial representations of various orders (equations (2.3.4) and (2.3.5)) as well as spectral representations which do not contain infinities (equation (2.3.8)).

An issue does arise from the shifting method which requires attention: the shifting procedure cancels certain Rayleigh modes for $Y > 0$ and thereby affects the ability of the Green function to represent general fields. In detail, the coefficient $(1 - e^{\mathrm{i}\beta_n h})^j \beta_n^{-1}$ in the series (2.3.8) vanishes if either $\beta_n = 0$ (Wood anomaly) and $j \geq 1$, or if $\beta_n h$ equals an integer multiple of 2π. As in [15], we address this difficulty by simply adding to $\tilde{G}_j^{qper}$ the missing modes. In fact, in a numerical implementation it is beneficial to incorporate corrections containing not only resonant modes, but also *nearly* resonant modes. Thus, using a sufficiently small number η and defining the η-dependent completion function

$$M^\eta(X,Y) = \sum_{n \in U^\eta} e^{\mathrm{i}\alpha_n X + \mathrm{i}\beta_n Y}, \qquad U^\eta = \left\{ n \in \mathbb{Z} : |(1 - e^{\mathrm{i}\beta_n h})^j \beta_n^{-1}| < \eta \right\}, \tag{2.3.9}$$

(where for $\beta_n = 0$ the quotient $|(1-e^{\mathrm{i}\beta_n h})^j \beta_n^{-1}|$ is interpreted as the corresponding limit as $\beta_n \to 0$), a *complete* version of the shifted Green function is given by

$$G_j^{qper}(X,Y) = \tilde{G}_j^{qper}(X,Y) + M^\eta(X,Y) \tag{2.3.10}$$

for (X,Y) outside the set P_j^{qper}.

Remark 2.3.1. *The following section presents an algorithm which, relying on both equations* (2.3.5) *and* (2.3.7)*, rapidly evaluates the Green function $\tilde{G}_j^{qper}$. Section 2.4 presents integral equation formulations based on separate use of the functions $\tilde{G}_j^{qper}$ and M^η, that avoids a minor difficulty (addressed in [15, Remark 4.8]) related to the direct use of the Green function G_j^{qper} defined in* (2.3.10)*.*

2.3.2 Hybrid spatial-spectral evaluation of $\tilde{G}_j^{qper}$

Equation (2.3.8) provides a very useful expression for evaluation of $\tilde{G}_j^{qper}$ for $Y > 0$ at all frequencies, including Wood anomalies—since, for such values of Y, this series converges exponentially fast. Interestingly, further, the related expression (2.3.7) can also be used, again, with exponentially fast convergence, including Wood anomalies, for all values of Y sufficiently far from the set $\{Y = -mh : 0 \leq m \leq j\}$. The latter expression thus provides a greatly advantageous alternative to direct summation of the series (2.3.5) for a majority (but not not the totality) of points (X,Y) relevant in a given quasi-periodic scattering problem.

The exponential convergence of (2.3.7) is clear by inspection. To see that (2.3.7) is well defined at and around Wood anomalies it suffices to substitute the sum in m in equation (2.3.7) by the expression

$$\sum_{m=0}^{j} (-1)^m C_m^j \frac{e^{\mathrm{i}\beta_n |Y+mh|}}{\beta_n} = e^{\mathrm{i}\beta_n Y} \frac{(1 - e^{\mathrm{i}\beta_n h})^j}{\beta_n} - \sum_{\substack{0 \leq m \leq j \\ m < -Y/h}} (-1)^m C_m^j \frac{e^{\mathrm{i}\beta_n (Y+mh)} - e^{-\mathrm{i}\beta_n (Y+mh)}}{\beta_n}. \tag{2.3.11}$$

where, once again, the values of the quotients containing β_n denominators at $\beta_n = 0$ are interpreted as the corresponding $\beta_n \to 0$ limits.

A strategy guiding the selection of the values Y for which the spectral series (2.3.7) is used instead of the spatial series (2.3.5) can be devised on the basis of the relation

$$\beta_n = \mathrm{k}\sqrt{1-(\sin(\theta)+\frac{\lambda}{d}n)^2} \;\approx\; \mathrm{ik}\frac{\lambda}{d}n+\mathcal{O}(1) \;=\; \frac{2n\pi}{d}\mathrm{i}+\mathcal{O}(1). \tag{2.3.12}$$

Indeed, the estimate

$$\left|e^{\mathrm{i}\beta_n|Y+mh|}\right| < Ce^{-2n\pi\frac{\delta}{d}}, \quad (|Y+mh|>\delta>0) \tag{2.3.13}$$

shows that, for $|Y+mh|>\delta>0$, the spectral representation (2.3.7) converges like a geometric series of ratio $e^{-2\pi\frac{\delta}{d}}<1$—with fast convergence for values of $\frac{\delta}{d}$ sufficiently far from zero.

2.4 Hybrid, high-order Nyström solver throughout the spectrum

2.4.1 Integral equation formulation

The Green functions G_j^{qper} presented in Section 2.3 (equation (2.3.10)) can be used to devise an integral equation formulation for problem (2.2.1) which remains valid at Wood Anomalies [15]. As indicated in Remark 2.3.1, however, we proceed in a slightly different manner. Letting $\nu(x')$ denote the normal to the curve Γ at the point $(x', f(x'))$ and ds' denote the element of length on Γ at $(x', f(x'))$, we express the scattered field u^{scat} in (2.2.1), for all $(x,y)\in\Omega_f^+$, as a multipolar double layer potential plus a potential with kernel M^η:

$$u^{scat}(x,y) = \int_0^d \left(\nu(x')\cdot\nabla_{(x',y')}\tilde{G}_j^{qper}(x-x',y-y')\big|_{y'=f(x')} + M^\eta(x-x',y-f(x'))\right)\mu(x')ds'. \tag{2.4.1}$$

Defining the normal-derivative operator $\partial_{\nu'}$, whose action on a given function $K:\mathbb{R}\times\mathbb{R}\to\mathbb{C}$ is given by

$$\partial_{\nu'}K(x,x') = \left[\nu(x')\cdot\nabla_{(x',y')}K(x-x',y-y')\right]_{y=f(x),y'=f(x')}, \tag{2.4.2}$$

and, letting D denote the integral operator

$$D[\mu](x) = \int_0^d \left(\partial_{\nu'}\tilde{G}_j^{qper}(x,x') + M^\eta(x-x',f(x)-f(x'))\right)\mu(x')ds', \quad x\in[0,d], \tag{2.4.3}$$

it follows that μ satisfies the integral equation

$$\frac{1}{2}\mu(x) + D[\mu](x) = -u^{inc}(x) \quad \text{for} \quad x\in[0,d]. \tag{2.4.4}$$

We may also write

$$D[\mu] = \tilde{D}[\mu] + D_M[\mu] \tag{2.4.5}$$

where

$$\tilde{D}[\mu](x) = \int_0^d \partial_{\nu'}\tilde{G}_j^{qper}(x,x')\mu(x')ds' \quad \text{and} \tag{2.4.6}$$

$$D_M[\mu](x) = \int_0^d M^\eta(x-x',f(x)-f(x'))\mu(x')ds'. \tag{2.4.7}$$

It is easy to check [15], finally, that the operator $\tilde{D}$ can be expressed as the infinite integral

$$\tilde{D}[\mu](x) = \int_{-\infty}^{+\infty} \partial_{\nu'} G_j(x, x')\mu(x')ds_\Gamma(x'), \tag{2.4.8}$$

where μ is extended to all of $\mathbb{R}$ by α-quasi-periodicity:

$$\mu(x + d) = \mu(x)e^{\mathrm{i}\alpha d}. \tag{2.4.9}$$

The proposed fast iterative Nyström solver for equation (2.4.4) is based on use of an equispaced discretization of the periodicity interval $[0, d]$, an associated quadrature rule, and an FFT-based acceleration method. The underlying high-order quadrature rule, which is closely related to the one used in [15, Sect. 5], but which incorporates a highly-efficient hybrid spatial-spectral approach for the evaluation of the Green function, is detailed in Section 2.4.2. On the basis of this quadrature rule alone, an unaccelerated Nyström solver for equation (2.4.4) is presented in Section 2.4.3; a discussion concerning the convergence of this algorithm is put forth in Appendix 2.8. The proposed acceleration technique and resulting overall accelerated solver are presented in Section 2.5.

2.4.2 High-order quadrature for the incomplete operator $\tilde{D}$

In the proposed Nyström approach, the smooth windowing function

$$S_{\gamma,a}(x) = \begin{cases} 1 & \text{if } |x| \le \gamma, \\ \exp\left(\frac{2e^{-1/u}}{u-1}\right) & \text{if } \gamma < |x| < a, \quad u = \frac{|x|-\gamma}{a-\gamma}, \\ 0 & \text{if } |x| \ge a, \end{cases} \tag{2.4.10}$$

(see Figure 2.4.1) is used to decompose the operator $\tilde{D}$ in equation (2.4.8) as a sum $\tilde{D} = \tilde{D}_{\text{reg}} + \tilde{D}_{\text{sing}}$ of *regular* and *singular* contributions $\tilde{D}_{\text{reg}}$ and $\tilde{D}_{\text{sing}}$, given by

$$\tilde{D}_{\text{reg}}[\mu](x) = \int_{-\infty}^{+\infty} \partial_{\nu'} G_j(x, x')(1 - S^f_{\gamma,a}(x, x'))\mu(x')ds' \tag{2.4.11}$$

and

$$\tilde{D}_{\text{sing}}[\mu](x) = \int_{x-a}^{x+a} \partial_{\nu'} G_j(x, x')S^f_{\gamma,a}(x, x')\mu(x')ds'. \tag{2.4.12}$$

where we have defined

$$S^f_{\gamma,a}(x, x') = S_{\gamma,a}\left(\sqrt{(x - x')^2 + (f(x) - f(x'))^2}\right). \tag{2.4.13}$$

Remark 2.4.1. *The parameter a is selected so as to appropriately isolate the logarithmic singularity. For definiteness, throughout this chapter it is assumed the relation $a < d$ is satisfied.*

To derive quadrature rules for the operators $\tilde{D}_{\text{reg}}$ and $\tilde{D}_{\text{sing}}$ we consider an equispaced discretization mesh $\{x_\ell\}_{\ell=-\infty}^{\infty}$, of mesh-size $\Delta x = (x_{\ell+1} - x_\ell)$, for the complete real line, which is additionally assumed to satisfy $x_0 = 0$ and $x_N = d$ for a certain integer $N > 0$. The corresponding numerical approximations of the values $\mu(x_\ell)$ $(1 \le \ell \le N)$ will be denoted by μ_ℓ; in view of (2.4.9) the quantities μ_ℓ are extended to all $\ell \in \mathbb{Z}$ by quasi-periodicity:

$$\mu_{(\ell+pN)} = \mu_\ell \; e^{\mathrm{i}\alpha pd} \qquad \ell = 1, \ldots, N \quad p \in \mathbb{Z}. \tag{2.4.14}$$

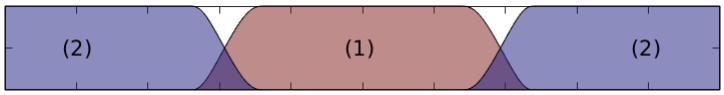

Figure 2.4.1: Partition of Unity functions $S_{\gamma,a}(x)$ and $1 - S_{\gamma,a}(x)$, labeled (1) and (2), respectively.

Discretization of the operator $\tilde{D}_{\text{sing}}$

To discretize the operator $\tilde{D}_{\text{sing}}$ we employ the Martensen-Kussmaul (MK) splitting [29] of the Hankel function H_1^1 into logarithmic and smooth contributions. Following [15, Secs. 5.1-5.2] we thus obtain the decomposition

$$\partial_{\nu'} G_j(x,x') = K_s(x,x') \ln\left[4\sin^2\left(\frac{\pi}{a}(x-x')\right)\right] + K_r(x,x') \tag{2.4.15}$$

where the smooth kernels K_s and K_r are given by

$$K_s(x,x') = \frac{\mathrm{k}}{4\pi} \frac{f(x')(x-x') - (f(x') - f(x))}{\sqrt{(x-x')^2 + (f(x) - f(x'))^2}} J_1(\mathrm{k}\sqrt{(x-x')^2 + (f(x) - f(x'))^2}) \tag{2.4.16}$$

and

$$K_r(x,x') = \partial_{\nu'} G_j(x,x') - K_s(x,x') \ln\left[4\sin^2\left(\frac{\pi}{a}(x-x')\right)\right]. \tag{2.4.17}$$

Replacing (2.4.15) into (2.4.12) we obtain $\tilde{D}_{\text{sing}} = \tilde{D}_{\text{sing}}^{\log} + \tilde{D}_{\text{sing}}^{\text{trap}}$ where

$$\tilde{D}_{\text{sing}}^{\log} = \int_{x-a}^{x+a} \ln\left[4\sin^2\left(\frac{\pi}{a}(x-x')\right)\right] K_s(x,x') S_{\gamma,a}^f(x,x') \mu(x') ds' \quad \text{and} \tag{2.4.18}$$

$$\tilde{D}_{\text{sing}}^{\text{trap}} = \int_{x-a}^{x+a} K_r(x,x') S_{\gamma,a}^f(x,x') \mu(x') ds'. \tag{2.4.19}$$

The operator $\tilde{D}_{\text{sing}}^{\log}$ contains the logarithmic singularity; the operator $\tilde{D}_{\text{sing}}^{\text{trap}}$ on the other hand, may be approximated accurately by means of the trapezoidal rule.

Given that $S_{\gamma,a}^f(x,x')$ vanishes smoothly at $x' = x \pm a$ together with all of its derivatives, we can obtain high-order quadratures for each of these integrals on the basis of the equispaced discretization $\{x_\ell\}$ ($\ell \in \mathbb{Z}$) and the Fourier expansions of the smooth factor $K_s(x,x') S_{\gamma,a}^f(x,x') \mu(x')$. Indeed, utilizing the aforementioned discrete approximations μ_ℓ (where ℓ may lie outside the range $1 \le \ell \le N$), relying on certain explicitly-computable Fourier-based weights $R_{i\ell}$ (which can be computed for general a by following the procedure used in [15, Sec. 5.2] for the particular case in which a equals a half period $d/2$), and appropriately accounting for certain near-singular terms in the kernel K_r by Fourier interpolation of $\mu(x') S_{\gamma,a}^f(x,x')$ (as detailed in [15, Sec. 5.3]), a numerical-quadrature approximation

$$\tilde{D}_{\text{sing}}^{\Delta x}[\mu_1, \ldots, \mu_N](x_i) = \sum_{\ell \in L_i^a} R_{i\ell} K_s(x_i, x_\ell) S_{\gamma,a}^f(x_i, x_\ell) \mu_\ell + \sum_{\ell \in L_i^a} W_{i\ell} K_r(x_i, x_\ell) S_{\gamma,a}^f(x_i, x_\ell) \mu_\ell \tag{2.4.20}$$

of $\tilde{D}_{\text{sing}}[\mu](x_i)$ is obtained. Here $L_i^a : \{\ell : |x_\ell - x_i| \le a\}$, and, for values of $\ell > N$ and $\ell < 1$, μ_ℓ is given by (2.4.14).

Discretization of the operator $\tilde{D}_{\rm reg}$

The windowing function $S_{\gamma,a}$ (with "relatively small" values of a) was used in the previous section to discriminate between singular and regular contributions $\tilde{D}_{\rm sing}$ and $\tilde{D}_{\rm reg}$ to the operator $\tilde{D}$. A new windowing function $S_{cA,A}(x-x')$ (intended for use with "large" values of A) is now introduced to smoothly truncate the infinite integral that defines the operator $\tilde{D}_{\rm reg}$: the truncated operator is defined by

$$\tilde{D}^A_{\rm reg}[\mu](x) = \int_{x-A}^{x+A} \partial_{\nu'} G_j(x,x')(1 - S^f_{\gamma,a}(x,x'))\mu(x') S_{cA,A}(x-x')ds'. \tag{2.4.21}$$

Defining the windowed Green function by

$$\tilde{G}^{q,A}_j(X,Y) = \sum_{p=-\infty}^{\infty} G_j(X+dp,Y) S_{cA,A}(X+dp), \tag{2.4.22}$$

the truncated operator $\tilde{D}^A_{\rm reg}$ can also be expressed in the form

$$\tilde{D}^A_{\rm reg}[\mu](x) = \int_{x-d/2}^{x+d/2} \partial_{\nu'} \tilde{G}^{q,A}_j(x,x')(1 - S^f_{\gamma,a}(x,x'))\mu(x')ds'. \tag{2.4.23}$$

On account of the smoothness of the integrand in (2.4.21), and the fact that it vanishes identically outside $[x-A, x+A]$, the integral (2.4.21) is approximated with superalgebraic order of integration accuracy by the discrete trapezoidal rule expression

$$\tilde{D}^{A,\Delta x}_{\rm reg}[\mu_1,\ldots,\mu_N](x_i) = \sum_{\ell=-\infty}^{\infty} \partial_{\nu'} G_j(x_i,x_\ell) S_{cA,A}(x_i-x_\ell)(1 - S^f_{\gamma,a}(x_i,x_\ell))\mu_\ell (\Delta s)_\ell \tag{2.4.24}$$

where $(\Delta s)_\ell$ denotes the discrete surface element $\Delta x\sqrt{1+f(x_\ell)^2}$, and with μ_ℓ replaced by $\mu(x_\ell)$ ($\ell = 1,\ldots,N$); see also (2.4.9) and (2.4.14).

Remark 2.4.2. *The claimed superalgebraic integration accuracy of the right-hand expression in* (2.4.24) *for a fixed value of A follows from the well known trapezoidal-rule integration-accuracy result for smooth periodic function integrated over their period [46])—since the restriction of the integrand to $[x-A, x+A]$ can be extended to all of $\mathbb{R}$ as a smooth and periodic function $F^{A,x} = F^{A,x}(x')$ of period $2A$.*

An analysis of the smooth truncation procedure, namely, of the convergence of $\tilde{D}^A_{\rm reg}$ to $\tilde{D}_{\rm reg}$ as $A \to \infty$, is easily established on the basis of the convergence analysis [15, 21, 22] for the windowed-Green-function (2.4.22) to the regular shifted series (2.3.5)

$$\tilde{G}^{qper}_j(x,y) = \lim_{A\to\infty} \tilde{G}^{q,A}_j(x,y). \tag{2.4.25}$$

The overall error resulting from the combined use of smooth truncation and trapezoidal discretization is discussed in Section 2.8. In particular, Lemma 2.8.1 in that appendix provides an error estimate that shows that the superalgebraic order of trapezoidal integration accuracy is also uniform with respect to A.

Clearly, the numerical method embodied in equations (2.4.20) and (2.4.24) provides a high-order strategy for the evaluation of the operator $\tilde{D}$ in equation (2.4.8). As shown in the following section, a hybrid spatial/spectral Green-function evaluation strategy can be used to significantly decrease the costs associated with evaluation of the discrete operator in equation (2.4.24). While this strategy suffices in many cases, when used in conjunction with the FFT acceleration method introduced in Section 2.5 a solver results which, as mentioned in the introduction, enables treatment of challenging rough-surface scattering problems.

Spatial/Spectral hybridization

To obtain a hybrid strategy we express (2.4.24) in terms of the function $\tilde{G}_j^{qper}$ which we then evaluate by means of either (2.3.7) or (2.4.25), whichever is preferable for each pair (x_i, x_ℓ). Taking limit as $A \to \infty$ in (2.3.7) we obtain the limiting discrete operator

$$\tilde{D}^{\Delta x}_{\rm reg}[\mu_1, \ldots, \mu_N](x_i) = \sum_{\ell=-\infty}^{\infty} \mu_\ell (1 - S^f_{\gamma,a}(x_i, x_\ell)) \partial_{\nu'} G_j(x_i, x_\ell)(\Delta s)_\ell. \tag{2.4.26}$$

Writing, for every $\ell \in \mathbb{Z}$, $x_\ell = x_k - dp$ for a unique integers k and p ($1 \le k \le N$), exploiting the periodicity of the function f and the α-quasi-periodicity of μ, using (2.4.22) and (2.4.25), and taking into account Remark 2.4.1, we obtain the alternative expression

$$\tilde{D}^{\Delta x}_{\rm reg}[\mu_1, \ldots, \mu_N](x_i) = \sum_{m=1}^{N} \partial_{\nu'} \tilde{G}_j^{qper,\star}(x_i, x_k) \mu_k (\Delta s)_k, \tag{2.4.27}$$

where we have set

$$\tilde{G}_j^{qper,\star}(X, Y) = \tilde{G}_j^{qper}(X, Y) - \sum_{p=-1}^{1} G_j(X + dp, Y) e^{-{\rm i}\alpha dp} S_{\gamma,a}(X + dp). \tag{2.4.28}$$

Clearly, $\tilde{G}_j^{qper,\star}$ is a smooth function that results from subtraction from $\tilde{G}_j^{qper}(X, Y)$ of (windowed versions of) the nearest interactions (modulo the period).

The expression (2.4.27) relies, via (2.4.28), on the evaluation of the exact quasi-periodic Green function $\tilde{G}_j^{qper}(X, Y)$. For a given point (X, Y) this function can be evaluated by either a spectral or a spatial approach: use of the spectral series as described in Section 2.3.2 is preferable for values of Y sufficiently far from the set $\{Y = -mh : \ 0 \le m \le j\}$, while, in view of the fast convergence [15, 21, 22] of (2.4.25), for other values of Y the spatial expansion (2.4.22) with a sufficiently large value of A can be more advantageous. (Note that if the grating is deep enough, then $f(x)$ could be far from $f(x')$ even if x is relatively close to x'. The exponentially convergent spectral approach could provide the most efficient alternative in such cases.)

2.4.3 Overall discretization and (unaccelerated) solution of equation (2.4.4)

Taking into account equation (2.4.5) in conjunction with the Green function evaluation and discretization strategies presented in Section (2.4.2) for the operator $\tilde{D}$, a full discretization for the

complete operator D in (2.4.3) can now be obtained easily: an efficient discretization of the remaining operator D_M in (2.4.7), whose kernel is given by equation (2.3.9), can be produced via a direct application of the trapezoidal rule. Separating the variables X and Y in the exponentials $e^{\mathrm{i}\alpha_n X+\mathrm{i}\beta_n Y}$, further, the resulting discrete operator may be expressed in the form

$$D_M^{\Delta x}[\mu_1,\ldots,\mu_N](x_i) = \sum_{n\in U^\eta} e^{\mathrm{i}\alpha_n x_i}\left(\sum_{\ell=1}^{N} e^{\mathrm{i}\beta_n f(x_\ell)}\mu_\ell(\Delta s)_\ell\right). \tag{2.4.29}$$

Letting

$$D^{\Delta x} = \tilde{D}_{\text{sing}}^{\Delta x} + \tilde{D}_{\text{reg}}^{\Delta x} + D_M^{\Delta x} \tag{2.4.30}$$

we thus obtain the desired discrete version

$$\left(\frac{1}{2}I + D^{\Delta x}\right)[\mu_1,\ldots,\mu_N](x_i) = -u^{inc}(x_i) \tag{2.4.31}$$

of equation (2.4.4).

As mentioned in Section 2.1, the proposed method relies on use of an iterative linear algebra solver such as GMRES [69]. The necessary evaluation of the action of the discrete operator $D^{\Delta x}$ is accomplished, in the direct (unaccelerated) implementation considered in this section, via straightforward applications of the corresponding expressions (2.4.20), (2.4.27) and (2.4.29) for the operators $\tilde{D}_{\text{sing}}^{\Delta x}$, $\tilde{D}_{\text{reg}}^{\Delta x}$ and $D_M^{\Delta x}$, respectively. This completes the proposed unaccelerated iterative solver for equation (2.4.4).

The computational cost required by the various components of this solver can be estimated as follows.

1. The application of the *local* operator $\tilde{D}_{\text{sing}}^{\Delta x}$ requires $\mathcal{O}(N)$ arithmetic operations, the vast majority of which are those associated with evaluation of the multipolar Green function G_j.

2. $D_M^{\Delta x}$, in turn, requires $\mathcal{O}(N)$ operations, including the computation of a number $\mathcal{O}(N)$ of values of exponential functions.

3. The operator $\tilde{D}_{\text{reg}}^{\Delta x}$, finally, requires $\mathcal{O}(N^2)$ arithmetic operations, including the significant cost associated with the evaluation of $\mathcal{O}(N^2)$ values of the shifted-quasi-periodic Green function $\tilde{G}_j^{qper}$.

Clearly, the cost mentioned in point 3 above represents the most significant component of the cost associated of the evaluation of $D^{\Delta x}$. Thus, although highly accurate, the direct $\mathcal{O}(N^2)$-cost strategy outlined above for the evaluation of $D^{\Delta x}$ can pose a significant computational burden for problems which, as a result of high-frequency and/or complex geometries, require use of large numbers N of unknowns. A strategy is presented in the next section which, on the basis of equivalent sources and Fast Fourier transforms leads to significant reductions in the cost of the evaluation of this operator, and, therefore, in the overall cost of the solution method.

2.5 Shifted Equivalent-Source Acceleration

The most significant portion of the computational cost associated with the strategy described in the previous section concerns the evaluation of the discrete operator $\tilde{D}_{\text{reg}}^{\Delta x}$ in equation (2.4.26). The present section introduces an acceleration method for the evaluation of that operator which, incorporating an FFT-based algorithm that is applicable throughout the spectrum, reduces very significantly the number of necessary evaluations of the periodic Green function $\tilde{G}_j^{qper}$, with corresponding reductions in the cost of the overall approach. A degree of familiarity with the acceleration methodology introduced in [18] could be helpful in a first reading of this section.

Central to the contribution [18] is the introduction of "monopole and dipole" representations and an associated notion of "adjacency" that, in modified forms, are used in the present algorithm as well. In order to extend the applicability of the method [18] to the context of this thesis, the present Section 2.5 introduces certain "shifted equivalent source" representations and a corresponding validity-ensuring notion of "adjacency". The geometrical structure that underlies the approach as well an outline of the reminder of Section 2.5 are presented in Section 2.5.1.

2.5.1 Geometric setup

In order to incorporate equivalent sources, the algorithm utilizes a "reference periodicity domain" $\Omega_{per} = [0, d) \times [h_{\min}, h_{\max})$, where $h_{\min}$ and $h_{\max}$ are selected so as to satisfy $[\min(f), \max(f)] \subset [h_{\min}, h_{\max}]$. The domain Ω_{per} is subsequently partitioned in a number $n_{\text{cell}} = n_x n_y$ of mutually disjoint square cells c^q—whose side L, we assume, satisfies

$$d = n_x L \qquad \text{and} \qquad (h_{\max} - h_{\min}) = n_y L \tag{2.5.1}$$

for certain positive integers n_x and n_y. We additionally denote by $\Omega_\infty = (-\infty, +\infty) \times [h_{\min}, h_{\max}]$; clearly Ω_∞ domain that is similarly partitioned into (an infinite number of) cells c^q ($q \in \mathbb{Z}$):

$$\Omega_{\text{per}} = \bigcup_{q=1}^{n_{\text{cell}}} c^q \qquad \text{and} \qquad \Omega_\infty = \bigcup_{q=-\infty}^{\infty} c^q = \bigcup_{n=-\infty}^{\infty} \Big(\Omega_{\text{per}} + nd\Big). \tag{2.5.2}$$

Remark 2.5.1. *It is additionally assumed that the side L of the accelerator cells c^q is selected in such a way that these cells are not resonant for the given wavenumber* k*—that is to say, that $-\mathrm{k}^2$ is not a Dirichlet eigenvalue for the Laplace operator in the cells c^q. This is a requirement in the plane-wave Dirichlet-problem solver described in Section 2.5.6. Clearly, values of the parameters L, $h_{\max}$, $h_{\min}$, n_x and n_y meeting this constraint as well as* (2.5.1) *can be found easily. Finally, the parameter L is chosen so as to minimize the overall computing cost, while meeting a prescribed accuracy tolerance. In all cases considered in this chapter values of L in the range between one and four wavelengths were used.*

Remark 2.5.2. *In order to avoid cell intersections, throughout this chapter the cells c^q are assumed to include the top and right sides, but not to include the bottom and left sides. In other words, it is assumed that each cell c^q can be expressed in the form $c^q = (a_1^q, b_1^q] \times (a_2^q, b_2^q]$ for certain real numbers a_1^q, b_1^q, a_2^q and b_2^q.*

Remark 2.5.3. *With reference to Remark 2.4.1, throughout the reminder of this chapter (and, more specifically, in connection with the accelerated scheme), the parameter a is additionally assumed to satisfy the condition $a < L$. Under this assumption, the singular integration region (that is, the integration interval in* (2.4.12)*) necessarily lies within the union of at most three cells c^q.*

Taking into account (2.3.2), equation (2.4.26) tells us that the quantity $\tilde{D}^{\Delta x}_{\text{reg}}[\mu_1, \ldots, \mu_N](x_i)$ equals the field at the point x_i that arises from free-space "true" sources which are located at points $(x_\ell, f(x_\ell)) - mhe_2$ with $\ell \in \mathbb{Z}$ and $0 \leq m \leq j$, whose x-coordinates differ from x_i in no less than γ (see Figure 2.4.1 and equation (2.4.10)). Figure 2.5.1, which depicts such an array of true sources, displays as black dots (respectively gray dots) the "surface true sources" $(x_\ell, f(x_\ell))$ (resp. the "shifted true sources" $(x_\ell, f(x_\ell)) - mhe_2$ with $1 \leq m \leq j$).

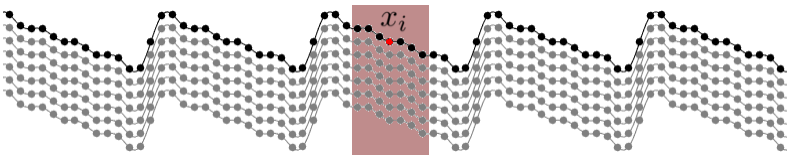

Figure 2.5.1: Surface true sources (black), and shifted true sources (gray). Matching the color code in Figure 2.4.1, the sources giving rise to "local" interactions for the given target point x_i are contained in the region shaded in pink. The accelerated algorithm in Section 2.5.5 below produces $\tilde{D}^{\Delta x}_{\text{reg}}(x_i)$ (equation (2.4.26)) by subtraction of incorrect local contributions in an FFT-based "all-to-all" operator, followed by addition of the correct local contributions.

In order to accelerate the evaluation of the operator $\tilde{D}^{\Delta x}_{\text{reg}}$, at first we disregard the shifted true sources (gray points in Figure 2.5.1) and we restrict attention to the surface true-sources (black dots) that are contained within a given cell c^q. In preparation for FFT acceleration we seek to represent the field generated by the latter sources in two different ways. As indicated in what follows, the equivalent sources are to be located in "Horizontal" and "Vertical" sets Λ^H_q and Λ^V_q of equispaced discretization points,

$$\Lambda^\lambda_q = \{\mathbf{y}^{\lambda,q}_s : s = 1, \ldots, n_{\text{eq}}\} \qquad (\lambda = H, V), \tag{2.5.3}$$

contained on (slight extensions of) the horizontal and vertical sides of c^q, respectively; see Figure 2.5.2. (In the examples considered in this chapter each one of the extended sets Λ^H_q and Λ^V_q contain approximately 20% more equivalent-source points than are contained on each pair of parallel sides of the squares c^q themselves. Such extensions provide slight accuracy enhancements as discussed in [18].) The resulting equivalent-source approximation, which is described in detail in Section 2.5.2, is valid and highly accurate outside the square domain $\mathcal{S}_q$ of side $3L$ and concentric with c^q:

$$\mathcal{S}_q = \bigcup_{-1 \leq m,n \leq 1} \Big(c^q + (n, m)L\Big). \tag{2.5.4}$$

Importantly, for each λ (either $\lambda = H$ or $\lambda = V$) the union of Λ^λ_q for all q (equation (2.5.25) below) is a Cartesian grid, and thus facilitates evaluation of certain necessary discrete convolutions by means of FFTs, as desired.

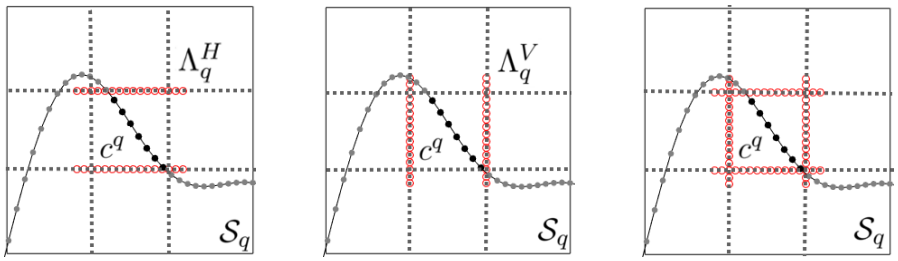

Figure 2.5.2: "Free-Space" Equivalent source geometry. The true sources within c^q (resp. outside c^q) are displayed as solid black (resp. gray) circles. The left, center and right images depict in red unfilled circles the horizontal set Λ_q^H, the vertical set Λ_q^V, and the union $\Lambda_q^H \cup \Lambda_q^V$, respectively.

The proposed acceleration procedure is described below, starting with the computation of the equivalent-source densities (Section 2.5.2) and following with the incorporation of shifted equivalent sources and consideration of an associated validity criterion (Section 2.5.3). This validity criterion induces a decomposition of the operator $\tilde{D}_{\text{reg}}^{\Delta x}$ into two terms (Section 2.5.4), each one of can be produced via certain FFT-based convolutions (Section 2.5.5). A reconstruction of needed surface fields is then produced (Section 2.5.6), and, finally, the overall fast high-order solver for equation (2.4.4) is presented (Section 2.5.7). For convenience, shifted and unshifted "punctured Green functions" $\Phi_j : \mathbb{R}^2 \times \mathbb{R}^2 \to \mathbb{C}$ and $\Phi : \mathbb{R}^2 \times \mathbb{R}^2 \to \mathbb{C}$ are used in what follows which, in terms of the two-dimensional observation and integration variables $\mathbf{x} = (x_1, x_2) \in \mathbb{R}^2$ and $\mathbf{y} = (y_1, y_2) \in \mathbb{R}^2$, are given by

$$\Phi_j(\mathbf{x}, \mathbf{y}) = \begin{cases} G_j(x_1 - y_1, x_2 - y_2) & \text{for } \mathbf{x} \neq \mathbf{y} \\ 0 & \text{for } \mathbf{x} = \mathbf{y} \end{cases} \quad \text{and} \quad \Phi = \Phi_0. \tag{2.5.5}$$

2.5.2 Equivalent-source representation I: surface true sources

As indicated above, this section provides an equivalent-source representation of the contributions to the quantity $\tilde{D}_{\text{reg}}^{\Delta x}[\mu_1, \ldots, \mu_N](x_i)$ in (2.4.26) that arise from surface true sources only (the solid black points in Figure 2.5.1). To do this we define

$$\psi^q(\mathbf{x}) = \sum_{(x_\ell, f(x_\ell)) \in c^q} \left(\mu_\ell \, \frac{\partial}{\partial n_y} \Phi(\mathbf{x}, \mathbf{y})\big|_{\mathbf{y}=(x_\ell, f(x_\ell))} \right) (\Delta s)_\ell, \tag{2.5.6}$$

which denotes the field generated by all of the surface true-sources located within the cell c^q. In the equivalent-source approach, the function ψ^q is evaluated, with prescribed accuracy, by a fast procedure based on use of certain "horizontal" and "vertical" representations, which are valid, within the given accuracy tolerance, for values of $\mathbf{x}$ outside $\mathcal{S}_q$. Each of those representations is given by a sum of monopole and dipole equivalent-sources supported on the corresponding equispaced mesh Λ_q^λ (2.5.3) ($\lambda = H$ or $\lambda = V$).

To obtain the desired representation a least-squares problem is solved for each cell c^q (cf. [18]).

In detail, for $\lambda = H$ and $\lambda = V$ and for each q, an approximate representation of the form

$$\psi^q(\mathbf{x}) \approx \varphi^{q,\lambda}(\mathbf{x}), \quad \text{where} \quad \varphi^{q,\lambda}(\mathbf{x}) = \sum_{s=1}^{n_{eq}} \left(\Phi(\mathbf{x}, \mathbf{y}_s^{q,\lambda}) \xi_s^{q,\lambda} + \frac{\partial}{\partial \nu(y)} \Phi(\mathbf{x}, \mathbf{y}_s^{q,\lambda}) \zeta_s^{q,\lambda} \right) \tag{2.5.7}$$

is sought, where $\xi_s^{q,\lambda}$ and $\zeta_s^{q,\lambda}$ are complex numbers (the "equivalent-source densities"), and where $\nu(y)$ denotes the normal to Λ_q^λ. The densities $\xi_s^{q,\lambda}$ and $\zeta_s^{q,\lambda}$ are obtained as the QR-based solutions [39] of the oversampled least-squares problem

$$\min_{(\xi_s^{q,\lambda}, \zeta_s^{q,\lambda})} \sum_{t=1}^{n_{\text{coll}}} \left| \psi^q(\mathbf{x}_t^q) - \sum_{s=1}^{n_{eq}} \left(\Phi(\mathbf{x}_t^q, \mathbf{y}_s^{q,\lambda}) \xi_s^{q,\lambda} + \frac{\partial}{\partial n_y} \Phi(\mathbf{x}_t^q, \mathbf{y}_s^{q,\lambda}) \zeta_s^{q,\lambda} \right) \right|^2, \tag{2.5.8}$$

where $\{\mathbf{x}_t^q\}_{t=1,\ldots,n_{\text{coll}}}$ is a sufficiently fine discretization of $\partial \mathcal{S}^q$, which in general may be selected arbitrarily, but which we generally take to equal the union of equispaced discretizations of the sides of $\partial \mathcal{S}^q$ (as displayed in Figure 2.5.3). Under these conditions, the equivalent source representation $\varphi^{q,\lambda}$ matches the field values $\psi^q(\mathbf{x})$ for $\mathbf{x}$ on the boundary of $\mathcal{S}^q$ within the prescribed tolerance. Since $\varphi^{q,\lambda}$ and $\psi^q(\mathbf{x})$ are both solutions of the Helmholtz equation with wavenumber k outside $\mathcal{S}^q$, it follows that $\varphi^{q,\lambda}$ agrees closely with $\psi^q(\mathbf{x})$ through the exterior of $\mathcal{S}^q$ as well [18]. The equivalent-source approximation and its accuracy outside of $\mathcal{S}_q$ is demonstrated in Figure 2.5.3 for the case $\lambda = H$ ("horizontal" representation).

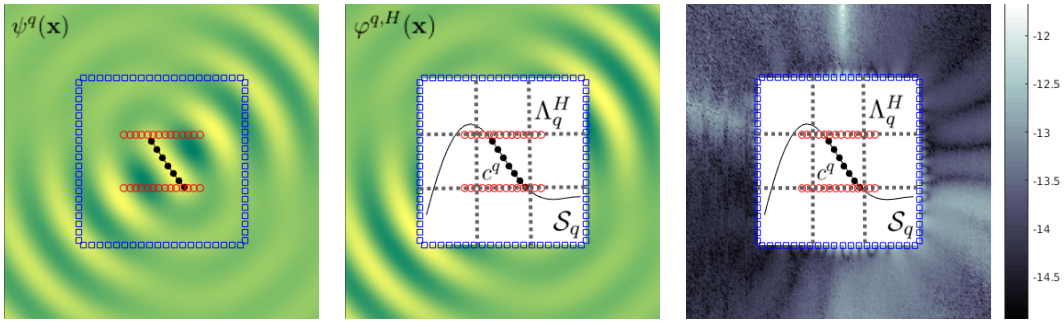

Figure 2.5.3: Left: Field $\psi^q(\mathbf{x})$ generated by the surface true sources (solid black circles), evaluated throughout space. Center: Approximate field $\varphi^{q,H}(\mathbf{x})$ generated by the equivalent sources (unfilled red circles), evaluated outside $\mathcal{S}^q$. Right: approximation error $|\psi^q(\mathbf{x}) - \varphi^{q,H}(\mathbf{x})|$ outside $\mathcal{S}^q$ (in $\log_{10}$ scale). Collocation points $\mathbf{x}_t \in \partial \mathcal{S}^q$ are displayed as blue squares. According to the right image, the error for this test case ($\mathrm{k} = 10$, $L = 0.3$, $n_{\text{eq}} = 10$, $n_{\text{coll}} = 80$) is smaller than 10^{-12} everywhere in the validity region $\{x \in \mathbb{R}^2 : x \notin \mathcal{S}^q\}$..

Remark 2.5.4. *It is easy to see that the equivalent source densities $(\xi_s^{q,\lambda}, \zeta_s^{q,\lambda})$ are α-quasi periodic quantities, in the sense that given two cells, c^q and $c^{q'}$, where $c^{q'}$ is displaced from c^q, in the horizontal direction, by an integer multiple pd of the period d, we have $(\xi_s^{\lambda,q'}, \zeta_s^{\lambda,q'}) = e^{\mathrm{i}\alpha pd}(\xi_s^{\lambda,q}, \zeta_s^{\lambda,q})$. To check this note that, since the corresponding density μ_ℓ is itself α-quasi periodic (equation (2.4.14)), in view of (2.5.6) it follows that so is the quantity $\psi^q(\mathbf{x}_t^r)$ in (2.5.8). In particular, we have $\psi^{q'}(\mathbf{x}_t^{q'}) = e^{\mathrm{i}\alpha pd}\psi^q(\mathbf{x}_t^q)$. Since, additionally, $\Phi(\mathbf{x}_t^{q'}, \mathbf{y}_s^{\lambda,q'}) = \Phi(\mathbf{x}_t^q, \mathbf{y}_s^{\lambda,q})$, we conclude that the least*

square problems (2.5.8) *for q and q' are equivalent, and the desired α-quasiperiodicity of $(\xi_s^{q,\lambda}, \zeta_s^{q,\lambda})$ follows.*

2.5.3 Equivalent-source representation II: shifted true sources

In order to incorporate shifted true sources within the equivalent source representation we define the quantity

$$\psi_j^q(\mathbf{x}) = \sum_{(x_\ell, f(x_\ell)) \in c^q} \left(\mu_\ell \, \frac{\partial}{\partial n_y} \Phi_j(\mathbf{x}, \mathbf{y})\big|_{\mathbf{y}=(x_\ell, f(x_\ell))} \right) (\Delta s)_\ell \tag{2.5.9}$$

which, in view of in view of (2.5.5), contains some of the contributions on the right hand side of (2.4.26). (With reference to (2.4.2), note that a term in the sum (2.5.9) coincides with a corresponding term in (2.4.26) if and only if $1 - S^f_{\gamma,a}(x_i, x_\ell) = 1$. For $\mathbf{y} = (x_\ell, f(x_\ell)) \in c^q$, the latter relation certainly holds provided $\mathbf{x} = (x_i, f(x_i))$ is sufficiently far from c^q. But there are other pairs $(\mathbf{x}, \mathbf{y})$ for which this this relation holds; see Section 2.5.4 below for details.)

In view of (2.3.2), the field ψ_j^q in (2.5.9) includes contributions from all surface sources contained within the cell c^q (solid black dots in Figure 2.5.4), as well as all of the shifted true sources that lie below them (which are displayed as gray dots in Figure 2.5.4). Importantly, as illustrated in Figure 2.5.4, these shifted sources may or may not lie within c^q.

In order to obtain an equivalent-source approximation of the shifted-true-source quantity ψ_j^q in (2.5.9) which is analogous to the approximation (2.5.7) for the surface true sources, we consider the easily-checked relation

$$\psi_j^q(\mathbf{x}) = \sum_{m=0}^{j} (-1)^m C_m^j \psi^q(\mathbf{x} - m\bar{h}), \tag{2.5.10}$$

where $\bar{h} = (0, h)$, and we use the approximation $\psi^q(\mathbf{x} - m\bar{h}) \approx \varphi^{q,\lambda}(\mathbf{x} - m\bar{h})$ which follows by employing (2.5.7) at the point $\mathbf{x} - m\bar{h}$, for each m. Since, in view of the relation $\Phi(\mathbf{x} + \mathbf{z}, \mathbf{y}) = \Phi(\mathbf{x}, \mathbf{y} - \mathbf{z})$, we have

$$\varphi^{q,\lambda}(\mathbf{x} - m\bar{h}) = \sum_{s=1}^{n_{eq}} \left(\Phi(\mathbf{x}, \mathbf{y}_s^{q,\lambda} + m\bar{h}) \xi_s^{q,\lambda} + \frac{\partial}{\partial \nu(y)} \Phi(\mathbf{x}, \mathbf{y}_s^{q,\lambda} + m\bar{h}) \zeta_s^{q,\lambda} \right), \tag{2.5.11}$$

summing (2.5.11) over m yields the desired approximation:

$$\psi_j^q(\mathbf{x}) \approx \varphi_j^{q,\lambda}(\mathbf{x}), \quad \text{where} \quad \varphi_j^{q,\lambda}(\mathbf{x}) = \sum_{s=1}^{n_{eq}} \left(\Phi_j(\mathbf{x}, \mathbf{y}_s^{q,\lambda}) \xi_s^{q,\lambda} + \frac{\partial}{\partial \nu(y)} \Phi_j(\mathbf{x}, \mathbf{y}_s^{q,\lambda}) \zeta_s^{q,\lambda} \right). \tag{2.5.12}$$

The shifted-equivalent-source approximation (2.5.12) is a central element of the proposed acceleration approach. Noting that, for each m, the approximation (2.5.11) is valid for points $\mathbf{x}$ outside a translated domain $\mathcal{S}^q - m\bar{h}$, it follows that, calling

$$\widehat{\mathcal{S}}_j^q = \bigcup_{m=0}^{j} \left(\mathcal{S}^q - m\bar{h} \right), \tag{2.5.13}$$

the overall approximation (2.5.12) is valid for all $\mathbf{x} \notin \widehat{\mathcal{S}}_j^r$. Thus, letting

$$\mathcal{S}_j^q = \bigcup_{\{r\,:\,c^r \cap \widehat{\mathcal{S}}_j^q \neq \emptyset\}} c^r, \tag{2.5.14}$$

(which equals the smallest union of cells c^r that contains $\widehat{\mathcal{S}}_j^q$), it follows, in particular, that (2.5.12) is a valid approximation for all $\mathbf{x} \notin \mathcal{S}_j^q$.

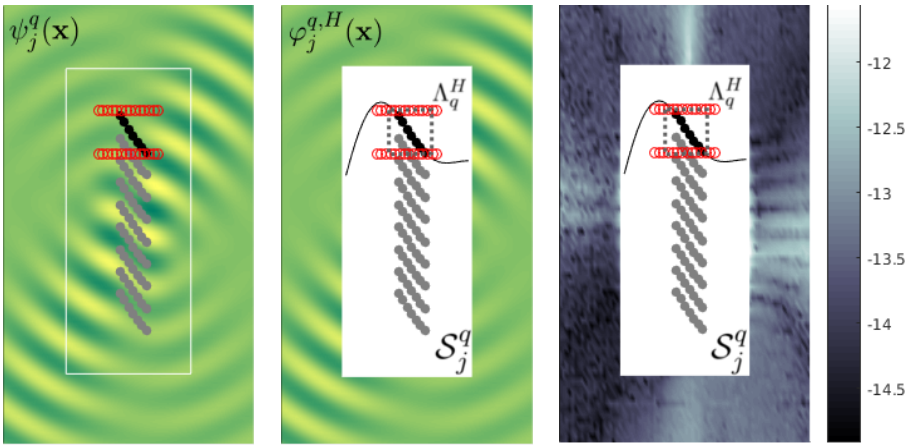

Figure 2.5.4: Left: Field $\psi_j^q(\mathbf{x})$ generated by the combination of the true sources (solid black circles) and their shifted copies (solid gray circles). Center: Approximate field $\varphi_j^{q,H}(\mathbf{x})$ generated by shifted equivalent sources (unfilled red circles). Right: approximation error $|\psi_j^q(\mathbf{x}) - \varphi_j^{q,H}(\mathbf{x})|$ outside $\mathcal{S}_j^q$ (in $\log_{10}$ scale). According to the right image, the error for this test case ($\mathrm{k} = 10$, $L = 0.3$, $n_{\mathrm{eq}} = 10$, $n_{\mathrm{coll}} = 80$) is smaller than 10^{-12} everywhere in the validity region $\left\{x \in \mathbb{R}^2 : x \notin \mathcal{S}_j^q\right\}$.

2.5.4 Decomposition of $\tilde{D}_{\mathrm{reg}}^{\Delta x}$ in "intersecting" and "non-intersecting" contributions

This section introduces a decomposition of the operator $\tilde{D}_{\mathrm{reg}}^{\Delta x}$ as a sum of two terms. With reference to Remark 2.5.2, and denoting by $\overline{A}$ the closure of a set A (the union of the set and its boundary), we define the first term as

$$\psi_j^{ni,q} : \overline{c^q} \to \mathbb{C}, \qquad \psi_j^{ni,q}(\mathbf{x}) = \sum_{\{r \in \mathbb{Z}\,:\,c^q \cap \mathcal{S}_j^r = \emptyset\}} \psi_j^r(\mathbf{x}), \qquad (\mathbf{x} \in \overline{c^q}). \tag{2.5.15}$$

Clearly, for $\mathbf{x} \in \overline{c^q}$, the quantity $\psi_j^{ni,q}(\mathbf{x})$ contains the "non-intersecting" contributions—that is, contributions arising from sources contained in cells $c^r \subset \Omega_\infty$, $-\infty \leq r \leq \infty$ (cf. equation (2.5.2)), such that $\mathcal{S}_j^r$ does not intersect c^q, and for which therefore, according to Section 2.5.3, the approximation (2.5.12) is valid. Since the operator $\tilde{D}_{\mathrm{reg}}^{\Delta x}$ acts on spaces of functions defined on Γ, in what follows we will often evaluate $\psi_j^{ni,q}$ at points $\mathbf{x} \in \overline{c^q}$ of the form $\mathbf{x} = (x_i, f(x_i)) \in \overline{c^q}$. For $\mathbf{x} = (x_i, f(x_i)) \in \overline{c^q}$, then, the second term equals, naturally,

$$\psi_j^{int,q}\Big(x_i, f(x_i)\Big) = \tilde{D}_{\mathrm{reg}}^{\Delta x}[\mu_1, \ldots, \mu_N](x_i) - \psi_j^{ni,q}\Big(x_i, f(x_i)\Big), \qquad (x_i, f(x_i)) \in c^q. \tag{2.5.16}$$

In view of definitions (2.5.9) and (2.5.15), the field $\psi_j^{ni,q}(\mathbf{x})$ can alternatively by expressed in the form

$$\psi_j^{ni,q}(\mathbf{x}) = \sum_{\{\ell\in\mathbb{Z}\,:\,(x_\ell,f(x_\ell))\,\in\, c^r \text{ with } c^q\cap\mathcal{S}_j^r=\emptyset\}} \left(\mu_\ell\,\frac{\partial}{\partial n_y}\Phi_j(\mathbf{x},\mathbf{y})\big|_{\mathbf{y}=(x_\ell,f(x_\ell))}\right)(\Delta s)_\ell. \tag{2.5.17}$$

Note that all non-intersecting contributions to a point $\mathbf{x} = (x_i, f(x_i)) \in c^q$ arise from integration points $(x_\ell, f(x_\ell))$ that are at a distance larger than the side L of c^q. Thus, in view of Remark 2.5.3 ($a < L$), we have $S^f_{\gamma,a}(x_i, x_\ell) = 0$ for all non-intersecting contributions. In view of (2.4.26) and (2.5.17), then, we obtain

$$\psi_j^{int,q}\Big(x_i, f(x_i)\Big) = \sum_{\{\ell\in\mathbb{Z}\,:\,(x_\ell,f(x_\ell))\,\in\, c^r \text{ with } c^q\cap\mathcal{S}_j^r\neq\emptyset\}} \mu_\ell(1 - S^f_{\gamma,a}(x_i, x_\ell))\partial_{\nu'}G_j(x_i, x_\ell)(\Delta s)_\ell. \tag{2.5.18}$$

The following two sections (2.5.5 and 2.5.6) present an efficient evaluation strategy for the quantities $\psi_j^{ni,q}(\mathbf{x})$ over $\Gamma \cap c^q$, for $q = 1, \ldots, n_{\text{cell}}$. This strategy relies on use of the approximation

$$\psi_j^{ni,q}(\mathbf{x}) \approx \varphi_j^{ni,q,\lambda}(\mathbf{x}); \qquad \varphi_j^{ni,q,\lambda}(\mathbf{x}) = \sum_{\{r\in\mathbb{Z}\,:\,c^q\cap\mathcal{S}_j^r=\emptyset\}} \sum_{s=1}^{n_{\text{eq}}} \left(\Phi_j(\mathbf{x},\mathbf{y}_s^{r,\lambda})\xi_s^{r,\lambda} + \frac{\partial}{\partial n_y}\Phi_j(\mathbf{x},\mathbf{y}_s^{r,\lambda})\zeta_s^{r,\lambda}\right), \tag{2.5.19}$$

(for $\mathbf{x} \in c^q$) which can be obtained by substituting equation (2.5.12) into (2.5.15). As shown in Section 2.5.5, the quantities $\varphi_j^{ni,q,\lambda}(\mathbf{x})$ in (2.5.19) ($q = 1, \ldots, n_{\text{cell}}$) are related to a single discrete Cartesian convolution that can be evaluated rapidly by means of the FFT algorithm. Once $\psi^{ni,q}(\mathbf{x})$ has been evaluated (by means of $\varphi_j^{ni,q,\lambda}$), the remaining "local" contributions $\psi_j^{int,q}$ to $\tilde{D}^{\Delta x}_{\text{reg}}$ can be incorporated using (2.5.18) at a small computational cost. The overall fast high-order numerical algorithm for evaluation of the operator on the left-hand side of equation (2.4.4) (which also incorporates the implementations of the operators $\tilde{D}^{\Delta x}_{\text{sing}}$ and $D^{\Delta x}_M$ presented in Section 2.4.3) together with the associated fast iterative solver, are then summarized in Section 2.5.7.

2.5.5 Approximation of $\psi_j^{ni,q}$ via global and local convolutions at FFT speeds

In order to accelerate the evaluation of $\psi_j^{ni,q}$ by means of the FFT algorithm we introduce the quantity

$$\varphi_j^{all,\lambda}(\mathbf{x}) = \sum_{r\in\mathbb{Z}}\sum_{s=1}^{n_{\text{eq}}} \left(\Phi_j(\mathbf{x},\mathbf{y}_s^{r,\lambda})\xi_s^{r,\lambda} + \frac{\partial}{\partial n_y}\Phi_j(\mathbf{x},\mathbf{y}_s^{r,\lambda})\zeta_s^{r,\lambda}\right) \tag{2.5.20}$$

which incorporates the non-intersecting terms already included in (2.5.19) as well as undesired "intersecting" (local) terms. For each q, the sum of all undesired intersecting terms for the domain $\overline{c^q}$ is a function $\varphi_j^{int,q,\lambda} : \overline{c^q} \to \mathbb{C}$ given by

$$\varphi_j^{int,q,\lambda}(\mathbf{x}) = \sum_{\substack{r\in\mathcal{L}(q)\\ 1\le s\le n_{\text{eq}}}} \left(\Phi_j(\mathbf{x},\mathbf{y}_s^{r,\lambda})\xi_s^{r,\lambda} + \frac{\partial}{\partial n_y}\Phi_j(\mathbf{x},\mathbf{y}_s^{r,\lambda})\zeta_s^{r,\lambda}\right), \quad \text{where } \mathcal{L}(q) = \{r \in \mathbb{Z} : c^q \subset \mathcal{S}_j^r\}. \tag{2.5.21}$$

Since, by construction, $c^q \cap \mathcal{S}_j^r \neq \emptyset$ if and only if $c^q \subset \mathcal{S}_j^r$, in view of (2.5.19) we clearly have

$$\varphi_j^{ni,q,\lambda} = \varphi_j^{all,\lambda} - \varphi_j^{int,q,\lambda}. \tag{2.5.22}$$

This relation reduces the evaluation of $\varphi_j^{ni,q,\lambda}$ to evaluation of the q-independent quantity (2.5.20) and the q-dependent quantity (2.5.21).

The expression (2.5.20) for $\varphi_j^{all,\lambda}$ requires the evaluation of an infinite sum. Exploiting the fact that, as indicated in Remark 2.5.4, the equivalent sources $(\xi_s^{r,\lambda}, \zeta_s^{r,\lambda})$ are α-quasi-periodic quantities, a more convenient expression can be obtained. Indeed, defining

$$\widetilde{\Phi}_j^{qper} : \mathbb{R}^2 \times \mathbb{R}^2 \to \mathbb{C}, \qquad \widetilde{\Phi}_j^{qper}(\mathbf{x}, \mathbf{y}) = \begin{cases} \tilde{G}_j^{qper}(x_1 - y_1, x_2 - y_2) & \text{for } \mathbf{x} \neq \mathbf{y} \\ 0 & \text{for } \mathbf{x} = \mathbf{y} \end{cases} \tag{2.5.23}$$

in terms of the variables $\mathbf{x} = (x_1, x_2) \in \mathbb{R}^2$ and $\mathbf{y} = (y_1, y_2) \in \mathbb{R}^2$, we can express $\varphi_j^{all,\lambda}$ as the sum

$$\varphi_j^{all,\lambda}(\mathbf{x}) = \sum_{r=1}^{n_{\text{cell}}} \sum_{s=1}^{n_{\text{eq}}} \left(\widetilde{\Phi}_j^{qper}(\mathbf{x}, \mathbf{y}_s^{r,\lambda}) \xi_s^{r,\lambda} + \frac{\partial}{\partial n_y} \widetilde{\Phi}_j^{qper}(\mathbf{x}, \mathbf{y}_s^{r,\lambda}) \zeta_s^{r,\lambda} \right) \tag{2.5.24}$$

of finitely many terms, each one of which contains $\widetilde{\Phi}_j^{qper}$.

In order to evaluate the quantities $\varphi_j^{all,\lambda}$ and $\varphi_j^{int,q,\lambda}$ by means of the FFT algorithm we use the equivalent-source meshes Λ_q^λ introduced in Section 2.5.1 (and depicted in Figure 2.5.2) and we define, for $\lambda = H, V$, the "global" and "local" Cartesian grids

$$\Pi_\lambda^{per} = \bigcup_{\{r \in \mathbb{Z} \,:\, c^r \subseteq \Omega_{per}\}} \Lambda_r^\lambda \qquad \text{and} \qquad \Pi_\lambda^q = \bigcup_{\{r \in \mathbb{Z} \,:\, c^q \subset \mathcal{S}_j^r\}} \Lambda_r^\lambda. \tag{2.5.25}$$

The following two sections describe algorithms which rapidly evaluate these quantities by means of FFTs. The evaluation of $\psi_j^{ni,q}$ (which is the main goal of Section 2.5.5) then follows directly, as indicated in Section 2.5.5.

Evaluation of $\varphi_j^{all,\lambda}$ in Π_λ via a global convolution

In order to express $\varphi_j^{all,\lambda}$ as a convolution, for $\mathbf{y}' \in \Pi_\lambda^{per}$ and $\lambda = H, V$ we define the sums

$$\xi^{all,\lambda}(\mathbf{y}') = \sum_{\substack{1 \leq r \leq n_{\text{cell}} \\ 1 \leq s \leq n_{\text{eq}} \\ \mathbf{y}_s^{r,\lambda} = \mathbf{y}'}} \xi_s^{r,\lambda} \qquad \text{and} \qquad \zeta^{all,\lambda}(\mathbf{y}') = \sum_{\substack{1 \leq r \leq n_{\text{cell}} \\ 1 \leq s \leq n_{\text{eq}} \\ \mathbf{y}_s^{r,\lambda} = \mathbf{y}'}} \zeta_s^{r,\lambda} \tag{2.5.26}$$

of equivalent source densities $\xi_s^{r,\lambda}$ and $\zeta_s^{r,\lambda}$, respectively ($1 \leq r \leq n_{\text{cell}}$), that are supported at a given point $\mathbf{y}' \in \Pi_\lambda^{per}$. We note that two and even four contributions may arise at a point $\mathbf{y}' \in \Pi_\lambda^{per}$—as $\mathbf{y}'$ may lie on a common side of two neighboring cells, and, in some cases, on the intersection of four different sets Λ_q^λ—on account of overlap of the extended regions described in Section 2.5.1 and depicted in Figure 2.5.2.

Replacing (2.5.26) in (2.5.24), we arrive at the discrete-convolution expression

$$\varphi_j^{all,\lambda}(\mathbf{x}) = \sum_{\mathbf{y}' \in \Pi_\lambda^{per}} \left(\widetilde{\Phi}_j^{qper}(\mathbf{x}, \mathbf{y}') \xi^{all,\lambda}(\mathbf{y}') + \frac{\partial}{\partial n_y} \widetilde{\Phi}_j^{qper}(\mathbf{x}, \mathbf{y}') \zeta^{all,\lambda}(\mathbf{y}') \right), \quad \mathbf{x} \in \Pi_\lambda^{per}, \tag{2.5.27}$$

for the quantity $\varphi_j^{all,\lambda}$ on the mesh Π_λ^{per}. The evaluation of this convolution can be performed by a standard FFT-based procedure in $O(M \log M)$ operations, where $M = O(n_{\text{cell}} n_{eq})$ denotes the number of elements in Π_λ^{per}. Note that, per equation (2.5.23), this global FFT algorithm requires the values of the quasi-periodic Green function $\tilde{G}_j^{qper}(X,Y)$ (see also Remark 2.5.5 below) at points (X,Y) in the "evaluation grid" $\widehat{\Pi}_\lambda^{per} = \{\mathbf{x} - \mathbf{y} : \mathbf{x}, \mathbf{y} \in \Pi_\lambda^{per}\}$. In fact, this is the only point in the accelerated algorithm that requires use of the quasi-periodic Green function.

Remark 2.5.5. *An efficient strategy for the evaluation of $\tilde{G}_j^{qper}(X,Y)$ at a given point was presented in Section 2.3.2, which makes use of both spectral and spatial representations of this function. Additional performance gains are obtained in the present context by exploiting certain symmetries in the evaluation grid $\widehat{\Pi}_\lambda^{per}$. The identity $\tilde{G}_j^{qper}(X+d,Y) = e^{i\alpha d}\tilde{G}_j^{qper}(X,Y)$ is used to restrict the evaluation of the function $\tilde{G}_j^{qper}(X,Y)$ at, say, only positive values of X; for the $j=0$ case, the identity $\tilde{G}_0^{qper}(X,Y) = \tilde{G}_0^{qper}(X,-Y)$ is similarly used to restrict evaluation of $\tilde{G}_0^{qper}(X,Y)$ to positive values of Y. Further, since the spectral series* (2.3.8) *is a sum of exponentials which can expressed as products of exponentials that depend on X and Y separately, the spectral series can be evaluated efficiently by utilizing precomputed values of the required single-variable exponentials—with limited computing and storage cost. For an efficient implementation of the spatial series, finally, asymptotic expansions of the Hankel functions as proposed in [15] are also used. The overall strategy produces the required values of $\tilde{G}_j^{qper}$ over the necessary evaluation grid $\widehat{\Pi}_\lambda^{per}$ in a highly efficient manner.*

Evaluation of $\varphi_j^{int,q,\lambda}$ in Π_λ^q via a local convolution

In order to express $\varphi_j^{int,q,\lambda}$ (equation (2.5.21)) as a convolution, for $\mathbf{y}' \in \Pi_\lambda^q$, we define the sums

$$\xi^{q,\lambda}(\mathbf{y}') = \sum_{\substack{r\in\mathcal{L}(q)\\ 1\le s\le n_{\text{eq}}\\ \mathbf{y}_s^{r,\lambda}=\mathbf{y}'}} \xi_s^{r,\lambda} \qquad \text{and} \qquad \zeta^{q,\lambda}(\mathbf{y}') = \sum_{\substack{r\in\mathcal{L}(q)\\ 1\le s\le n_{\text{eq}}\\ \mathbf{y}_s^{r,\lambda}=\mathbf{y}'}} \zeta_s^{r,\lambda} \tag{2.5.28}$$

of equivalent source densities $\xi_s^{r,\lambda}$ and $\zeta_s^{r,\lambda}$, respectively, that are supported at the point $\mathbf{y}' \in \Pi_\lambda^q$, where r lies in the local set of indexes $\mathcal{L}(q)$ defined in (2.5.21). Note that, the set $\mathcal{L}(q)$ contains integers r that may lie outside the range $1 \le r \le n_{\text{cell}}$. In such cases, in order to avoid use of equivalent source densities that lie outside the reference periodicity domain Ω^{per}, the α-quasiperiodicity of $\xi_s^{r,\lambda}$ and $\zeta_s^{r,\lambda}$ (Remark 2.5.4) is utilized to re-express the sums in (2.5.28) in terms of equivalent sources $\xi_s^{r,\lambda}$ and $\zeta_s^{r,\lambda}$ for which $1 \le r \le n_{\text{cell}}$. Additionally note that, as in Section 2.5.5, two and even four contributions may arise in the sums (2.5.28) for a given point $\mathbf{y}' \in \Pi_\lambda^q$.

Replacing (2.5.28) in (2.5.21) yields the discrete-convolution expression

$$\varphi_j^{int,q,\lambda}(\mathbf{x}) = \sum_{\mathbf{y}'\in\Pi_\lambda^q} \left(\Phi_j(\mathbf{x},\mathbf{y}')\xi^{q,\lambda}(\mathbf{y}') + \frac{\partial}{\partial n_y}\Phi_j(\mathbf{x},\mathbf{y}')\zeta^{q,\lambda}(\mathbf{y}') \right), \quad \mathbf{x} \in \Pi_\lambda^q, \tag{2.5.29}$$

which can be evaluated for all $\mathbf{x} \in \Pi_\lambda^q$ by means of an FFT procedure, in $O(M_q \log M_q)$ operations, where $M_q = O(n_{eq})$ denotes the number of elements in Π_λ^q. This time, the Green function Φ_j has

to be evaluated on the "evaluation grid"

$$\widehat{\Pi}_\lambda^q = \{\mathbf{x}-\mathbf{y} : \mathbf{x},\mathbf{y} \in \Pi_\lambda^q\}. \tag{2.5.30}$$

Notice that the set $\widehat{\Pi}_\lambda^q$ is in fact independent of q.

Approximation of $\psi_j^{ni,q}$ on the boundary of c^q

Having obtained $\varphi_j^{int,q,\lambda}(\mathbf{x})$ and $\varphi_j^{all,\lambda}(\mathbf{x})$, the desired quantities $\varphi_j^{ni,q,\lambda}(\mathbf{x})$, for $\lambda = H, V$ follow from (2.5.22). For each q ($1 \le q \le n_{\text{cell}}$) the resulting discrete values $\varphi_j^{ni,q,H}$ and $\varphi_j^{ni,q,V}$ are finally used to form the mesh functions

$$\varphi_j^{ni,q} : \overline{c^q} \cap (\Pi_H^q \cup \Pi_V^q) \to \mathbb{C}, \qquad \varphi_j^{ni,q}(\mathbf{x}) = \varphi_j^{ni,q,\lambda}(\mathbf{x}) \quad \text{for} \quad \mathbf{x} \in \overline{c^q} \cap \Pi_\lambda^q \quad \text{and} \quad \lambda = H, V. \tag{2.5.31}$$

It is clear, by construction, that $\varphi_j^{ni,q}(\mathbf{x})$ is an approximation of $\psi_j^{ni,q}(\mathbf{x})$ for each element $\mathbf{x}$ in the discretization $\overline{c^q} \cap (\Pi_H^q \cup \Pi_V^q)$ of the boundary of c^q. Using these approximate values, the next section presents a method for the high-order evaluation of $\psi_j^{ni,q}(\mathbf{x})$ at an arbitrary point within c^q, and thus, in particular, on the portion $\Gamma \cap c^q$ of the scattering surface Γ contained within c^q.

2.5.6 Plane Wave representation of $\psi_j^{ni,q}$ within c^q

Since $\psi_j^{ni,q}(\mathbf{x})$ satisfies the Helmholtz equation within the cell c^q, and in view of Remark 2.5.1, this field can be obtained within that cell as the solution of the Dirichlet problem with values $\psi_j^{ni,q}(\mathbf{x})$ on the cell boundary. Using the approximate values $\varphi_j^{ni,q}$ of the field $\psi_j^{ni,q}(\mathbf{x})$ that are produced, on the discrete mesh $\overline{c^q} \cap (\Pi_H^q \cup \Pi_V^q)$, by the fast algorithm described in Section 2.5.5, approximate values of the solution $\psi_j^{ni,q}(\mathbf{x})$ of this Dirichlet problem for $\mathbf{x} \in c^q$ are obtained [18] by means of a discrete plane wave expansion. Thus, using a number n_{plw} of plane waves, the proposed approximation for $\mathbf{x} \in c^q$ is thus given by the expression

$$\psi_j^{ni,q}(\mathbf{x}) \approx \eta_j^{ni,q}(\mathbf{x}) \quad \text{where} \quad \eta_j^{ni,q}(\mathbf{x}) = \sum_{s=1}^{n_{\text{plw}}} w_s . e^{\mathrm{i}\mathrm{k} d_s \cdot \mathbf{x}}, \quad \mathbf{x} \in c^q, \tag{2.5.32}$$

where the weights w_i are obtained as the QR solution [39] of the least squares problem

$$\min_{\{w_s\}} \sum_{\mathbf{x} \in \overline{c^q} \cap (\Pi_H^q \cup \Pi_V^q)} \left| \varphi_j^{ni,q}(\mathbf{x}) - \sum_{s=1}^{n_{\text{plw}}} w_s . e^{\mathrm{i}\mathrm{k} d_s \cdot \mathbf{x}} \right|^2, \quad \text{where} \quad d_s = \left(\sin\left(\frac{2\pi s}{n_{\text{plw}}}\right), \cos\left(\frac{2\pi s}{n_{\text{plw}}}\right) \right). \tag{2.5.33}$$

This is the last necessary element in the proposed algorithm for fast approximate evaluation of the operator $\tilde{D}_{\text{reg}}^{\Delta x}$. Using the various components introduced above in the present Section 2.5, Section 2.5.7 describes the overall proposed fast high-order solver.

2.5.7 Overall fast high-order solver for equation (2.4.4)

The overall solver described in what follows results as a modified version of the unaccelerated solver presented in Section 2.4.3: in the present accelerated solver the evaluation of the operator

$\tilde{D}^{\Delta x}_{\text{reg}}$ is carried out using the procedure described in Sections 2.5.1 through 2.5.6 instead of the straightforward $O(N^2)$ approach used in Section 2.4.3. Algorithms 1 to 3 summarize the overall accelerated solution method.

Algorithm 1 Main program: solution of equation (2.4.31)

Run Initialization (Algorithm 2)

Run GMRES iterations, using the forward-map Algorithm 3, on the linear algebra problem (2.4.31)

Algorithm 2 Initialization

Obtain QR factors for (2.5.8) and (2.5.33)	// Only once (they do not depend on q).
Evaluate G_j^{qper} on $\widehat{\Pi}_\lambda^{per}$	// Remark 2.5.5.
Evaluate G_j on $\widehat{\Pi}_\lambda^{q}$	// Only once ($\widehat{\Pi}_\lambda^{q}$ in (2.5.30) does not depend on q).
Precompute matrices for $\tilde{D}^{\Delta x}_{\text{sing}}$ and $D^{\Delta x}_M$	// Equations (2.4.20) and (2.4.29).

Algorithm 3 Discrete forward map: $[\mu_1, \ldots, \mu_n] \to \left(\frac{1}{2}I + D^{\Delta x}\right)[\mu_1, \ldots, \mu_n]$

$\{(\xi_s^{q,\lambda}, \zeta_s^{q,\lambda})\} \longleftarrow$ `EqSources`	// Solve least squares problem (2.5.8).
$\{(\xi_{\mathbf{y}'}^{all,\lambda}, \zeta_{\mathbf{y}'}^{all,\lambda})\} \longleftarrow$ `GlobalEqSMerge`	// Combine equivalent sources (2.5.26).
$\{\varphi_j^{all,\lambda}\} \longleftarrow$ `GlobalFFT`	// Evaluate (2.5.27) via FFT on the grid Π_λ^{per}.
$\{(\xi_{\mathbf{y}'}^{q,\lambda}, \zeta_{\mathbf{y}'}^{q,\lambda})\} \longleftarrow$ `LocalEqSMerge`	// Combine equivalent sources (2.5.28).
$\{\varphi_j^{int,q,\lambda}\} \longleftarrow$ `LocalFFT`	// Evaluate (2.5.29) via FFT on the grid Π_λ^{q}.
$\{\varphi_j^{ni,q,\lambda}\} \longleftarrow$ `LocalSubtract`	// Subtract $\varphi_j^{int,q,\lambda}$ from $\varphi_j^{all,\lambda}$ (2.5.22).
$\{\varphi_j^{ni,q}\} \longleftarrow$ `Combine-`λ	// Combine $\varphi_j^{ni,q,H}$ and $\varphi_j^{ni,q,V}$ as in (2.5.31).
$\{w_s^q\} \longleftarrow$ `PlaneWaveWeights`	// Solve least square problem (2.5.33).
$\psi_j^{ni,q} \dashleftarrow$ `NonIntersecting`	// Use (2.5.32); $\mathbf{x} = (x_i, f(x_i)) \in c^q$.
$\psi_j^{int,q} \longleftarrow$ `Intersecting`	// Use (2.5.18); $(x_i, f(x_i)) \in c^q$.
$\tilde{D}^{\Delta x}_{\text{reg}} \dashleftarrow$ `EvalRegular`	// Use (2.5.16), $\psi_j^{ni,q}(x_i, f(x_i))$, $\psi_j^{int,q}(x_i, f(x_i))$.
$\tilde{D}^{\Delta x}_{\text{sing}} \longleftarrow$ `EvalSingular`	// Use (2.4.20); $1 \le i \le N$.
$D^{\Delta x}_M \longleftarrow$ `EvalModes`	// Use (2.4.29); $1 \le i \le N$.
$\left(\frac{1}{2}I + D^{\Delta x}\right) \longleftarrow$ `AddOperators`	// Add $\frac{1}{2}I$, $\tilde{D}^{\Delta x}_{\text{sing}}$, $\tilde{D}^{\Delta x}_{\text{reg}}$ and $D^{\Delta x}_M$ (2.4.30)-(2.4.31).

Algorithm 3: Routines `EqSource`, `GlobalFFT`, etc. perform the tasks described in the corresponding comments on the right column, resulting on the values indicated by the left-pointing solid arrows. Dashed arrows indicate that an additional approximation is used in the assignment. Whenever the resulting values (on the left) depend on q and/or λ, the operations are performed for $1 \le q \le n_{\text{cell}}$ and/or for $\lambda = H, V$, respectively.

The accuracy and efficiency of this algorithm is demonstrated in the following section.

Remark 2.5.6. *Once a solution μ of the integral equation* (2.4.4) *has been obtained, a single*

application of a slightly modified version of Algorithm 3 enables the evaluation of the scattered field $u^{scat}(\mathbf{x})$ *in* (2.4.1)*, and thus the total field* $u(\mathbf{x}) = u^{scat}(\mathbf{x}) + u^{inc}(\mathbf{x})$*, at all points* $\mathbf{x} = (x, y)$ *in a given two-dimensional domain—at a very moderate additional computational cost. In brief, the modified evaluation procedure only requires that equations* (2.5.18) *and* (2.5.32)*, together with their dependencies, be implemented so as to produce the necessary scattered field* u^{scat} *at all points where the fields are desired.*

2.6 Numerical results

This section presents results of applications of the proposed algorithm to problems of scattering by perfectly conducting periodic rough surfaces, at both Wood and non-Wood configurations, with sinusoidal and composite rough surfaces (including randomly rough Gaussian surfaces), and through wide ranges of problem parameters—including grazing incidences and high period-to-wavelength and/or height-to-period ratios. The presentation is prefaced by a brief section concerning computational costs. For brevity, only results for the accelerated method are presented. In all cases these results compare favorably, in terms of computing times, accuracy and generality, with those provided by previous approaches. All computational results presented in this section were obtained from single-core runs on a 3.4GHz Intel i7-6700 processor with 4 Gb of memory.

2.6.1 Computing costs

The dependence of the computing cost of the algorithm on the size of the problem is subtle, as it includes costs components from various code elements (acceleration, integration, Green function evaluations, etc.), each one of which depends significantly on a variety of structural parameters—including the shift-parameter h, the various ratios H/d, H/λ, d/λ involving the height H, the period d, and the wavelength λ, and the "roughness" of the surface, as quantified by the decay of the associated spectrum. Roughly speaking, however, the results in the present section suggest two important asymptotic regimes exist: (1) d/λ grows as H/λ is kept fixed; and, (2) Both d/λ and H/λ are allowed to grow simultaneously.

In case (1), which arises in the context of studies of scattering by randomly rough surfaces such as the Gaussian surfaces considered in Section 2.6.4, the cost of the algorithm grows at most linearly with the number of unknowns—regardless of the incidence angle, and including near grazing incidences. This favorable behavior stems from the decay experienced by the shifted Green function G_j used in (2.3.5) as d/λ grows while keeping a constant height H/λ (cf. (2.3.4) and [15, Sec. 5.4]). As a result of this decay, the number n_{per} of terms necessary to obtain a prescribed error tolerance in the summation of (2.3.5) decreases as d grows. In case (2), on the other hand, the computational cost is generally observed to range from $O(N)$ up to $O(N^{\frac{3}{2}})$, and it can even reach $O(N^2)$ for extreme geometries.

The cost of the overall algorithm can be affected significantly by the value selected for the shift-parameter h (or, rather, of the dimensionless parameter h/λ). On one hand, this parameter controls the rate of convergence of the spatial series for the shifted Green function: smaller values

of h/λ result in faster convergence of this series. On the other hand, however, use of very small values of h/λ does give rise to certain ill-conditioning difficulties (which, for geometric reasons, become more and more pronounced as the grating-depths increase [15]). In particular, since, for a fixed h/λ value, the distance between the scattering surface and the first shifted source decreases as the depth of the surface is increased, to avoid ill-conditioned-related accuracy losses it becomes necessary to use larger and larger values of h/λ as the surface height grows. The selection of such larger h/λ values, in turn, requires use of increasingly higher number of periods for the summation of the spatial periodic Green function to maintain accuracy. For the test cases considered in this chapter, values of h/λ in the range $\frac{1}{3} \leq h/\lambda \leq 1$ were generally used. For even steeper gratings, larger upper bounds must be utilized in order to maintain a given accuracy tolerance.

In any case, examination of the numerical results presented in what follows does indicate that, for highly challenging scattering configurations of the types that arise in a wide range of applications, the accelerated solver introduced in this thesis provides significant performance improvements over the previous state of the art: the proposed solver is often hundreds of times faster and beyond, and significantly more accurate, than other available approaches. And, importantly, it is applicable to Wood anomaly configurations, and it is extensible to the three-dimensional case while maintaining a full Wood-anomaly capability [20].

2.6.2 Convergence

In order to assess the convergence rate of the proposed algorithm, we consider the problem of scattering of an incident plane-wave at a fixed incidence angle $\theta = 45^\circ$ by the composite surface [17]

$$f(x) = -\frac{1}{4}\left(\sin(x) + \frac{1}{2}\sin(2x) + \frac{1}{3}\sin(3x) + \frac{1}{4}\sin(4x)\right), \qquad x \in (0, 2\pi)$$

depicted in Figure 2.6.1, whose peak to trough height $H = \max(f) - \min(f)$ equals 0.763, and whose period d equals 2π. For this test we consider two slightly different wavenumbers, namely, the non-Wood wavenumber $\mathrm{k} = 20$, for which we have $\frac{H}{\lambda} = 2.43$ and $\frac{d}{\lambda} = 20$, and the Wood wavenumber $\mathrm{k} = 6(1-\sin(\theta))^{-1} \approx 20.4852...$ for which the $\frac{H}{\lambda}$ and $\frac{d}{\lambda}$ ratios are slightly larger. Table 2.6.1 presents results of convergence studies for these two test configurations, using the unshifted Green function ($j = 0$) for the non-Wood cases, and relying, for the Wood cases, on the shifted Green function with shift-parameter values $j = 8$ and $h = 0.16 \approx \lambda/2$. In both cases the accelerator parameters $L = \lambda$, $n_{\mathrm{eq}} = 10$ and $n_{\mathrm{plw}} = 35$ and $n_{\mathrm{coll}} = 200$ were used. This table displays the calculated values ε of the energy-balance error (1.2.11) as well as the error $\tilde{\varepsilon}$ defined as the maximum for $n \in U$ of the errors in each one of the scattering efficiencies e_n (Section 2.2). (The quantities $\tilde{\varepsilon}$ in Table 2.6.1 were evaluated by comparison with reference values obtained using large values of N and n_{per}.)

Table 2.6.1 demonstrates the high-order convergence and efficiency enjoyed by the proposed algorithm, even for Wood configurations for which the classical Green function is not even defined. Concerning accuracy, we see that a mere doubling of the number of discretization points and the number of terms used for summation of the shifted Green function suffices to produce significant improvements in the solution error. Additionally, an increase in computing costs by a factor of five

Table 2.6.1: Convergence in a simple composite surface for Wood and non-Wood cases.

		k = 20 (non-Wood)			k = 20.4852...[a] (Wood Anomaly)		
N	n_{per}	Total time	ε	$\tilde{\varepsilon}$	Total time	ε	$\tilde{\varepsilon}$
100	50	0.09 sec	5.1e-03	1.3e-03	0.67 sec	5.9e-02	2.2e-02
150	75	0.09 sec	1.0e-05	4.2e-05	0.84 sec	9.0e-04	2.8e-04
200	100	0.10 sec	4.9e-06	4.2e-05	1.02 sec	3.4e-05	7.0e-05
300	150	0.13 sec	1.2e-06	2.3e-06	1.39 sec	2.4e-06	9.0e-06
400	200	0.16 sec	4.1e-07	1.8e-07	1.77 sec	1.6e-07	6.1e-07
600	300	0.26 sec	1.1e-08	4.9e-09	2.57 sec	1.3e-07	2.6e-07
800	400	0.36 sec	2.2e-11	3.1e-10	3.40 sec	6.7e-08	4.8e-08

[a]The exact value of the Wood-Anomaly frequency $\mathrm{k} = 6(1 - \sin(45^\circ))^{-1}$ was used.

(from the first to the last row in the table) suffices to increase the solution accuracy by six additional digits. And, concerning efficiency, the table displays computing times that grow in a slower-than-linear fashion as the discretizations parameters N and n_{per} are increased. (As indicated above, the accelerator parameter $n_{\text{eq}} = 10$ is kept fixed: the resulting rather-coarse discretization suffices to produce all accuracies displayed in Table 2.6.1.)

Figure 2.6.1: Depiction of the solution of the Wood-anomaly problem considered in Table 2.6.1. This solution resulted from a 0.9 sec. computation, which included the evaluation of the scattered field displayed.

2.6.3 Sinusoidal Gratings

In order to illustrate the performance of the proposed solver for a wide range of problem parameters we consider a Littrow mount configuration of order -1 (the $n = -1$ diffracted mode is backscattered [55]), with incidence angle θ given by $\sin(\theta) = \frac{1}{3}$, for the sinusoidal surface

$$f(x) = \frac{H}{2}\sin(2\pi x/d), \qquad x \in (0, d),$$

and with $H = \frac{d}{4}$ (Tables 2.6.2 and 2.6.5), $H = \frac{d}{2}$ (Tables 2.6.3 and 2.6.6) and $H = d$ (Tables 2.6.4 and 2.6.7). In the Wood cases the wavenumber k varies from the first Wood frequency (k = 1.5) up to the sixth one (k = 9). As in the previous section, the accelerator parameters $L = \lambda$, $n_{\text{eq}} = 10$, $n_{\text{plw}} = 35$ and $n_{\text{coll}} = 200$ were used in all cases. Tables 2.6.2, 2.6.3 and 2.6.4 (resp. Tables 2.6.5, 2.6.6 and 2.6.7) correspond to non-Wood (resp. Wood) configurations. The first row in each one of these tables corresponds to test problems considered in [15, Tables 3-7].

The columns "Iter. time" and "# Iters." display the computing time required by each full solver iteration and the total number of iterations required to reach the energy balance tolerance ε. The columns "G_0^{qper} eval." and "Init. time", in turn, list initialization times as described in Remark 2.6.1.

Table 2.6.2: Sinusoidal scatterer data for increasingly higher non-Wood frequencies; $H = \frac{d}{4}$, $j = 0$.

H/λ	d/λ	N	n_{per}	G_0^{qper} eval.	Init. time	Iter. time	# Iters.	Total time	ε
0.25	1.00	48	110	0.01 sec	0.02 sec	2.9e-04 sec	7	0.02 sec	1.7e-08
0.62	2.50	76	110	0.01 sec	0.03 sec	5.8e-04 sec	10	0.04 sec	3.1e-08
1.00	4.00	120	110	0.01 sec	0.04 sec	1.2e-03 sec	12	0.06 sec	7.7e-08
1.38	5.50	166	110	0.01 sec	0.11 sec	1.0e-03 sec	13	0.13 sec	2.1e-08
1.75	7.00	210	110	0.02 sec	0.10 sec	1.1e-03 sec	14	0.12 sec	2.1e-08
2.12	8.50	256	110	0.02 sec	0.08 sec	2.2e-03 sec	15	0.12 sec	1.8e-09

Remark 2.6.1. *In Tables 2.6.2 and subsequent, the columns "Init. time" display the total initialization times—that is, the times required in each case by Algorithm 2 in Section 2.5.7. This time includes, in particular, the separately-listed "G_0^{qper} eval." time, which is the time required for the evaluation of all necessary values of the quasi-periodic Green function.*

Table 2.6.3: Sinusoidal scatterer data for increasingly higher non-Wood frequencies; $H = \frac{d}{2}$, $j = 0$.

H/λ	d/λ	N	n_{per}	G_0^{qper} eval.	Init. time	Iter. time	# Iters.	Total time	ε
0.50	1.00	64	120	0.01 sec	0.03 sec	6.2e-04 sec	8	0.03 sec	5.9e-08
1.25	2.50	106	120	0.01 sec	0.07 sec	5.6e-04 sec	13	0.07 sec	6.1e-08
2.00	4.00	168	120	0.01 sec	0.08 sec	1.4e-03 sec	18	0.10 sec	3.8e-09
2.75	5.50	232	120	0.01 sec	0.11 sec	2.1e-03 sec	21	0.15 sec	6.3e-09
3.50	7.00	294	120	0.02 sec	0.11 sec	2.5e-03 sec	23	0.17 sec	1.4e-09
4.25	8.50	358	120	0.02 sec	0.14 sec	3.1e-03 sec	26	0.22 sec	3.3e-09

Table 2.6.4: Sinusoidal scatterer data for increasingly higher non-Wood frequencies; $H = d$, $j = 0$.

H/λ	d/λ	N	n_{per}	G_0^{qper} eval.	Init. time	Iter. time	# Iters.	Total time	ε
1.00	1.00	76	150	0.01 sec	0.04 sec	4.1e-04 sec	12	0.05 sec	2.2e-08
2.50	2.50	126	150	0.01 sec	0.05 sec	1.2e-03 sec	18	0.08 sec	2.2e-08
4.00	4.00	200	150	0.02 sec	0.07 sec	2.3e-03 sec	26	0.13 sec	2.0e-08
5.50	5.50	276	150	0.02 sec	0.15 sec	3.7e-03 sec	32	0.27 sec	2.7e-09
7.00	7.00	350	150	0.02 sec	0.22 sec	8.1e-03 sec	39	0.54 sec	5.6e-09
8.50	8.50	426	150	0.03 sec	0.41 sec	9.3e-03 sec	46	0.84 sec	2.2e-09

The non-Wood examples considered in Tables 2.6.2, 2.6.3 and 2.6.4 demonstrate the performance of the proposed accelerated solver in absence of Wood anomalies: these results extend corresponding data tables presented in the recent reference [15], with better than single precision accuracy, to

Table 2.6.5: Sinusoidal scatterer data for increasingly higher Wood frequencies. $H = \frac{d}{4}$

H/λ	d/λ	N	h/λ	n_{per}	G_8^{qper} eval.	Init. time	Iter. time	# Iters.	Total time	ε
0.38	1.50	46	0.43	50	0.03 sec	0.05 sec	2.1e-04 sec	10	0.05 sec	4.5e-08
0.75	3.00	90	0.43	50	0.05 sec	0.09 sec	4.3e-04 sec	17	0.10 sec	7.8e-08
1.12	4.50	136	0.43	50	0.09 sec	0.15 sec	6.9e-04 sec	23	0.16 sec	8.3e-08
1.50	6.00	180	0.43	50	0.12 sec	0.17 sec	1.1e-03 sec	30	0.20 sec	9.0e-08
1.88	7.50	226	0.48	50	0.13 sec	0.21 sec	1.0e-03 sec	34	0.25 sec	3.1e-08
2.25	9.00	270	0.53	50	0.21 sec	0.29 sec	2.3e-03 sec	38	0.37 sec	5.9e-08

Table 2.6.6: Sinusoidal scatterer data for increasingly higher Wood frequencies. $H = \frac{d}{2}$

H/λ	d/λ	N	h/λ	n_{per}	G_8^{qper} eval.	Init. time	Iter. time	# Iters.	Total time	ε
0.75	1.50	90	0.36	200	0.09 sec	0.14 sec	4.0e-04 sec	15	0.15 sec	2.5e-08
1.50	3.00	180	0.48	200	0.29 sec	0.38 sec	1.2e-03 sec	23	0.41 sec	7.6e-08
2.25	4.50	270	0.69	400	0.68 sec	0.86 sec	1.9e-03 sec	26	0.91 sec	3.0e-08
3.00	6.00	360	0.69	400	1.13 sec	1.39 sec	3.0e-03 sec	34	1.49 sec	3.3e-08
3.75	7.50	450	0.74	600	1.92 sec	2.22 sec	2.6e-03 sec	40	2.33 sec	3.9e-08
4.50	9.00	540	0.77	600	3.24 sec	3.59 sec	5.1e-03 sec	46	3.83 sec	2.3e-08

Table 2.6.7: Sinusoidal scatterer data for increasingly higher Wood frequencies. $H = d$

H/λ	d/λ	N	h/λ	n_{per}	G_8^{qper} eval.	Init. time	Iter. time	# Iters.	Total time	ε
1.50	1.50	200	0.36	400	0.18 sec	0.50 sec	7.6e-04 sec	27	0.52 sec	2.8e-09
3.00	3.00	400	0.57	650	0.83 sec	1.48 sec	2.0e-03 sec	37	1.56 sec	1.7e-08
4.50	4.50	600	0.79	1000	1.87 sec	3.20 sec	3.1e-03 sec	46	3.34 sec	1.5e-08
6.00	6.00	800	0.86	1500	4.86 sec	6.52 sec	9.6e-03 sec	59	7.09 sec	6.4e-08
7.50	7.50	1000	0.90	2000	8.29 sec	10.67 sec	9.2e-03 sec	74	11.35 sec	5.8e-07
9.00	9.00	1200	0.86	2500	17.22 sec	19.81 sec	9.8e-03 sec	88	20.68 sec	3.2e-08

problems that are up to eight times higher in frequency and depth in comparable sub-second, single-core computing times (cf. Tables 2, 3 and 4 in [15]). High accuracy and speed are also demonstrated in the Wood-anomaly cases considered in Tables 2.6.5, 2.6.6 and 2.6.7. With exception of the first row in each one of these tables, for which comparable performance was demonstrated in [15], none of these problems had been previously treated in the literature. These tables demonstrate that better than single precision accuracy is again produced by the proposed methods at the expense of modest computing costs.

Increases by factors of 2.5 to 25 are observed in the "Total time" columns of the Wood-anomaly tables in this section relative to the corresponding columns in the non-Wood tables, with cost-factor increases that grow as $\frac{H}{d}$ and/or $\frac{H}{\lambda}$ grow. The cost increases at Wood frequencies, which can be tracked down directly to the cost required of evaluation of the shifted Green function, are most marked for deep gratings—which, as discussed in Section 2.6.1, require use of adequately enlarged values of the shift parameter h to avoid near singularity and ill conditioning, and which therefore require use of larger numbers n_{per} of terms for the summation of the shifted quasi-periodic Green function $\tilde{G}_j^{qper}$.

2.6.4 Large random rough surfaces under near-grazing incidence

This section demostrates the character of the proposed algorithm in the context of randomly rough Gaussian surfaces under near-grazing illumination. At exactly grazing incidence, $\theta = 90°$, the zero-th efficiency becomes a Wood anomaly—a challenge which underlies the significant difficulties classically found in the solution of *near grazing* periodic rough-surface scattering problems.

Various techniques [45, 70] based on tapering of either the incident field, or the surface, or both, have been proposed to avoid the nonphysical edge diffraction which arises as an infinite random surfaces is truncated to a bounded computational domain. Unfortunately, the modeling errors introduced by this approximation are strongly dependent on the incidence angle and the size of the truncated section [45, 70]. Consideration of periodic surfaces [27] provides an alternative that does not suffer from this difficulty. However, periodic-surface approaches have only occasionally been pursued in the context of random surfaces, on the basis that while [45] "periodic surfaces [allow use of] plane wave incident fields without angular resolution problems [...] these techniques do not simultaneously model a full range of ocean length scales for microwave and higher frequencies". Thus, the contribution [45] proposes use of a taper—an approach which has been influential in the subsequent literature [70]. As demonstrated in this section, the proposed periodic-surface solvers can tackle wide ranges of length-scales, thus eliminating the disadvantages of the periodic simulation method while maintaining its main strength: direct simulation of an unbounded randomly rough surface.

The character of the proposed solvers in the random-surface context is demonstrated by means of a range of challenging numerical examples. Throughout this section surface "heights" are quantified in terms of the surface's root-mean-square height (rms). For definiteness, all test cases concern randomly-rough Gaussian surfaces [35, p. 124] with correlation length equal to the electromagnetic wavelength λ; examples for various period-to-wavelength and height-to-wavelength ratios are used to demonstrate the computing-time scaling of the algorithm. Equispaced meshes of meshsize $\Delta x = \lambda/10$ (Section 2.4.2) were used for all the examples considered in this section.

Table 2.6.8: Gaussian surface with $\theta = 89.9°$, $H = \frac{\lambda}{2}$ mean rms.

d/λ	n_{per}	G_8^{qper} eval.	Init. time	Iter. time	# Iters.	Total time	ε
25	1600	4.16 sec	6.89 sec	3.5e-03 sec	103	7.39 sec	1.8e-08
50	800	3.76 sec	6.66 sec	7.1e-03 sec	209	8.03 sec	2.5e-07
100	400	3.62 sec	8.77 sec	1.3e-02 sec	360	13.81 sec	3.2e-08
200	200	3.70 sec	14.56 sec	2.6e-02 sec	680	33.10 sec	4.6e-08
300	133	4.06 sec	20.13 sec	3.8e-02 sec	973	57.93 sec	3.2e-08
400	100	4.48 sec	26.77 sec	5.5e-02 sec	1242	96.02 sec	4.6e-08

Table 2.6.8 presents computing times and accuracies for problems of scattering by Gaussian surfaces of rms-height equal to $\lambda/2$ under close-to-grazing incidence $\theta = 89.9°$. The data displayed in this table demonstrates uniform accuracy, with fixed meshsize, for periods going from twenty-five to four-hundred wavelengths in size. Certain useful characteristics of the algorithm may be

gleaned from this table. On one hand, the "time" columns in the table show that, as indicated in Section 2.1 and discussed in Section 2.6.1, the computing costs for a fixed accuracy grow at most linearly with the surface period d/λ. The "G_8^{qper} eval." data, in turn, shows that the cost of evaluation of the shifted Green function G_j^{qper} with $j = 8$ remains essentially constant as the size of the surface grows—and that, therefore, the Green-function cost becomes negligible, when compared to the total cost, for sufficiently large surfaces. The ε error column demonstrates the high accuracy of the method.

Remark 2.6.2. *The "constant-cost" observed for the computation of G_8^{qper} in Table 2.6.8 can be understood as follows. As noted in section 2.3.2, the efficiency of the spectral series is inversely proportional to parameter $\frac{\delta}{d}$, where δ is the distance from Y to the set of polar points $\{-mh, 0 \leq m \leq j\}$. As the period d grows the quotient $\frac{\delta}{d}$ decreases, and, therefore, the trade-off in the hybrid strategy increasingly favors the use of the spatial series—which as demonstrated by the n_{per} column in Table 2.6.8, requires smaller and smaller values of n_{per} as the period is increased, to meet a given error tolerance.*

Figure 2.6.2 displays scattered fields produced by increasingly *larger and steeper* Gaussian surfaces under 89° near-grazing incidence. The ε error is in all cases of the order of 10^{-9}, and the computing times reported in the figure caption include the computation of the displayed near field.

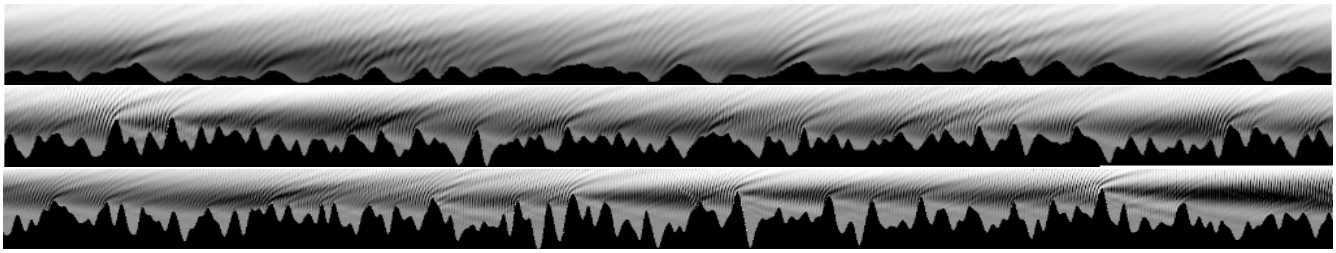

Figure 2.6.2: Gaussian rough surfaces under $\theta = 89°$ incidence, with simulation errors $\varepsilon < 10^{-8}$ in all cases. Top: $d = 100\lambda$, $H = \frac{\lambda}{2}$ mean rms (2.6λ peak-to-trough). Center: $d = 200\lambda$, $H = \lambda$ mean rms (6.7λ peak-to-trough). Bottom: $d = 1000\lambda$ (fragment), $H = 2\lambda$ mean rms (14.3λ peak-to-trough). Computing time (including near field evaluation) is 22.3 sec., 62.9 sec. and 830 sec. respectively.

2.6.5 Comparison with [17] for some "extreme" problems

A number of fast and accurate solutions were provided in [17] for highly-challenging grating-scattering problems (in configurations away from Wood Anomalies); relevant performance comparisons with results in that contribution are presented in what follows. While the results of [17] ensure accuracies of the order of ten to twelve digits, the solver introduced in the present thesis was restricted, for definiteness, to accuracies of the order of single-precision. Fortunately, however, Table 8 in [17] presents a convergence study for a problem of scattering by a composite surface. That table shows that the method [17] requires 85 seconds to reach single precision accuracy for

this problem; the present approach, in contrast, reaches the same precision for the same problem in just 1.8 seconds—including the evaluation of the near-field displayed in Figure 2.6.3.

Remark 2.6.3. *Higher accuracies can be produced by the present approach at moderate additional computational expense. In turn, results in Table 8 in [17] show that, for example, a reduction in accuracy from fourteen digits to single precision only produces a relatively small reduction in computing time—from 98 seconds to 85 seconds. This is a consequence, of course, of the high-order convergence of the method [17].*

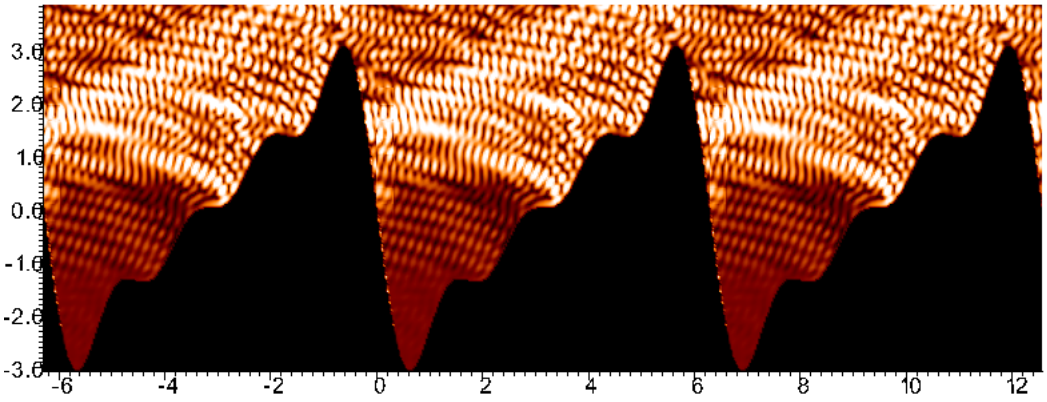

Figure 2.6.3: Depiction of the solution of the considered in Table 8 of [17]. This solution resulted from a 1.8 sec. computation, which included the evaluation of the scattered field displayed.

As an additional example we consider Table 5 in [17]. That table presents results for extremely deep sinusoidal gratings with $\lambda = 0.05$ and incidence angle $\theta = 70°$. The corresponding accuracies and computing times produced for those configurations by the present solvers are presented in Table 2.6.9. Comparison of the tabulated data shows significant improvements in computing times, by factors of 12 to 25, at the expense of a few digits of accuracy; see Remark 2.6.3.

Table 2.6.9: Increasingly deep gratings with a fixed period, and with incidence angle $\theta = 70°$.

h/λ	d/λ	N	G_0^{qper} eval.	Init. time	Iter. time	# Iters.	Total time	ε
160	20	800	0.74 sec	1.59 sec	0.08 sec	633	0.84 min	5.9e-08
320	20	1600	1.01 sec	3.31 sec	0.15 sec	1260	3.30 min	5.3e-08
480	20	2400	1.28 sec	4.73 sec	0.26 sec	1881	8.21 min	2.6e-08
640	20	3200	1.59 sec	8.89 sec	0.35 sec	2507	14.88 min	6.1e-08
800	20	4000	1.97 sec	9.96 sec	0.43 sec	3148	22.83 min	8.0e-08

Table 7 in [17], finally, considers increasingly high frequencies while maintaining the other problem parameters fixed: $\theta = 45°$, $d = 1$, $h = 2$. A similar picture emerges in this case: the method [17] solves problems with accuracies of the order of 13 to 16 digits, at computing times that are larger than those displayed in Table 2.6.10 by factors of 10 to 18.

Table 2.6.10: Increasingly high frequencies, with $\theta = 45°$, $d = 1$, $h = 2$

h/λ	d/λ	N	G_0^{qper} eval.	Init. time	Iter. time	# Iters.	Total time	ε
20	10	200	0.55 sec	0.75 sec	0.01 sec	92	1.62 sec	4.1e-09
40	20	400	1.09 sec	1.51 sec	0.02 sec	167	5.02 sec	1.7e-08
200	100	2000	11.57 sec	13.64 sec	0.25 sec	477	133.67 sec	3.8e-11
400	200	4000	122.78 sec	128.25 sec	1.00 sec	698	824.82 sec	2.4e-09

2.7 Conclusions

The periodic-scattering solver introduced in this thesis provides the first accelerated solver of high-order of accuracy for the solution of problems of scattering by periodic surfaces up to and including Wood frequencies. The algorithm relies on use of an accelerated shifted Green function methodology which reduces operator evaluations to Fast Fourier Transforms, and which, in particular, greatly reduces the required number of evaluations of the shifted quasi-periodic Green function. Significant additional acceleration is obtained by the solver by means of an appropriate application of a dual spectral/spatial approach for evaluation of the shifted Green function—which exploits, when possible, the exponentially fast convergence of the spectral series, and which relies on the high-order-convergent shifted spatial series for points for which the convergence of the spectral series deteriorates. The combined solver is highly efficient: it enables fast and accurate solution of some of the most challenging two-dimensional periodic scattering problems arising in practice. A three-dimensional version of this approach has been found equally effective, and will the subject of a subsequent contribution.

Acknowledgment

OB gratefully acknowledges support by NSF and AFOSR and DARPA through contracts DMS-1411876 and FA9550-15-1-0043 and HR00111720035, and the NSSEFF Vannevar Bush Fellowship under contract number N00014-16-1-2808. MM work was supported from a PhD fellowship of CONICET and the Bec.AR-Fullbright Argentine Presidential Fellowship in Science and Technology.

2.8 Appendix: Convergence and error analysis

An error analysis for the numerical method embodied in equation (2.4.31) follows from the standard stability result [46, Th.10.12]. The following lemma establishes the crucial new element necessary to produce a convergence estimate specific to equation (2.4.31), namely, an error estimate for the combined smooth windowing and trapezoidal quadrature for the operator $\tilde{D}_{\text{reg}}$ (all other needed estimates can be found in reference [46]). Throughout this section the notations in Section 2.4.2 are used together with the shorthand $\vec{\mu} = [\mu(x_1), \ldots, \mu(x_N)]$ for a given quasi-periodic function μ.

Lemma 2.8.1. *Let $d > 0$ and $\alpha \geq 0$, and let μ denote an infinitely differentiable α-quasi-periodic function of quasi-period $[0, d]$. Then, $\tilde{D}_{\text{reg}}^{A,\Delta x}[\vec{\mu}](x)$ tends to $\tilde{D}_{\text{reg}}[\mu](x)$, uniformly for $x \in [0, d]$, as*

$A \to \infty$ and $\Delta x \to 0$. More precisely, we have

$$|\tilde{D}_{\text{reg}}[\mu](x) - \tilde{D}_{\text{reg}}^{A,\Delta x}[\vec{\mu}](x)| \leq E_p(\Delta x)^p + C_q A^{-q} \quad (1 \leq i \leq N), \tag{2.8.1}$$

for all positive integers p, and with $q = \left\lfloor \frac{j+1}{2} \right\rfloor - \frac{1}{2}$ near Wood anomalies, and for all positive integers q away from Wood-anomaly frequencies. Here C_q and E_p are constants that do not depend on either A or Δx. We also have the error estimate

$$|\tilde{D}_{\text{reg}}[\mu](x) - \tilde{D}_{\text{reg}}^{\Delta x}[\vec{\mu}](x)| \leq E_p(\Delta x)^p \quad \textit{for all } p \in \mathbb{N}. \tag{2.8.2}$$

Proof. Let us consider the triangle-inequality estimate

$$|\tilde{D}_{\text{reg}}[\mu](x) - \tilde{D}_{\text{reg}}^{A,\Delta x}[\vec{\mu}](x)| \leq |\tilde{D}_{\text{reg}}[\mu](x) - \tilde{D}_{\text{reg}}^{A}[\mu](x)| + |\tilde{D}_{\text{reg}}^{A}[\mu](x) - \tilde{D}_{\text{reg}}^{A,\Delta x}[\vec{\mu}]|. \tag{2.8.3}$$

The first term on the right hand side of this relation admits the bound

$$|\tilde{D}_{\text{reg}}[\mu](x) - \tilde{D}_{\text{reg}}^{A}[\mu](x)| \leq C_q A^{-q}, \tag{2.8.4}$$

for certain values of q, as indicated as follows. For frequencies k away from Wood anomalies, on one hand, the Green function series converges at a superalgebraic rate as $A \to \infty$ [15], (faster than A^{-q} for any integer q), for all integers $j \geq 0$ (including the "unshifted" case $j = 0$), and thus so does $\tilde{D}_{\text{reg}}^{A}[\mu]$. In other words, away from Wood anomalies, the bound (2.8.4) holds for all positive integers q. For frequencies k up to and including Wood anomalies, on the other hand, reference [15] shows that for a given integer $j \geq 1$, the Green function series enjoys algebraic convergence, with errors of the order of A^{-q}) with $q = (j-1)/2$ for j even, and with $q = j/2$ for j odd. It follows that, up to an including Wood anomalies, for a given $j \geq 1$ the bound (2.8.4) holds with $q = \left\lfloor \frac{j+1}{2} \right\rfloor - \frac{1}{2}$.

Having obtained the estimate (2.8.4) for the first term on the right-hand side of (2.8.3) under the various frequency regimes, we now turn to the second term on that right-hand side. To estimate this term, we first consider the smooth $2A$-periodic function $F^{A,x} = F^{A,x}(x')$ (which, as indicated in Remark 2.4.2, coincides with the integrand in equation (2.4.21)), and we show that the coefficients

$$F_n^{A,x} = \frac{1}{2A} \int_{-A}^{A} F^{A,x}(x') e^{-\frac{\pi i}{A} n x'} dx' \tag{2.8.5}$$

of the Fourier series

$$F^{A,x}(x') = \sum_{n=-\infty}^{\infty} F_n^{A,x} e^{\frac{\pi i}{A} n x'} \tag{2.8.6}$$

converge to zero rapidly and uniformly in A and x as $n \to \infty$. Indeed, using integration by parts p times in (2.8.6) we see that

$$|F^{A,x}(x')| \leq C_p^{A,x} \left(\frac{A}{n} \right)^p \tag{2.8.7}$$

where $C_p^{A,x}$ is an upper bound for the absolute value of the product of π^p and the p-th derivative of $F^{A,x}(x')$ with respect to x'. But, considering the expression that defines $F^{A,x}(x')$, namely, the integrand in (2.4.21), we see that the p-th order derivative of $F^{A,x}(x')$ with respect to x' is bounded

by a constant which does not depend on A or x—since the same is true of each of the four functions in (2.4.21) whose products equals $F^{A,x}$. We thus obtain, for each non-negative integer p, the bound

$$|F_n^{A,x}| < C_p \left(\frac{A}{n}\right)^p, \tag{2.8.8}$$

where the constant C_p depends on p only. Since $F^{A,x}(x')$ is (a periodic extension of) the integrand in (2.4.21), we see that $\tilde{D}^A_{\mathrm{reg}}[\mu]$ equals the zero-th order coefficient of $F^{A,x}(x')$:

$$\tilde{D}^A_{\mathrm{reg}}[\mu] = F_0^{A,x}. \tag{2.8.9}$$

The discrete approximation $D^{A,\Delta x}_{\mathrm{reg}}[\vec{\mu}](x)$ in (2.4.24), in turn, utilizes in the periodicity interval $[x-A, x+A]$ a number N_A of discretization points that satisfies the relations

$$\lfloor A/d \rfloor N \le N_A \le \lceil A/d \rceil N \tag{2.8.10}$$

where, for a real number r, $\lceil r \rceil$ (resp. $\lfloor r \rfloor$) denotes the smallest integer larger than or equal to r (resp. the largest integer smaller than or equal to r). For a given period d we clearly have

$$N_A = O\left(\frac{A}{N}\right). \tag{2.8.11}$$

As is well known (and easily checked), the N_A-point discrete trapezoidal-rule quadrature inherent in equation (2.4.24) integrates correctly all the non-aliased harmonics in equation (2.8.6), and it produces the value one for the aliased harmonics. We thus obtain

$$D^{A,\Delta x}_{\mathrm{reg}}[\vec{\mu}] = \sum_{\ell=-\infty}^{\infty} F^{A,x}_{\ell N_A}. \tag{2.8.12}$$

In view of (2.8.8), (2.8.9) and (2.8.12) it follows that

$$|\tilde{D}^A_{\mathrm{reg}}[\mu](x) - \tilde{D}^{A,\Delta x}_{\mathrm{reg}}[\vec{\mu}]| = \left| \sum_{\substack{\ell=-\infty \\ \ell\neq 0}}^{\infty} F^{A,x}_{\ell N_A} \right| \le C_p \left(\frac{A}{N_A}\right)^p \sum_{\substack{\ell=-\infty \\ \ell\neq 0}}^{\infty} \ell^{-p} \tag{2.8.13}$$

which, in view of (2.8.10) and since $\Delta x \sim 1/N$, for $p \ge 2$ shows that

$$|\tilde{D}^A_{\mathrm{reg}}[\mu](x) - \tilde{D}^{A,\Delta x}_{\mathrm{reg}}[\vec{\mu}](x)| \le E_p (\Delta x)^p \tag{2.8.14}$$

for some constant E_p, as desired. The proof is now complete. □

Chapter 3

High order Nyström solvers for the Fractional Laplacian operator

3.1 Problem setup

The present chapter addresses theoretical questions and puts forth algorithms for the numerical solution of the Dirichlet problem

$$\begin{cases} (-\Delta)^s u = f & \text{in } \Omega, \\ u = 0 & \text{in } \Omega^c \end{cases} \tag{3.1.1}$$

on a bounded one-dimensional domain Ω consisting of a union of a finite number of intervals (whose closures are assumed mutually disjoint). This approach to enforcement of (nonlocal) boundary conditions in a bounded domain Ω arises naturally in connection with the long jump random walk approach to the Fractional Laplacian [78]. In such random walk processes, jumps of arbitrarily long distances are allowed. Thus, the payoff of the process, which corresponds to the boundary datum of the Dirichlet problem, needs to be prescribed in Ω^c.

Letting s and n denote a real number ($0 < s < 1$) and the spatial dimension ($n = 1$ throughout this chapter), and using the normalization constant [61]

$$C_n(s) = \frac{2^{2s} s \Gamma(s + \frac{n}{2})}{\pi^{n/2} \Gamma(1 - s)},$$

the fractional-Laplacian operator $(-\Delta)^s$ is given by

$$(-\Delta)^s u(x) = C_n(s) \text{ P.V.} \int_{\mathbb{R}^n} \frac{u(x) - u(y)}{|x - y|^{n+2s}} \, dy. \tag{3.1.2}$$

The development and analysis of high order numerical methods for this problems is quite challenging: in fact, prior to the present contribution (see also our related work [4]), the best algorithm presented in the literature for this problem [3] had only linear convergence. The analysis developed in the present chapter leads to a Gegenbauer-based Nyström discretization that, in particular, converges *exponentially fast* for analytic right-hand sides.

The first step in the development of this algorithm is to obtain a factorization of solutions as a product of a certain edge-singular weight ω times a "regular" unknown. In order to do that, Section 3.3 presents an asymptotic analysis that leads to the characterization of the singular weight ω involved. Interestingly, characterizing the single-edge behavior in Section 3.3.1 does not suffice to fully characterize the asymptotic behavior of the singularity, leading to an ambiguity in the possible singular exponents: s or $2s$. Section 3.3.2, finally, establishes that the correct exponent that characterizes the singularity to all orders is s. This analysis, further, leads to a full eigendecomposition for a certain *weighted integral operator*, in terms of the Gegenbauer polynomial basis (with weight exponent equal to s), which is obtained in Section 3.4.

Section 3.5, in turn, studies the "regular" unknown: a characterization of the regularity of solutions in terms of the smoothness of the corresponding right-hand sides, in various function spaces. In particular, for right-hand sides which are analytic in a Bernstein Ellipse, analyticity in the same Bernstein Ellipse is obtained for the "regular" unknown. Moreover, a sharp Sobolev regularity result is presented which completely characterizes the co-domain of the Fractional-Laplacian operator in terms of certain weighted Sobolev spaces introduced by Babuška and Guo in [8]. Additionally, a weighted-space version of the Sobolev lemma is presented in that section, which establishes the classical regularity of solutions in the proposed Sobolev spaces of sufficiently high order.

On the basis of this theory, Section 3.6 presents a highly accurate and efficient numerical solver for Fractional-Laplacian equations posed on a union of finitely many one-dimensional intervals. The sharp error estimates presented in Section 3.6 indicate that the proposed algorithm is spectrally accurate, with convergence rates that only depend on the smoothness of the right-hand side. In particular, the exponentially fast convergence (resp. faster than any power of the mesh-size) for analytic (resp. infinitely smooth) right-hand sides is rigorously established.

The treatment for this problem is presented in this Chapter in an essentially self-contained manner. This approach recasts the problem as an integral equation in a bounded domain, and it proceeds by computing certain singular exponents α that make $(-\Delta)^s(\omega^\alpha \phi(x))$ analytic near the boundary for every polynomial ϕ. As shown in Theorem 3.3.7 a infinite sequence of such values of α is given by $\alpha_n = s + n$ for all $n \geq 0$. Morever, Section 3.3.2 shows that the weighted operator K_s maps polynomials of degree n into polynomials of degree n—and it provides explicit closed-form expressions for the images of each polynomial ϕ.

A certain hypersingular form we present for the operator K_s leads to consideration of a weighted L^2 space wherein K_s is self-adjoint. In view of the aforementioned polynomial-mapping properties of the operator K_s it follows that this operator is diagonal in a basis of orthogonal polynomials with respect to a corresponding inner product. A related diagonal form was obtained in the recent independent contribution [37] by employing arguments based on Mellin transforms. The diagonal form [37] provides, in particular, a family of explicit solutions in the n dimensional ball in $\mathbb{R}^n$, which are given by products of the singular term $(1 - |z|^2)^s$ and general Meijer G-Functions. The diagonalization approach proposed in this Chapter, which is restricted to the one-dimensional case, is elementary and is succinctly expressed: the eigenfunctions are precisely the Gegenbauer polynomials.

A variety of numerical results presented in Section 3.7 demonstrate the character of the proposed solver: the new algorithm is significantly more accurate and efficient than those resulting from previous approaches.

3.2 Hypersingular Integral Equation Formulation

In this section the one-dimensional operator

$$(-\Delta)^s u(x) = C_1(s)\ \text{P.V.} \int_{-\infty}^{\infty} (u(x) - u(x-y))\, |y|^{-1-2s} dy \tag{3.2.1}$$

together with Dirichlet boundary conditions outside the bounded domain Ω, is expressed as an integral over Ω. The Dirichlet problem (3.1.1) is then identified with a hypersingular version of Symm's integral equation; the precise statement is provided in Lemma 3.2.3 in the introduction. In accordance with Section 1.4, throughout this Chapter we assume the following definition holds.

Definition 3.2.1. *The domain Ω equals a finite union*

$$\Omega = \bigcup_{i=1}^{M} (a_i, b_i) \tag{3.2.2}$$

of open intervals (a_i, b_i) with disjoint closures. We denote $\partial\Omega = \{a_1, b_1, \ldots, a_M, b_M\}$.

Definition 3.2.2. *$C_0^2(\Omega)$ will denote, for a given open set $\Omega \subset \mathbb{R}$, the space of all functions $u \in C^2(\Omega) \cap C(\mathbb{R})$ that vanish outside of Ω. For $\Omega = (a, b)$ we will simply write $C_0^2((a, b)) = C_0^2(a, b)$.*

The following Lemma provides a useful expression for the Fractional Laplacian operator in terms of integro-differential operators; For clarity the result is presented for the case $\Omega = (a, b)$; the generalization to domains Ω of the form (3.2.2) then follows easily in Corollary 3.2.5.

Lemma 3.2.3. *Let $s \in (0, 1)$, let $u \in C_0^2(a, b)$ such that $|u'|$ is integrable in (a, b), let $x \in \mathbb{R}, x \notin \partial\Omega = \{a, b\}$, and define*

$$C_s = \frac{C_1(s)}{2s(1-2s)} = -\Gamma(2s-1)\sin(\pi s)/\pi \quad (s \neq 1/2); \tag{3.2.3}$$

We then have

— *Case $s \neq \frac{1}{2}$:*

$$(-\Delta)^s u(x) = C_s \frac{d}{dx} \int_a^b |x-y|^{1-2s} \frac{d}{dy} u(y) dy. \tag{3.2.4}$$

— *Case $s = \frac{1}{2}$:*

$$(-\Delta)^{1/2} u(x) = \frac{1}{\pi} \frac{d}{dx} \int_a^b \ln|x-y| \frac{d}{dy} u(y) dy. \tag{3.2.5}$$

Lemma 3.2.3 enables to cast problem (3.1.1) as the integral equation problem

$$C_s \frac{d}{dx} \int_a^b |x-y|^{1-2s} \frac{d}{dy} u(y) dy = f(x) \tag{3.2.6}$$

Proof. We note that, since the support of $u = u(x)$ is contained in $[a, b]$, for each $x \in \mathbb{R}$ the support of the translated function $u = u(x - y)$ as a function of y is contained in the set $[x - b, x - a]$. Thus, using the decomposition $\mathbb{R} = [x - b, x - a] \cup (-\infty, x - b) \cup (x - a, \infty)$ in (3.2.1), we obtain the following expression for $(-\Delta)^s u(x)$:

$$C_1(s)\left(\text{P.V.}\int_{x-b}^{x-a}(u(x)-u(x-y))|y|^{-1-2s}dy+\left[\int_{-\infty}^{x-b}dy+\int_{x-a}^{\infty}dy\right]u(x)|y|^{-1-2s}\right). \tag{3.2.7}$$

We consider first the case $x \notin [a, b]$, for which (3.2.7) becomes

$$-C_1(s)\left(\text{P.V.}\int_{x-b}^{x-a}u(x-y)|y|^{-1-2s}dy\right). \tag{3.2.8}$$

Noting that the integrand (3.2.8) is smooth, integration by parts yields

$$\frac{C_1(s)}{2s}\int_{x-b}^{x-a}u'(x-y)\,\text{sgn}(y)|y|^{-2s}dy \tag{3.2.9}$$

(since $u(a) = u(b) = 0$), and, thus, letting $z = x - y$ we obtain

$$(-\Delta)^s u(x) = \frac{C_1(s)}{2s}\int_a^b \text{sgn}(x-z)|x-z|^{-2s}u'(z)dz \quad , \quad x \notin [a,b]. \tag{3.2.10}$$

Then, letting

$$\Phi_s(y) = \begin{cases} |y|^{1-2s}/(1-2s) & \text{for } s \in (0,1),\ s \neq 1/2 \\ \log|y| & \text{for } s = 1/2 \end{cases},$$

noting that

$$\text{sgn}(x-z)|x-z|^{-2s} = \frac{\partial}{\partial x}\Phi_s(x-z), \tag{3.2.11}$$

replacing (3.2.11) in (3.2.10) and exchanging the x-differentiation and z-integration yields the desired expressions (3.2.4) and (3.2.5). This completes the proof in the case $x \notin [a, b]$.

Let us now consider the case $x \in (a, b)$. The second term in (3.2.7) can be computed exactly; we clearly have

$$\left[\int_{-\infty}^{x-b}dy+\int_{x-a}^{\infty}dy\right]u(x)|y|^{-1-2s} = \left[\frac{u(x)}{2s}\,\text{sgn}(y)|y|^{-2s}\Big|_{y=x-b}^{y=x-a}\right]. \tag{3.2.12}$$

In order to integrate by parts in the P.V. integral in (3.2.7) consider the set

$$D_\varepsilon = [x-b, x-a] \setminus (-\varepsilon, \varepsilon).$$

Then, defining

$$Q_\epsilon(x) = \int_{D_\epsilon}(u(x)-u(x-y))\,|y|^{-1-2s}dy$$

integration by parts yields

$$Q_\epsilon(x) = -\frac{1}{2s}\left(g_a^b(x) - h_a^b(x) - \frac{\delta_\varepsilon^2}{\varepsilon^{2s}} - \int_{D_\epsilon}u'(x-y)\,\text{sgn}(y)|y|^{-2s}dy\right)$$

where $\delta_\varepsilon = u(x+\varepsilon) + u(x-\varepsilon) - 2u(x)$, $g_a^b(x) = u(x)(|x-a|^{-2s} + |x-b|^{-2s})$ and $h_a^b(x) = u(a)|x-a|^{-2s} + u(b)|x-b|^{-2s}$.

The term $h_a^b(x)$ vanishes since $u(a) = u(b) = 0$. The contribution $g_a^b(x)$, on the other hand, exactly cancels the boundary terms in equation (3.2.12). For the values $x \in (a,b)$ under consideration, a Taylor expansion in ε around $\varepsilon = 0$ additionally tells us that the quotient $\frac{\delta_\varepsilon^2}{\varepsilon^{2s}}$ tends to 0 as $\varepsilon \to 0$. Therefore, using the change of variables $z = x - y$ and letting $\varepsilon \to 0$ we obtain a principal-value expression valid for $x \neq a, x \neq b$:

$$(-\Delta)^s u(x) = \frac{C_1(s)}{2s} \text{ P.V.} \int_a^b \operatorname{sgn}(x-z)|x-z|^{-2s} u'(z) dz. \tag{3.2.13}$$

Replacing (3.2.11) in (3.2.13) then yields (3.2.4) and (3.2.5), provided that the derivative in x can be interchanged with the P.V. integral. This interchange is indeed correct, as it follows from an application of the following Lemma to the function $v = u'$. The proof is thus complete. □

Lemma 3.2.4. *Let $\Omega \subset \mathbb{R}$ be as indicated in Definition 3.2.1 and let $v \in C^1(\Omega)$ such that v is absolutely integrable over Ω, and let $x \in \Omega$. Then the following relation holds:*

$$P.V. \int_\Omega \frac{\partial}{\partial x} \Phi_s(x-y) v(y) dy = \frac{\partial}{\partial x} \int_\Omega \Phi_s(x-y) v(y) dy \tag{3.2.14}$$

Proof. See Appendix 3.8.1. □

Corollary 3.2.5. *Given a domain Ω as in Definition* (3.2.1)*, and with reference to equation* (3.2.3)*, for $u \in C_0^2(\Omega)$ and $x \notin \partial\Omega$ we have*

— *Case $s \neq \frac{1}{2}$:*

$$(-\Delta)^s u(x) = C_s \frac{d}{dx} \sum_{i=1}^M \int_{a_i}^{b_i} |x-y|^{1-2s} \frac{d}{dy} u(y) dy \tag{3.2.15}$$

— *Case $s = \frac{1}{2}$:*

$$(-\Delta)^{1/2} u(x) = \frac{1}{\pi} \frac{d}{dx} \sum_{i=1}^M \int_{a_i}^{b_i} \ln|x-y| \frac{d}{dy} u(y) dy \tag{3.2.16}$$

for all $x \in \mathbb{R} \setminus \partial\Omega = \cup_i^M \{a_i, b_i\}$.

Proof. Given $u \in C_0^2(\Omega)$ we may write $u = \sum_i^M u_i$ where, for $i = 1, \ldots, M$ the function $u_i = u_i(x)$ equals $u(x)$ for $x \in (a_i, b_i)$ and and it equals zero elsewhere. In view of Lemma 3.2.3 the result is valid for each function u_i and, by linearity, it is thus valid for the function u. The proof is complete. □

Remark 3.2.6. *A point of particular interest arises as we examine the character of $(-\Delta)^s u$ with $u \in C_0^2(\Omega)$ for x at or near $\partial\Omega$. Both Lemma 3.2.3 and its corollary 3.2.5 are silent in these regards. For $\Omega = (a,b)$, for example, inspection of equation* (3.2.13) *leads one to generally expect that $(-\Delta)^s u(x)$ has an infinite limit as x tends to each one of the endpoints a or b. But this is not so for all functions $u \in C_0^2(\Omega)$. Indeed, as established in Section 3.4, the subclass of functions*

in $C_0^2(\Omega)$ for which there is a finite limit forms a dense subspace of a relevant weighted L^2 space. In fact, a dense subset of functions exists for which the image of the fractional Laplacian can be extended as an analytic function in the complete complex x variable plane. But, even for such functions, definition (3.2.1) *still generically gives $(-\Delta)^s u(x) = \pm\infty$ for $x = a$ and $x = b$. Results concerning functions whose Fractional Laplacian blows up at the boundary can be found in [1].*

The next section concerns the single-interval case ($M = 1$ in (3.2.15), (3.2.16)). Using translations and dilations the single interval problem in any given interval (a_1, b_1) can be recast as a corresponding problem in any desired open interval (a, b). For notational convenience two different selections are made at various points in Section 3.4, namely $(a, b) = (0, 1)$ in Sections 3.3.1 and 3.3.2, and $(a, b) = (-1, 1)$ in Section 3.4. The conclusions and results can then be easily translated into corresponding results for general intervals; see for example Corollary 3.4.5.

3.3 Asymptotic Analysis of the Boundary Singularity

Lemma 3.2.3 expresses the action of the operator $(-\Delta)^s$ on elements u of the space $C_0^2(\Omega)$ in terms of the integro-differential operators on the right-hand side of equations (3.2.4) and (3.2.5). A brief consideration of the proof of that lemma shows that for such representations to be valid it is essential for the function u to vanish on the boundary—as all functions in $C_0^2(a, b)$ do, by definition. Section 3.3.1 considers, however, the action under the integral operators on the right-hand side of equations (3.2.4) and (3.2.5) on certain functions u defined on $\Omega = (a, b)$ *which do not necessarily vanish at a or b.* To do this we study the closely related integral operators

$$S_s[u](x) := C_s \int_a^b \left(|x-y|^{1-2s} - (b-a)^{1-2s} \right) u(y) dy \quad (s \neq \frac{1}{2}), \tag{3.3.1}$$

$$S_{\frac{1}{2}}[u](x) := \frac{1}{\pi} \int_a^b \log\left(\frac{|x-y|}{b-a} \right) u(y) dy, \tag{3.3.2}$$

$$T_s[u](x) := \frac{\partial}{\partial x} S_s \left[\frac{\partial}{\partial y} u(y) \right] (x). \tag{3.3.3}$$

Remark 3.3.1. *The addition of the constant term $-(b-a)^{1-2s}$ in the integrand* (3.3.1) *does not have any effect in the definition of T_s: the constant $-(b-a)^{1-2s}$ only results in the addition of a constant term on the right-hand side of* (3.3.1)*, which then yields zero upon the outer differentiation in equation* (3.3.3)*. The integrand* (3.3.1) *is selected, however, in order to insure that the kernel of S_s (namely, the function $C_s\left(|x-y|^{1-2s} - (b-a)^{1-2s}\right)$) tends to the kernel of $S_{\frac{1}{2}}$ in* (3.3.2) *(the function $\frac{1}{\pi}\log(|x-y|/(b-a))$) in the limit as $s \to \frac{1}{2}$.*

Remark 3.3.2. *In view of Remark 3.3.1 and Lemma 3.2.4, for $u \in C^2(a, b)$ we additionally have*

$$T_s[u](x) = \frac{C_1(s)}{2s} \; P.V. \int_a^b \operatorname{sgn}(x-z)|x-z|^{-2s} u'(z) dz. \tag{3.3.4}$$

Remark 3.3.3. *The operator T_s coincides with $(-\Delta)^s$ for functions u that satisfy the hypothesis of Lemma 3.2.3, but T_s does not coincide with $(-\Delta)^s$ for functions u which, such as those we consider in Section 3.3.1 below, do not vanish on $\partial\Omega = \{a, b\}$.*

Remark 3.3.4. *The operator $S_{\frac{1}{2}}$ coincides with Symm's integral operator [75], which is important in the context of electrostatics and acoustics in cases where Dirichlet boundary conditions are posed on infinitely-thin open plates [19, 50, 75, 83]. The operator $T_{\frac{1}{2}}$, on the other hand, which may be viewed as a* hypersingular version *of the Symms operator $S_{\frac{1}{2}}$, similarly relates to electrostatics and acoustics, in cases leading to Neumann boundary conditions posed on open-plate geometries. The operators S_s and T_s in the cases $s \neq \frac{1}{2}$ can thus be interpreted as generalizations to fractional powers of classical operators in potential theory, cf. also Remark 3.3.3.*

Restricting attention to $\Omega = (a, b) = (0, 1)$ for notational convenience and without loss of generality, Section 3.3.1 studies the image $T_s[u_\alpha]$ of the function

$$u_\alpha(y) = y^\alpha \tag{3.3.5}$$

with $\Re\alpha > 0$—which is smooth in $(0, 1)$, but which has an algebraic singularity at the boundary point $y = 0$. That section shows in particular that, whenever $\alpha = s + n$ for some $n \in \mathbb{N} \cup \{0\}$, the function $T_s[u_\alpha](x)$ can be extended analytically to a region containing the boundary point $x = 0$. Building upon this result (and assuming once again $\Omega = (a, b) = (0, 1)$), Section 3.3.2, explicitly evaluates the images of functions of the form $v(y) = y^{s+n}(1 - y)^s$ $(n \in \mathbb{N} \cup \{0\})$, which are singular (not smooth) at the two boundary points $y = 0$ and $y = 1$, under the integral operators T_s and S_s. The results in Section 3.3.2 imply, in particular, that the image $T_s[v]$ for such functions v can be extended analytically to a region containing the interval $[0, 1]$. Reformulating all of these results in the general interval $\Omega = (a, b)$, Section 3.4 then derives the corresponding single-interval diagonal form for weighted operators naturally induced by T_s and S_s.

3.3.1 Single-edge singularity

With reference to equations (3.3.4) and (3.2.3), and considering the aforementioned function $u_\alpha(y) = y^\alpha$ we clearly have

$$T_s[u_\alpha](x) = \alpha(1 - 2s)C_s N^s_\alpha(x) \ \text{, where}$$
$$N^s_\alpha(x) := P.V. \int_0^1 \operatorname{sgn}(x - y)|x - y|^{-2s} y^{\alpha-1} dy. \tag{3.3.6}$$

As shown in Theorem 3.3.7 below (equation (3.3.12)), the functions N^s_α and (thus) $T_s[u_\alpha]$ can be expressed in terms of classical special functions whose singular structure is well known. Leading to the proof of that theorem, in what follows we present a sequence of two auxiliary lemmas.

Lemma 3.3.5. *Let $E = (a, b) \subset \mathbb{R}$, and let $C \subseteq \mathbb{C}$ denote an open subset of the complex plane. Further, let $f = f(t, c)$ be a function defined in $E \times C$, and assume 1) f is continuous in $E \times C$, 2) f is analytic with respect to $c = c_1 + ic_2 \in C$ for each fixed $t \in E$, and 3) f is "uniformly integrable over compact subsets of C"—in the sense that for every compact set $K \subset C$ the functions*

$$h_a(\eta, c) = \left| \int_a^{a+\eta} f(t, c)dt \right| \quad \text{and} \quad h_b(\eta, c) = \left| \int_{b-\eta}^{b} f(t, c)dt \right| \tag{3.3.7}$$

tend to zero uniformly for $c \in K$ as $\eta \to 0^+$. Then the function

$$F(c) := \int_E f(t,c)dt$$

is analytic throughout C.

Proof. Let K denote a compact subset of C. For each $c \in K$ and each $n \in \mathbb{N}$ we consider Riemann sums $R_n^h(c)$ for the integral of f in the interval $[a+\eta_n, b-\eta_n]$, where η_n is selected in such a way that $h_a(\eta_n, c) \leq 1/n$ and $h_b(\eta_n, c) \leq 1/n$ for all $c \in K$ (which is clearly possible in view of the hypothesis (3.3.7)). The Riemann sums are defined by $R_n^h(c) = h\sum_{j=1}^M f(t_j, c)$, with $h = (b-a+2\eta_n)/M$ and $t_{j+1} - t_j = h$ for all j.

Let $n \in \mathbb{N}$ be given. In view of the uniform continuity of $f(t,c)$ in the compact set $[a+\eta_n, b-\eta_n]\times K$, the difference between the maximum and minimum of $f(t,c)$ in each integration subinterval $(t_j, t_{j+1}) \subset [a+\eta_n, b-\eta_n]$ tends uniformly to zero for all $c \in K$ as the integration meshsize tends to zero. It follows that a meshsize h_n can be found for which the approximation error in the corresponding Riemann sum $R_n^h(c)$ is *uniformly small for all $c \in K$*:

$$\left| \int_{a+\eta_n}^{b-\eta_n} f(t,c)dt - R_n^h(c) \right| < \frac{1}{n} \quad \text{for all } c \in K \text{ and for all } n \in \mathbb{N}.$$

Thus $F(c)$ equals a uniform limit of analytic functions over every compact subset of C, and therefore $F(c)$ is itself analytic throughout C, as desired. □

Lemma 3.3.6. *Let $x \in (0,1)$ and let $g(s,\alpha) = N_\alpha^s(x)$ be defined by* (3.3.6) *for complex values of s and α satisfying $\Re s < 1$ and $\Re\alpha > 0$. We then have:*

(i) For each fixed α such that $\Re\alpha > 0$, $g(s,\alpha)$ is an analytic function of s for $\Re s < 1$; and

(ii) For each fixed s such that $\Re s < 1$, $g(s,\alpha)$ is an analytic of α for $\Re\alpha > 0$.

In other words, for each fixed $x \in (0,1)$ the function $N_\alpha^s(x)$ is jointly analytic in the (s,α) domain $D = \{\Re s < 1\} \times \{\Re\alpha > 0\} \subset \mathbb{C}^2$.

Proof. We express the integral that defines N_α^s as the sum $g_1(s,\alpha) + g_2(s,\alpha)$ of two integrals, each one of which contains only one of the two singular points of the integrand ($y = 0$ and $y = x$):

$$g_1 = \int_0^{x/2} \operatorname{sgn}(x-y)|x-y|^{-2s} y^{\alpha-1} dy \text{ and } g_2 = P.V. \int_{x/2}^1 \operatorname{sgn}(x-y)|x-y|^{-2s} y^{\alpha-1} dy.$$

Lemma 3.3.5 tells us that g_1 is an analytic function of s and α for $(s,\alpha) \in D_1 = \mathbb{C} \times \{\Re\alpha > 0\}$.

Integration by parts in the g_2 term, in turn, yields

$$(1-2s)g_2(s,\alpha) = (1-x)^{1-2s} - \left(\frac{x}{2}\right)^{\alpha-2s} - (\alpha-1)\int_{x/2}^1 |x-y|^{1-2s} y^{\alpha-2} dy. \tag{3.3.8}$$

But, writing the the integral on the right-hand side of (3.3.8) in the form $\int_{x/2}^1 = \int_{x/2}^x + \int_x^1$ and applying Lemma 3.3.5 to each one of the resulting integrals shows that the quantity $(1-2s)g_2(s,\alpha)$

is an analytic function of s and α for $(s,\alpha) \in D_2 = \mathbb{C} \times \{\alpha > 0\}$. In view of the $(1-2s)$ factor, however, it still remains to be shown that $g_2(s,\alpha)$ is analytic at $s = 1/2$ as well.

To check that both $g_2(s,\alpha)$ and $g(s,\alpha)$ are analytic around $s = 1/2$ for any fixed $\alpha \in \{\Re\alpha > 0\}$, we first note that since $\int_0^1 1 \cdot y^{\alpha-1}dy$ is a constant function of x we may write

$$g(s,\alpha) = \frac{1}{1-2s}\frac{\partial}{\partial x}\int_0^1 \left(|x-y|^{1-2s} - 1\right) y^{\alpha-1}dy.$$

But since we have the uniform limit

$$\lim_{s\to 1/2} \frac{|x-y|^{1-2s}-1}{1-2s} = \frac{\partial}{\partial r}|x-y|^r\Big|_{r=0} = \log|x-y|$$

as complex values of s approach $s = 1/2$, we see that g is in fact a continuous and therefore, by Riemann's theorem on removable singularities, analytic at $s = 1/2$ as well. The proof is now complete. □

Theorem 3.3.7. *Let $s \in (0,1)$ and $\alpha > 0$. Then $N_\alpha^s(x)$ can be analytically continued to the unit disc $\{x : |x| < 1\} \subset \mathbb{C}$ if and only if either $\alpha = s + n$ or $\alpha = 2s + n$ for some $n \in \mathbb{N} \cup \{0\}$. In the case $\alpha = s + n$, further, we have*

$$N_{s+n}^s(x) = \sum_{k=0}^{\infty} \frac{(2s)_k}{s-n+k}\frac{x^k}{k!} \tag{3.3.9}$$

where, for a given complex number z and a given non-negative integer k

$$(z)_k := \frac{\Gamma(z+k)}{\Gamma(z)} \tag{3.3.10}$$

denotes the Pochhamer symbol.

Proof. We first assume $s < \frac{1}{2}$ (for which the integrand in (3.3.6) is an element of $L^1(0,1)$) and $\alpha < 2s$ (to enable some of the following manipulations); the result for the full range of s and α will subsequently be established by analytic continuation in these variables. Writing

$$N_\alpha^s(x) = x^{-2s}\int_0^1 \operatorname{sgn}(x-y)\left|1-\frac{y}{x}\right|^{-2s} y^{\alpha-1}dy,$$

after a change of variables and some simple calculations for $x \in (0,1)$ we obtain

$$N_\alpha^s(x) = x^{-2s+\alpha}\left[\int_0^1 (1-r)^{-2s}r^{\alpha-1}dr - \int_1^{\frac{1}{x}} (r-1)^{-2s}r^{\alpha-1}dr\right]. \tag{3.3.11}$$

It then follows that

$$N_\alpha^s(x) = x^{-2s+\alpha}\left[\mathrm{B}(\alpha, 1-2s) - \mathrm{B}(1-2s, 2s-\alpha) + \mathrm{B}_x(-\alpha+2s, 1-2s)\right], \tag{3.3.12}$$

where

$$\begin{aligned} \mathrm{B}(a,b) &:= \int_0^1 t^{a-1}(1-t)^{b-1}dt = \frac{\Gamma(a)\Gamma(b)}{\Gamma(a+b)} \quad \text{and} \\ \mathrm{B}_x(a,b) &:= \int_0^x t^{a-1}(1-t)^{b-1}dt = x^a\sum_{k=0}^{\infty}\frac{(1-b)_k}{a+k}\frac{x^k}{k!} \end{aligned} \tag{3.3.13}$$

denote the Beta Function [2, eqns. 6.2.2] and the Incomplete Beta function [2, eqns. 6.6.8 and 15.1.1], respectively. Indeed, the first integral in (3.3.11) equals the first Beta function on the right-hand side of (3.3.12), and, after the change of variables $w = 1/r$, the second integral is easily seen to equal the difference $\mathrm{B}(1-2s, 2s-\alpha) - \mathrm{B}_x(-\alpha+2s, 1-2s)$.

In view of (3.3.12) and the right-hand expressions in equation (3.3.13) we can now write

$$N_\alpha^s(x) = x^{-2s+\alpha}\left[\frac{\Gamma(\alpha)\Gamma(1-2s)}{\Gamma(1+\alpha-2s)} - \frac{\Gamma(1-2s)\Gamma(-\alpha+2s)}{\Gamma(1-\alpha)}\right] + \sum_{k=0}^{\infty} \frac{(2s)_k}{2s-\alpha+k}\frac{x^k}{k!} \tag{3.3.14}$$

for all $x \in (0,1)$, $0 < s < \frac{1}{2}$ and $0 < \alpha < 2s$. Using Euler's reflection formula $\Gamma(z)\Gamma(1-z) = \pi\csc(\pi z)$ ([2, eq. 6.1.17]), and further trigonometric identities, equation (3.3.14) can also be made to read

$$N_\alpha^s(x) = x^{-2s+\alpha}\frac{\Gamma(\alpha)\Gamma(1-2s)}{\Gamma(1+\alpha-2s)}\frac{2\cos(\pi s)\sin(\pi(\alpha-s))}{\sin(\pi(\alpha-2s))} + \sum_{k=0}^{\infty} \frac{(2s)_k}{2s-\alpha+k}\frac{x^k}{k!}. \tag{3.3.15}$$

The required x-analyticity properties of the function $N_\alpha^s(x)$ will be established by resorting to analytic continuation of the function $N_\alpha^s(x)$ to complex values of the variables s and α. In view of the special role played by the quantity $q = \alpha - 2s$ in (3.3.15), further, it is useful to consider the function $M_q^s(x) = N_{q+2s}^s(x)$ where q is defined via the the change of variables $\alpha = q + 2s$. Then, collecting for each $n \in \mathbb{N}\cup\{0\}$ all the potentially singular terms in a neighborhood of $q = n$ and letting $G(s) := 2\Gamma(1-2s)\cos(\pi s)$ we obtain

$$\begin{aligned} M_q^s(x) &= N_{q+2s}^s(x) = \\ &= \left[x^q\frac{\Gamma(q+2s)G(s)\sin(\pi(q+s))}{\Gamma(1+q)\sin(\pi q)} + \frac{(2s)_n}{n-q}\frac{x^n}{n!}\right] + \sum_{k=0,\ k\neq n}^{\infty}\frac{(2s)_k}{k-q}\frac{x^k}{k!}. \end{aligned} \tag{3.3.16}$$

In order to obtain expressions for $N_\alpha^s(x)$ which manifestly display its analytic character with respect to x for all required values of s and α, we analytically continue the function M_q^s to all complex values of q and s for which the corresponding (s,α) point belongs to the domain $D = \{(s,\alpha) : \Re s < 1\} \times \{\Re\alpha > 0\} \subset \mathbb{C}^2$. To do this we consider the following facts:

1. Since $\Gamma(z)$ is a never-vanishing function of z whose only singularities are simple poles at the nonpositive integers $z = -n$ ($n \in \mathbb{N}\cup\{0\}$), and since, as a consequence, $1/\Gamma(z)$ is an entire function of z which only vanishes at non-positive integer values of z, the quotient $\Gamma(\alpha)/\Gamma(1+\alpha-2s)$ is analytic and non-zero for $(s,\alpha) \in D$.

2. The function $G(s)$ that appears on the right hand side of (3.3.16) ($s \neq 1/2$) can be continued analytically to the domain $\Re s < 1$ with the value $G(1/2) = \pi$. Further, this function does not vanish for any s with $0 < \Re s < 1$.

3. For fixed $s \in \mathbb{C}$ the quotient $\sin(\pi(\alpha-s))/\sin(\pi(\alpha-2s)) = \sin(\pi(q+s))/\sin(\pi q)$ is a meromorphic function of q—whose singularities are simple poles at the integer values $q = n \in \mathbb{Z}$ with corresponding residues given by $(-1)^n\sin(\pi(q+s))/\pi$. Further, for $s \notin \mathbb{Z}$ the quotient vanishes if and only if $q = n - s$ (or equivalently, $\alpha = s + n$) for some $n \in \mathbb{Z}$.

4. For each x in the unit disc $\{x \in \mathbb{C} : |x| < 1\}$ the infinite series on the right-hand side of (3.3.15) converges uniformly over compact subsets of $D \setminus \{\alpha = 2s + n, n \in \mathbb{N} \cup \{0\}\}$. This is easily checked by using the asymptotic relation [2, 6.1.46] $\lim_{k\to\infty} k^{1-2s}(2s)_k/k! = 1/\Gamma(2s)$, and taking into account that the functions $s \to (2s)_k$ and $s \to 1/\Gamma(2s)$ are entire and, thus, finite-valued for each $s \in \mathbb{C}$ and each $k \in \mathbb{N} \cup \{0\}$.

5. For each fixed $s \in \mathbb{C}$ and each $x \in \mathbb{C}$ with $|x| < 1$ the series on the right hand side of (3.3.15) is a meromorphic function of q containing only simple polar singularities at $q = n \in \mathbb{N} \cup \{0\}$, with corresponding residues given by $(2s)_n x^n/n!$. Indeed, point (4) above tells us that the series is an analytic function of q for $q \notin \mathbb{N} \cup \{0\}$; the residue at the non-negative integer values of q can be computed immediately by considering a single term of the series.

6. The residue of the two terms under brackets on the right-hand side of (3.3.16) are negatives of each other. This can be established easily by considering points (3) and (5) as well as the identity $\lim_{q\to n}(-1)^n G(s)\sin(\pi(q + s))/\pi = 1/\Gamma(2s)$—which itself results from Euler's reflection formula and standard trigonometric identities.

7. The sum of the bracketed terms in (3.3.16) is an analytic function of q up to and including non-negative integer values of this variable, as it follows from point (6). Its limit as $q \to n$, further, is easily seen to equal the product of an analytic function of q and s times the monomial x^n.

Expressions establishing the x-analyticity properties of $N^s_\alpha(x)$ can now be obtained. On one hand, by Lemma 3.3.6 the function $N^s_\alpha(x)$ is a jointly analytic function of (s, α) in the domain D. In view of points (3) through (7), on the other hand, we see that the right-hand side expression in equation (3.3.15) is also an analytic function throughout D. Since, as shown above in this proof, these two functions coincide in the open set $U := (0, \frac{1}{2}) \times (0, 2s) \subset D$, it follows that they must coincide throughout D. In other words, interpreting the right-hand sides in equations (3.3.15) and (3.3.16) as their analytic continuation at all removable-singularity points (cf. points (2) and (6)) these two equations hold throughout D.

We may now establish the x-analyticity of the function $N^s_\alpha(x)$ for given α and s in D. We first do this in the case $\alpha = s + n$ with $n \in \mathbb{N} \cup \{0\}$ and $s \in (0, 1)$. Under these conditions the complete first term in (3.3.15) vanishes—even at $s = 1/2$—as it follows from points (1) through (3). The function $N^s_\alpha(x)$ then equals the series on the right-hand side of (3.3.15). In view of point (4) we thus see that, at least in the case $\alpha = s + n$, $N^s_\alpha(x)$ is analytic with respect to x for $|x| < 1$ and, further, that the desired relation (3.3.9) holds.

In order to establish the x-analyticity of $N^s_\alpha(x)$ in the case $\alpha = 2s + n$ (or, equivalently, $q = n$) with $n \in \mathbb{N} \cup \{0\}$ and $s \in (0, 1)$, in turn, we consider the limit $q \to n$ of the right-hand side in equation (3.3.16). Evaluating this limit by means of points (4) and (7) results in an expression which, in view of point (4), exhibits the x-analyticity of the function N^s_α for $|x| < 1$ in the case under consideration.

To complete our description of the analytic character of $N^s_\alpha(x)$ for $(\alpha, s) \in D$ it remains to show that this function is not x-analytic near zero whenever $(\alpha - s)$ and $(\alpha - 2s)$ are not elements of

$\mathbb{N} \cup \{0\}$. But this follows directly by consideration of (3.3.15)—since, per points (1), (2) and (3), for such values of α and s the coefficient multiplying the non-analytic term $x^{-2s+\alpha}$ in (3.3.15) does not vanish. The proof is now complete. □

3.3.2 Singularities on both edges

Utilizing Theorem 3.3.7, which in particular establishes that the image of the function $u_\alpha(y) = y^\alpha$ (equation (3.3.5)) under the operator T_s is analytic for $\alpha = s + n$, here we consider the image of the function

$$u(y) := y^s(1-y)^s y^n \tag{3.3.17}$$

under the operator T_s and we show that, in fact, $T_s[u]$ is a polynomial of degree n. This is a desirable result which, as we shall see, leads in particular to (i) Diagonalization of weighted version of the fractional Laplacian operator, as well as (ii) Smoothness and even analyticity (up to a singular multiplicative weight) of solutions of equation (3.1.1) under suitable hypothesis on the right-hand side f.

Remark 3.3.8. *Theorem 3.3.7 states that the image of the aforementioned function u_α under the operator T_s is analytic not only for $\alpha = s + n$ but also for $\alpha = 2s + n$. But, as shown in Remark 3.5.20, the smoothness and analyticity theory mentioned in point (ii) above, which applies in the case $\alpha = s + n$, cannot be duplicated in the case $\alpha = 2s + n$. Thus, except in Remark 3.5.20, the case $\alpha = 2s + n$ will not be further considered in this Chapter.*

In view of Remark 3.3.2 and in order to obtain an explicit expression for $T_s[u]$ we first express the derivative of u in the form

$$u'(y) = \frac{d}{dy}\left(y^s(1-y)^s y^n\right) = y^{s-1}(1-y)^{s-1}\left[y^n(s+n-(2s+n)y)\right]$$

and (using (3.2.3)) we thus obtain

$$T_s[u] = (1-2s)C_s\left((s+n)L_n^s - (2s+n)L_{n+1}^s\right). \tag{3.3.18}$$

where

$$L_n^s := P.V.\int_0^1 \operatorname{sgn}(x-y)|x-y|^{-2s} y^{s-1}(1-y)^{s-1} y^n dy \tag{3.3.19}$$

On the other hand, in view of definitions (3.3.1) and (3.3.2) and Lemma 3.2.4 it is easy to check that

$$\frac{\partial}{\partial x} S_s(y^{s-1}(1-y)^{s-1}y^n) = (1-2s)C_s L_n^s. \tag{3.3.20}$$

In order to characterize the image $T_s[u]$ of the function u in (3.3.17) under the operator T_s, Lemma 3.3.9 below presents an explicit expression for the closely related function L_n^s. In particular the lemma shows that L_n^s is a polynomial of degree $n-1$, which implies that $T_s[u]$ is a polynomial of degree n.

Lemma 3.3.9. *$L_n^s(x)$ is a polynomial of degree $n-1$. More precisely,*

$$L_n^s(x) = \Gamma(s) \sum_{k=0}^{n-1} \frac{(2s)_k}{k!} \frac{\Gamma(n-k-s+1)}{(s+k-n)\Gamma(n-k)} x^k. \tag{3.3.21}$$

Proof. We proceed by substituting $(1-y)^{s-1}$ in the integrand (3.3.19) by its Taylor expansion around $y=0$,

$$(1-y)^{s-1} = \sum_{j=0}^{\infty} q_j y^j, \text{ with } q_j = \frac{(1-s)_j}{j!}, \tag{3.3.22}$$

and subsequently exchanging the principal value integration with the infinite sum (a step that is justified in Appendix 3.8.2). The result is

$$L_n^s(x) = \sum_{j=0}^{\infty} \left(\text{P.V.} \int_0^1 \text{sgn}(x-y)|x-y|^{-2s} q_j y^{s-1+n+j} dy \right) \tag{3.3.23}$$

or, in terms of the functions N_α^s defined in equation (3.3.6),

$$L_n^s(x) = \sum_{j=0}^{\infty} q_j N_{s+n+j}^s. \tag{3.3.24}$$

In view of (3.3.9), equation (3.3.24) can also be made to read

$$L_n^s(x) = \sum_{j=0}^{\infty} \sum_{k=0}^{\infty} \frac{(1-s)_j}{j!} \frac{(2s)_k}{k!} \frac{1}{s-n-j+k} x^k, \tag{3.3.25}$$

or, interchanging of the order of summation in this expression (which is justified in Appendix 3.8.3),

$$L_n^s(x) = \sum_{k=0}^{\infty} \frac{(2s)_k}{k!} a_k^n x^k, \text{ where } a_k^n = \sum_{j=0}^{\infty} \frac{(1-s)_j}{j!} \frac{1}{s-n-j+k}. \tag{3.3.26}$$

The proof will be completed by evaluating explicitly the coefficients a_k^n for all pairs of integers k and n.

In order to evaluate a_k^n we consider the Hypergeometric function

$${}_2F_1(a,b;c;z) = \sum_{j=0}^{\infty} \frac{(a)_j (b)_j}{(c)_j} \frac{z^j}{j!}. \tag{3.3.27}$$

Comparing the a_k^n expression in (3.3.26) to (3.3.27) and taking into account the relation

$$\frac{1}{s-n-j+k} = \frac{(n-k-s)_j}{(n-k-s+1)_j} \frac{1}{s+k-n}$$

(which follows easily from the recursion $(z+1)_j = (z)_j (z+j)/z$ for the Pochhamer symbol defined in equation (3.3.10)), we see that a_k^n can be expressed in terms of the Hypergeometric function ${}_2F_1$ evaluated at $z=1$:

$$a_k^n = 2F_1(1-s, n-k-s; n-k-s+1; 1)/(s+k-n).$$

This expression can be simplified further: in view of Gauss' formula ${}_2F_1(a,b;c;1) = \frac{\Gamma(c)\Gamma(c-a-b)}{\Gamma(c-a)\Gamma(c-b)}$ (see e.g. [9, p. 2]) we obtain the concise expression

$$a_k^n = \frac{\Gamma(n-k-s+1)\Gamma(s)}{(s+k-n)\Gamma(n-k)}. \tag{3.3.28}$$

It then clearly follows that $a_k^n = 0$ for $k \geq n$—since the term $\Gamma(n-k)$ in the denominator of this expression is infinite for all integers $k \geq n$. The series in (3.3.26) is therefore a finite sum up to $k = n-1$ which, in view of (3.3.28), coincides with the desired expression (3.3.21). The proof is now complete. □

Corollary 3.3.10. *Let $w(y) = u(y)\chi_{(0,1)}(y)$ where $u = y^s(1-y)^s y^n$ (equation (3.3.17)) and where $\chi_{(0,1)}$ denotes the characteristic function of the interval $(0,1)$. Then, defining the n-th degree polynomial $p(x) = (1-2s)C_s\left((s+n)L_n^s - (2s+n)L_{n+1}^s\right)$ with L_n^s given by (3.3.21), for all $x \in \mathbb{R}$ such that $x \neq 0$ and $x \neq 1$ (cf. Remark 3.2.6) we have*

$$T_s[u](x) = p(x) \tag{3.3.29}$$

and, consequently,

$$(-\Delta)^s w(x) = p(x). \tag{3.3.30}$$

Proof. In view of equation (3.3.18) and Lemma 3.3.9 we obtain (3.3.29). The relation (3.3.30) then follows from Remark 3.3.3. □

3.4 Diagonal Form of the Weighted Fractional Laplacian

In view of equation 3.3.20 and Lemma 3.3.9, the results obtained for the image of $u(y) = y^s(1-y)^s y^n$ under the operator T_s can be easily adapted to obtain analogous polynomial expressions of degree exactly n for the image of the function $\tilde{u}(y) = y^{s-1}(1-y)^{s-1}y^n$ under the operator S_s. And, indeed, both of these results can be expressed in terms of isomorphisms in the space $\mathbb{P}_n$ of polynomials of degree less or equal than n, as indicated in the following corollary,

Corollary 3.4.1. *Let $s \in (0,1)$, $m \in \mathbb{N}$, and consider the linear mappings $P : \mathbb{P}_m \to \mathbb{P}_m$ and $Q : \mathbb{P}_m \to \mathbb{P}_m$ defined by*

$$\begin{aligned} P &: p \to T_s[y^s(1-y)^s p(y)] \quad \text{and} \\ Q &: p \to S_s[y^{s-1}(1-y)^{s-1}p(y)]. \end{aligned} \tag{3.4.1}$$

Then the matrices $[P]$ and $[Q]$ of the linear mappings P and Q in the basis $\{y^n : n = 0, \ldots, m\}$ are upper-triangular and their diagonal entries are given by

$$\begin{aligned} P_{nn} &= \frac{\Gamma(2s+n+1)}{n!} \quad \text{and} \\ Q_{nn} &= -\frac{\Gamma(2s+n-1)}{n!}, \end{aligned}$$

respectively. In particular, for $s = \frac{1}{2}$ *we have*

$$\begin{aligned} P_{nn} &= 2n \\ Q_{nn} &= -\frac{2}{n} \quad \textit{for} \quad n \neq 0 \quad \textit{and} \quad Q_{00} = -2\log(2). \end{aligned} \tag{3.4.2}$$

Proof. The expressions for $n \neq 0$ and for P_{00} follow directly from equations (3.3.18), (3.3.20) and (3.3.21). In order to obtain Q_{00}, in turn, we note from (3.3.20) that for $n = 0$ we have $\frac{\partial}{\partial x} S_s(y^{s-1}(1-y)^{s-1}y^n) = 0$. In particular, $S_s(y^{s-1}(1-y)^{s-1})$ does not depend on x and we therefore obtain

$$\begin{aligned} Q_{00} = S_s(y^{s-1}(1-y)^{s-1}) &= C_s \int_0^1 (y^{2s-1} - 1) y^{s-1}(1-y)^{s-1} dy \\ &= C_s \left(\mathrm{B}(3s-1, s) - \mathrm{B}(s,s) \right). \end{aligned}$$

In the limit as $s \to 1/2$, employing l'Hôpital's rule together with well known values[2, 6.1.8, 6.3.2, 6.3.3] for the Gamma function and it's derivative at $z = 1/2$ and $z = 1$, we obtain $S_{\frac{1}{2}}(y^{-1/2}(1-y)^{-1/2}) = -2\log(2)$ □

In view of the form of the mapping P in equation (3.4.1) and using the "weight function"

$$\omega^s(y) = (y-a)^s (b-y)^s,$$

for $\phi \in C^2(a,b) \cap C^1[a,b]$ (that is, ϕ smooth up to the boundary but it does not necessarily vanish on the boundary) we introduce the weighted version

$$K_s(\phi) = C_s \frac{d}{dx} \int_a^b |x-y|^{1-2s} \frac{d}{dy} \left(\omega^s \phi(y) \right) dy \quad (s \neq 1/2), \tag{3.4.3}$$

of the operator T_s in equation (3.3.3). In view of Lemma 3.2.3, K_s can also be viewed as a weighted version of the Fractional Laplacian operator, and we therefore define

$$(-\Delta)^s_\omega[\phi] = K_s(\phi) \ \text{ for } \ \phi \in C^2(a,b) \cap C^1[a,b]. \tag{3.4.4}$$

Remark 3.4.2. *Clearly, given a solution* ϕ *of the equation*

$$(-\Delta)^s_\omega[\phi] = f \tag{3.4.5}$$

in the domain $\Omega = (a,b)$*, the function* $u = \omega^s \phi$ *extended by zero outside* (a,b) *solves the Dirichlet problem for the Fractional Laplacian* (3.1.1) *(cf. Lemma 3.2.3).*

In order to study the spectral properties of the operator $(-\Delta)^s_\omega$, consider the weighted L^2 space

$$L^2_s(a,b) = \left\{ \phi : (a,b) \to \mathbb{R} \, : \, \int_a^b |\phi|^2 \omega^s < \infty \right\}, \tag{3.4.6}$$

which, together with the inner product

$$(\phi, \psi)^s_{a,b} = \int_a^b \phi \, \psi \, \omega^s \tag{3.4.7}$$

and associated norm is a Hilbert space. We can now establish the following lemma.

Lemma 3.4.3. *The operator $(-\Delta)^s_\omega$ maps $\mathbb{P}_n$ into itself. The restriction of $(-\Delta)^s_\omega$ to $\mathbb{P}_n$ is a self adjoint operator with respect to the inner product $(\cdot,\cdot)^s_{a,b}$.*

Proof. Using the notation $K_s = (-\Delta)^s_\omega$, we first establish the relation $(K_s[p], q) = (p, K_s[q])$ for $p, q \in \mathbb{P}_n$. But this follows directly from application of integration by parts and Fubini's theorem followed by an additional instance of integration by parts in (3.4.3), and noting that the the boundary terms vanish by virtue of the weight ω^s. □

The orthogonal polynomials with respect to the inner product under consideration are the well known Gegenbauer polynomials [2]. These are defined on the interval $(-1, 1)$ by the recurrence

$$\begin{aligned} C_0^{(\alpha)}(x) &= 1, \\ C_1^{(\alpha)}(x) &= 2\alpha x, \\ C_n^{(\alpha)}(x) &= \frac{1}{n}\left[2x(n+\alpha-1)C_{n-1}^{(\alpha)}(x) - (n+2\alpha-2)C_{n-2}^{(\alpha)}(x)\right]; \end{aligned} \tag{3.4.8}$$

for an arbitrary interval (a, b), the corresponding orthogonal polynomials can be easily obtained by means of a suitable affine change of variables. Using this orthogonal basis we can now produce an explicit diagonalization of the operator $(-\Delta)^s_\omega$. We first consider the interval $(0, 1)$; the corresponding result for a general interval (a, b) is presented in Corollary 3.4.5.

Theorem 3.4.4. *Given $s \in (0, 1)$ and $n \in \mathbb{N} \cup \{0\}$, consider the Gegenbauer polynomial $C_n^{(s+1/2)}$, and let $p_n(x) = C_n^{(s+1/2)}(2x - 1)$. Then the weighted operator $(-\Delta)^s_\omega$ in the interval $(0, 1)$ satisfies the identity*

$$(-\Delta)^s_\omega(p_n) = \frac{\Gamma(2s+n+1)}{n!}\, p_n. \tag{3.4.9}$$

Proof. By Lemma 3.4.3 the restriction of the operator $(-\Delta)^s_\omega$ to the subspace $\mathbb{P}_m$ is self-adjoint and thus diagonalizable. We may therefore select polynomials $q_0, q_1, \ldots, q_m \in \mathbb{P}_m$ (where, for $0 \le n \le m$, q_n is a polynomial eigenfunction of $(-\Delta)^s_\omega$ of degree exactly n) which form an orthogonal basis of the space $\mathbb{P}_m$. Clearly, the eigenfunctions q_n are orthogonal and, therefore, up to constant factors, the polynomials q_n must coincide with p_n for all n, $0 \le n \le m$. The corresponding eigenvalues can be extracted from the diagonal elements, displayed in equation (3.4.2), of the upper-triangular matrix $[P]$ considered in Corollary 3.4.1. These entries coincide with the constant term in (3.4.9), and the proof is thus complete. □

Corollary 3.4.5. *The weighted operator $(-\Delta)^s_\omega$ in the interval $(-1, 1)$ satisfies the identity*

$$(-\Delta)^s_\omega(C_n^{(s+1/2)}) = \lambda_n^s\, C_n^{(s+1/2)},$$

where

$$\lambda_n^s = \frac{\Gamma(2s+n+1)}{n!}. \tag{3.4.10}$$

Moreover in the interval (a, b), we have

$$(-\Delta)^s_\omega(p_n) = \lambda_n^s\, p_n, \tag{3.4.11}$$

where $p_n(x) = C_n^{(s+1/2)}\left(\frac{2(x-a)}{b-a} - 1\right)$.

Proof. The formula is obtained by employing the change of variables $\tilde{x} = (x-a)/(b-a)$ and $\tilde{y} = (y-a)/(b-a)$ in equation (3.4.3) to map the weighted operator in (a,b) to the corresponding operator in $(0,1)$, and observing that $\omega^s(y) = (b-a)^{2s}\tilde{\omega}^s(\tilde{y})$, where $\tilde{\omega}^s(\tilde{y}) = \tilde{y}^s(1-\tilde{y})^s$. □

Remark 3.4.6. *It is useful to note that, in view of the formula* $\lim_{n\to\infty} n^{\beta-\alpha}\Gamma(n+\alpha)/\Gamma(n+\beta) = 1$ *(see e.g. [2, 6.1.46]) we have the asymptotic relation* $\lambda_n^s \approx O\left(n^{2s}\right)$ *for the eigenvalues* (3.4.10)*. This fact will be exploited in the following sections in order to obtain sharp Sobolev regularity results as well as regularity results in spaces of analytic functions.*

As indicated in the following corollary, the background developed in the present section can additionally be used to obtain the diagonal form of the operator S_s for all $s \in (0,1)$. This corollary generalizes a corresponding existing result for the case $s = 1/2$—for which, as indicated in Remark 3.3.4, the operator S_s coincides with the single-layer potential for the solution of the two-dimensional Laplace equation outside a straight arc or "crack".

Corollary 3.4.7. *The weighted operator* $\phi \to S_s[\omega^{s-1}\phi]$ *can be diagonalized in terms of the Gegenbauer polynomials* $C_n^{(s-1/2)}$

$$S_s\left[\omega^{s-1}C_n^{(s-1/2)}\right] = \mu_n^s C_n^{(s-1/2)},$$

where in this case the eigenvalues are given by

$$\mu_n^s = -\frac{\Gamma(2s+n-1)}{n!}.$$

Proof. The proof for the interval $[0,1]$ is analogous to that of Theorem 3.4.4. In this case, the eigenvalues are extracted from the diagonal entries of the upper triangular matrix $[Q]$ in equation (3.4.2). A linear change of variables allows to obtain the desired formula for an arbitrary interval. □

Corollary 3.4.8. *In the particular case* $s = 1/2$ *on the interval* $(-1,1)$*, the previous results amount, on one hand, to the known result [54, eq. 9.27] (cf also [83]),*

$$\int_{-1}^{1} \log|x-y| T_n(y)(1-y^2)^{-1/2} dy = \begin{cases} -\frac{\pi}{n}T_n & \text{for } n \neq 0 \\ -2\log(2) & \text{for } n = 0 \end{cases}$$

(where T_n *denotes the Tchevyshev polynomial of the first kind), and, on the other hand, to the relation*

$$\frac{\partial}{\partial x}\int_{-1}^{1} \log|x-y| \frac{\partial}{\partial y}\left(U_n(y)(1-y^2)^{1/2}\right) dy = (n+1)\pi U_n$$

(where U_n *denotes the Tchevyshev polynomial of the second kind).*

3.5 Regularity Theory

This section studies the regularity of solutions of the fractional Laplacian equation (3.1.1) under various smoothness assumptions on the right-hand side f–including treatments in both Sobolev and analytic function spaces, and for multi-interval domains Ω as in Definition 3.2.1. In particular,

Section 3.5.1 introduces certain weighted Sobolev spaces $H^r_s(\Omega)$ (which are defined by means of expansions in Gegenbauer polynomials together with an associated norm). The space A_ρ of analytic functions in a certain "Bernstein Ellipse" $\mathcal{B}_\rho$ is then considered in Section 3.5.2. The main result in Section 3.5.1 (resp. Section 3.5.2) establishes that for right-hand sides f in the space $H^r_s(\Omega)$ with $r \geq 0$ (resp. the space $A_\rho(\Omega)$ with $\rho > 0$) the solution u of equation (3.1.1) can be expressed in the form $u(x) = \omega^s(x)\phi(x)$, where ϕ belongs to $H^{r+2s}_s(\Omega)$ (resp. to $A_\rho(\Omega)$). Sections 3.5.1 and 3.5.2 consider the single-interval case; generalizations of all results to the multi-interval context are presented in Section 3.5.3. The theoretical background developed in the present Section 3.5 is exploited in Section 3.6 to develop and analyze a class of effective algorithms for the numerical solution of equation (3.1.1) in multi-interval domains Ω.

3.5.1 Sobolev Regularity, single interval case

In this section we define certain weighted Sobolev spaces, which provide a sharp regularity result for the weighted Fractional Laplacian $(-\Delta)^s_\omega$ (Theorem 3.5.12) as well as a natural framework for the analysis of the high order numerical methods proposed in Section 3.6. It is noted that these spaces coincide with the non-uniformly weighted Sobolev spaces introduced in [8]; Theorem 3.5.14 below provides an embedding of these spaces into spaces of continuously differentiable functions. For notational convenience, in the present discussion leading to the definition 3.5.6 of the Sobolev space $H^r_s(\Omega)$, we restrict our attention to the domain $\Omega = (-1, 1)$; the corresponding definition for general multi-interval domains then follows easily.

In order to introduce the weighted Sobolev spaces we note that the set of Gegenbauer polynomials $C_n^{(s+1/2)}$ constitutes an orthogonal basis of $L^2_s(-1, 1)$ (cf. (3.4.6)). The L^2_s norm of a Gegenbauer polynomial (see [2, eq 22.2.3]), is given by

$$h_j^{(s+1/2)} = \left\| C_j^{(s+1/2)} \right\|_{L^2_s(-1,1)} = \sqrt{\frac{2^{-2s}\pi}{\Gamma^2(s+1/2)} \frac{\Gamma(j+2s+1)}{\Gamma(j+1)(j+s+1/2)}}. \tag{3.5.1}$$

Definition 3.5.1. *Throughout this Chapter $\tilde{C}_j^{(s+1/2)}$ denotes the normalized polynomial $C_j^{(s+1/2)}/h_j^{(s+1/2)}$.*

Given a function $v \in L^2_s(-1, 1)$, we have the following expansion

$$v(x) = \sum_{j=0}^{\infty} v_{j,s} \tilde{C}_j^{(s+1/2)}(x), \tag{3.5.2}$$

which converges in $L^2_s(-1, 1)$, and where

$$v_{j,s} = \int_{-1}^{1} v(x) \tilde{C}_j^{(s+1/2)}(x)(1 - x^2)^s dx. \tag{3.5.3}$$

In view of the expression

$$\frac{d}{dx} C_j^{(\alpha)}(x) = 2\alpha C_{j-1}^{(\alpha+1)}(x), \ j \geq 1, \tag{3.5.4}$$

for the derivative of a Gegenbauer polynomial (see e.g. [76, eq. 4.7.14]), we have

$$\frac{d}{dx}\tilde{C}_j^{(s+1/2)}(x) = (2s+1)\frac{h_{j-1}^{(s+3/2)}}{h_j^{(s+1/2)}}\tilde{C}_{j-1}^{s+3/2}. \tag{3.5.5}$$

Thus, using term-wise differentiation in (3.5.2) we may conjecture that, for sufficiently smooth functions v, we have

$$v^{(k)}(x) = \sum_{j=k}^{\infty} v_{j-k,s+k}^{(k)} \tilde{C}_{j-k}^{(s+k+1/2)}(x) \tag{3.5.6}$$

where $v^{(k)}(x)$ denotes the k-th derivative of the function $v(x)$ and where, calling

$$A_j^k = \prod_{r=0}^{k-1} \frac{h_{j-1-r}^{(s+3/2+r)}}{h_{j-r}^{(s+1/2+r)}}(2(s+r)+1) = 2^k \frac{h_{j-k}^{(s+1/2+k)}}{h_j^{(s+1/2)}} \frac{\Gamma(s+1/2+k)}{\Gamma(s+1/2)}, \tag{3.5.7}$$

the coefficients in (3.5.6) are given by

$$v_{j-k,s+k}^{(k)} = A_j^k \, v_{j,s}. \tag{3.5.8}$$

Lemma 3.5.2 below provides, in particular, a rigorous proof of (3.5.6) under minimal hypothesis. Further, the integration by parts formula established in that lemma together with the asymptotic estimates on the factors B_j^k provided in Lemma 3.5.3, then allow us to relate the smoothness of a function v and the decay of its Gegenbauer coefficients; see Corolary 3.5.4.

Lemma 3.5.2 (Integration by parts)**.** *Let $k \in \mathbb{N}$ and let $v \in C^{k-2}[-1,1]$ such that for a certain decomposition $[-1,1] = \bigcup_{i=1}^{n}[\alpha_i, \alpha_{i+1}]$ $(-1 = \alpha_1 < \alpha_i < \alpha_{i+1} < \alpha_n = 1)$ and for certain functions $\tilde{v}_i \in C^k[\alpha_i, \alpha_{i+1}]$ we have $v(x) = \tilde{v}_i(x)$ for all $x \in (\alpha_i, \alpha_{i+1})$ and $1 \le i \le n$. Then for $j \ge k$ the s-weighted Gegenbauer coefficients $v_{j,s}$ defined in equation* (3.5.3) *satisfy*

$$\begin{aligned} v_{j,s} = B_j^k \int_{-1}^{1} \tilde{v}^{(k)}(x)\tilde{C}_{j-k}^{(s+k+1/2)}(x)(1-x^2)^{s+k}dx \\ - B_j^k \sum_{i=1}^{n} \left[\tilde{v}^{(k-1)}(x)\tilde{C}_{j-k}^{(s+k+1/2)}(x)(1-x^2)^{s+k}\right]_{\alpha_i}^{\alpha_{i+1}}, \end{aligned} \tag{3.5.9}$$

where

$$B_j^k = \frac{h_{j-k}^{(s+k+1/2)}}{h_j^{(s+1/2)}} \prod_{r=0}^{k-1} \frac{(2(s+r)+1)}{(j-r)(2s+r+j+1)}. \tag{3.5.10}$$

With reference to equation (3.5.7)*, further, we have $A_j^k = \frac{1}{B_j^k}$. In particular, under the additional assumption that $v \in C^{k-1}[-1,1]$ the relation* (3.5.8) *holds.*

Proof. Equation (3.5.9) results from iterated applications of integration by parts together with the relation [2, eq. 22.13.2]

$$\frac{\ell(2t+\ell+1)}{2t+1}\int (1-y^2)^t C_\ell^{(t+1/2)}(y)dy = -(1-x^2)^{t+1}C_{\ell-1}^{(t+3/2)}(x).$$

and subsequent normalization according to Definition 3.5.1. The validity of the relation $A_j^k = \frac{1}{B_j^k}$ can be checked easily. □

Lemma 3.5.3. *There exist constants C_1 and C_2 such that the factors B_j^k in equation* (3.5.7) *satisfy*

$$C_1 j^{-k} < |B_j^k| < C_2 j^{-k}$$

Proof. In view of the relation $\lim_{j\to\infty} j^{b-a}\Gamma(j+a)/\Gamma(j+b) = 1$ (see [2, 6.1.46]) it follows that $h_j^{(s+1/2)}$ in equation (3.5.1) satisfies

$$\lim_{j\to\infty} j^{1/2-s} h_j^{(s+1/2)} \neq 0 \tag{3.5.11}$$

and, thus, letting

$$q_j^k = \frac{h_{j-k}^{(s+k+1/2)}}{h_j^{(s+1/2)}}, \tag{3.5.12}$$

we obtain

$$\lim_{j\to\infty} q_j^k / j^k \neq 0. \tag{3.5.13}$$

The lemma now follows by estimating the asymptotics of the product term on the right-hand side of (3.5.10) as $j \to \infty$. □

Corollary 3.5.4. *Let $k \in \mathbb{N}$ and let v satisfy the hypothesis of Lemma 3.5.2. Then the Gegenbauer coefficients $v_{j,s}$ in equation* (3.5.3) *are quantities of order $O(j^{-k})$ as $j \to \infty$:*

$$|v_{j,s}| < C j^{-k}$$

for a constant C that depends on v and k.

Proof. The proof of the corollary proceeds by noting that the factor B_j^k in equation (3.5.9) is a quantity of order j^{-k} (Lemma 3.5.3), and obtaining bounds for the remaining factors in that equation. These bounds can be produced by (i) applying the Cauchy-Schwartz inequality in the space $L^2_{s+k}(-1,1)$ to the $(s+k)$-weighted scalar product (3.4.7) that occurs in equation (3.5.9); and (ii) using [76, eq. 7.33.6] to estimate the boundary terms in equation (3.5.9). The derivation of the bound per point (i) is straightforward. From [76, eq. 7.33.6], on the other hand, it follows directly that for each $\lambda > 0$ there is a constant C such that

$$|\sin(\theta)^{2\lambda-1} C_j^\lambda(\cos(\theta))| \leq C j^{\lambda-1}.$$

Letting $x = \cos(\theta)$, $\lambda = s + k + 1/2$ and dividing by the normalization constant $h_j^{(s+k+1/2)}$ we then obtain

$$\left|\tilde{C}_j^{s+k+1/2}(x)(1-x^2)^{s+k}\right| < C j^{s+k-1/2} / h_j^{(s+k+1/2)}.$$

In view of (3.5.11), the right hand side in this equation is bounded for all $j \geq 0$. The proof now follows from Lemma 3.5.3. □

We now define a class of Sobolev spaces H_s^r that, as shown in Theorem 3.5.12, completely characterizes the Sobolev regularity of the weighted fractional Laplacian operator $(-\Delta)_\omega^s$.

Remark 3.5.5. *In what follows, and when clear from the context, we drop the subindex s in the notation for Gegenbauer coefficients such as $v_{j,s}$ in* (3.5.3)*, and we write e.g. $v_j = v_{j,s}$, $w_j = w_{j,s}$, $f_j = f_{j,s}$, etc.*

Definition 3.5.6. *Let $r, s \in \mathbb{R}$, $r \geq 0$, $s > -1/2$ and, for $v \in L^2_s(-1,1)$ call v_j the corresponding Gegenbauer coefficient* (3.5.3) *(see Remark 3.5.5). Then the complex vector space $H^r_s(-1,1) = \left\{ v \in L^2_s(-1,1) \colon \sum_{j=0}^{\infty} (1+j^2)^r |v_j|^2 < \infty \right\}$ will be called the s-weighted Sobolev space of order r.*

Lemma 3.5.7. *Let $r, s \in \mathbb{R}$, $r \geq 0$, $s > -1/2$. Then the space $H^r_s(-1,1)$ endowed with the inner product $\langle v, w \rangle^r_s = \sum_{j=0}^{\infty} v_j w_j (1+j^2)^r$ and associated norm*

$$\|v\|_{H^r_s} = \sum_{j=0}^{\infty} |v_j|^2 (1+j^2)^r \tag{3.5.14}$$

is a Hilbert space.

Proof. The proof is completely analogous to that of [46, Theorem 8.2]. □

Remark 3.5.8. *By definition it is immediately checked that for every function $v \in H^r_s(-1,1)$ the Gegenbauer expansion* (3.5.2) *with expansion coefficients* (3.5.3) *is convergent in $H^r_s(-1,1)$.*

Remark 3.5.9. *In view of the Parseval identity $\|v\|^2_{L^2_s(-1,1)} = \sum_{n=0}^{\infty} |v_n|^2$ it follows that the Hilbert spaces $H^0_s(-1,1)$ and $L^2_s(-1,1)$ coincide. Further, we have the dense compact embedding $H^t_s(-1,1) \subset H^r_s(-1,1)$ whenever $r < t$. (The density of the embedding follows directly from Remark 3.5.8 since all polynomials are contained in $H^r_s(-1,1)$ for every r.) Finally, by proceeding as in [46, Theorem 8.13] it follows that for any $r > 0$, $H^r_s(-1,1)$ constitutes an interpolation space between $H^{\lfloor r \rfloor}_s(-1,1)$ and $H^{\lceil r \rceil}_s(-1,1)$ in the sense defined by [12, Chapter 2].*

Closely related "Jacobi-weighted Sobolev spaces" $\mathcal{H}^k_s$ (Definition 3.5.10) were introduced previously [8] in connection with Jacobi approximation problems in the p-version of the finite element method. As shown in Lemma 3.5.11 below, in fact, the spaces $\mathcal{H}^k_s$ coincide with the spaces H^k_s defined above, and the respective norms are equivalent.

Definition 3.5.10 (Babuška and Guo [8])**.** *Let $k \in \mathbb{N} \cup \{0\}$ and $r > 0$. The k-th order non-uniformly weighted Sobolev space $\mathcal{H}^k_s(a,b)$ is defined as the completion of the set $C^\infty(a,b)$ under the norm*

$$\|v\|_{\mathcal{H}^k_s} = \left(\sum_{j=0}^{k} \int_a^b |v^{(j)}(x)|^2 \omega^{s+j} dx \right)^{1/2} = \left(\sum_{j=0}^{k} \|v^{(j)}\|^2_{L^2_{s+j}} \right)^{1/2}.$$

The r-th order space $\mathcal{H}^r_s(a,b)$, in turn, is defined by interpolation of the spaces $\mathcal{H}^k_s(a,b)$ ($k \in \mathbb{N} \cup \{0\}$) by the K-method (see [12, Section 3.1]).

Lemma 3.5.11. *Let $r > 0$. The spaces $H^r_s(a,b)$ and $\mathcal{H}^r_s(a,b)$ coincide, and their corresponding norms $\|\cdot\|_{H^r_s}$ and $\|\cdot\|_{\mathcal{H}^r_s}$ are equivalent.*

Proof. A proof of this lemma for all $r > 0$ can be found in [8, Theorem 2.1 and Remark 2.3]. In what follows we present an alternative proof for non-negative integer values of r: $r = k \in \mathbb{N} \cup \{0\}$. In this case it suffices to show that the norms $\|\cdot\|_{H_s^k}$ and $\|\cdot\|_{\mathcal{H}_s^k}$ are equivalent on the dense subset $C^\infty[a,b]$ of both $H_s^k(a,b)$ (Remark 3.5.8) and $\mathcal{H}_s^k(a,b)$. But, for $v \in C^\infty[a,b]$, using (3.5.6), Parseval's identity in L^2_{s+k} and Lemma 3.5.2 we see that for every integer $k \geq 0$ we have $\|v^{(k)}\|_{L^2_{s+k}} = \sum_{j=k}^\infty |v^{(k)}_{j-k,s+k}|^2 = \sum_{j=k}^\infty |v_{j,s}|^2/|B_j^k|^2$. From Lemma 3.5.3 we then obtain

$$D_1 \sum_{j=k}^\infty |v_{j,s}|^2 j^{2k} \leq \|v^{(k)}\|^2_{L^2_{s+k}} \leq D_2 \sum_{j=k}^\infty |v_{j,s}|^2 j^{2k}$$

for certain constants D_1 and D_2, where $v^{(k)}_{j-k,s+k}$. In view of the inequalities

$$(1 + j^{2k}) \leq (1 + j^2)^k \leq (2j^2)^k \leq 2^k(1 + j^{2k})$$

the claimed norm equivalence for $r = k \in \mathbb{N} \cup \{0\}$ and $v \in C^\infty[a,b]$ follows. □

Sharp regularity results for the Fractional Laplacian in the Sobolev space $H_s^r(a,b)$ can now be obtained easily.

Theorem 3.5.12. *Let $r \geq 0$. Then the weighted fractional Laplacian operator* (3.4.4) *can be extended uniquely to a continuous linear map $(-\Delta)^s_\omega$ from $H_s^{r+2s}(a,b)$ into $H_s^r(a,b)$. The extended operator is bijective and bicontinuous.*

Proof. Without loss of generality, we assume $(a,b) = (-1,1)$. Let $\phi \in H_s^{r+2s}(-1,1)$, and let $\phi^n = \sum_{j=0}^n \phi_j \tilde{C}_j^{(s+1/2)}$ where ϕ_j denotes the Gegenbauer coefficient of ϕ as given by equation (3.5.3) with $v = \phi$. According to Corollary 3.4.5 we have $(-\Delta)^s_\omega \phi^n = \sum_{j=0}^n \lambda_j^s \phi_j \tilde{C}_j^{(s+1/2)}$. In view of Remarks 3.5.8 and 3.4.6 it is clear that $(-\Delta)^s_\omega \phi^n$ is a Cauchy sequence (and thus a convergent sequence) in $H_s^r(-1,1)$. We may thus define

$$(-\Delta)^s_\omega \phi = \lim_{n\to\infty} (-\Delta)^s_\omega \phi^n = \sum_{j=0}^\infty \lambda_j^s \phi_j \tilde{C}_j^{(s+1/2)} \in H_s^r(-1,1).$$

The bijectivity and bicontinuity of the extended mapping follows easily, in view of Remark 3.4.6, as does the uniqueness of continuous extension. The proof is complete. □

Corollary 3.5.13. *The solution u of* (3.1.1) *with right-hand side $f \in H_s^r(a,b)$ ($r \geq 0$) can be expressed in the form $u = \omega^s \phi$ for some $\phi \in H_s^{r+2s}(a,b)$.*

Proof. Follows from Theorem 3.5.12 and Remark 3.4.2. □

The classical smoothness of solutions of equation (3.1.1) for sufficiently smooth right-hand sides results from the following version of the "Sobolev embedding" theorem.

Theorem 3.5.14 (Sobolev's Lemma for weighted spaces)**.** *Let $s \geq 0$, $k \in \mathbb{N} \cup \{0\}$ and $r > 2k+s+1$. Then we have a continuous embedding $H_s^r(a,b) \subset C^k[a,b]$ of $H_s^r(a,b)$ into the Banach space $C^k[a,b]$ of k-continuously differentiable functions in $[a,b]$ with the usual norm $\|v\|_k$ (given by the sum of the L^∞ norms of the function and the k-th derivative): $\|v\|_k = \|v\|_\infty + \|v^{(k)}\|_\infty$.*

Proof. Without loss of generality we restrict attention to $(a,b) = (-1,1)$. Let $0 \leq \ell \leq k$ and let $v \in H_s^r(-1,1)$ be given. Using the expansion (3.5.2) and in view of the relation (3.5.4) for the derivative of a Gegenbauer polynomial, we consider the partial sums

$$v_n^{(\ell)}(x) = 2^\ell \prod_{i=1}^{\ell}(s+i-1/2) \sum_{j=\ell}^{n} \frac{v_j}{h_j^{(s+1/2)}} C_{j-\ell}^{(s+\ell+1/2)}(x) \tag{3.5.15}$$

that result as the partial sums corresponding to (3.5.2) up to $j = n$ are differentiated ℓ times. But we have the estimate

$$\|C_n^{(s+1/2)}\|_\infty \sim O(n^{2s}). \tag{3.5.16}$$

which is an immediate consequence of [76, Theorem 7.33.1]. Thus, taking into account (3.5.11), we obtain

$$|v_n^{(\ell)}(x)| \leq C(\ell) \sum_{j=0}^{n-\ell} \frac{|v_{j+\ell}|}{h_{j+\ell}^{(s+1/2)}} |C_j^{(s+\ell+1/2)}(x)| \leq C(\ell) \sum_{j=0}^{n-\ell} (1+j^2)^{(s+2\ell)/2+1/4} |v_{j+\ell}|,$$

for some constant $C(\ell)$. Multiplying and dividing by $(1+j^2)^{r/2}$ and applying the Cauchy-Schwartz inequality in the space of square summable sequences it follows that

$$|v_n^{(\ell)}(x)| \leq C(\ell) \left(\sum_{j=0}^{n-\ell} \frac{1}{(1+j^2)^{r-(s+2\ell+1/2)}} \right)^{1/2} \left(\sum_{j=0}^{n-\ell} (1+j^2)^r |v_{j+\ell}|^2 \right)^{1/2}. \tag{3.5.17}$$

We thus see that, provided $r - (s + 2\ell + 1/2) > 1/2$ (or equivalently, $r > 2\ell + s + 1$), $v_n^{(\ell)}$ converges uniformly to $\frac{\partial^\ell}{\partial x^\ell} v(x)$ (cf. [68, Th. 7.17]) for all ℓ with $0 \leq \ell \leq k$. It follows that $v \in C^k[-1,1]$, and, in view of (3.5.17), it is easily checked that there exists a constant $M(\ell)$ such that $\|\frac{\partial^{(\ell)}}{\partial x^k} v(x)\|_\infty \leq M(\ell)\|v\|_s^r$ for all $0 \leq \ell \leq k$. The proof is complete. □

Remark 3.5.15. *In order to check that the previous result is sharp we consider an example in the case $k = 0$: the function $v(x) = |\log(x)|^\beta$ with $0 < \beta < 1/2$ is not bounded, but a straightforward computation shows that, for $s \in \mathbb{N}$, $v \in \mathcal{H}_s^{s+1}(0,1)$, or equivalently (see Lemma 3.5.11), $v \in H_s^{s+1}(0,1)$.*

Corollary 3.5.16. *The weighted fractional Laplacian operator* (3.4.4) *maps bijectively the space $C^\infty[a,b]$ into itself.*

Proof. Follows directly from Theorem 3.5.12 together with lemmas 3.5.2, 3.5.3 and 3.5.14. □

3.5.2 Analytic Regularity, single interval case

Let f denote an analytic function defined in the closed interval $[-1,1]$. Our analytic regularity results for the solution of equation (3.1.1) relies on consideration of analytic extensions of the function f to relevant neighborhoods of the interval $[-1,1]$ in the complex plane. We thus consider the *Bernstein ellipse* $\mathcal{E}_\rho$, that is, the ellipse with foci ± 1 whose minor and major semiaxial lengths

add up to $\rho \geq 1$. We also consider the closed set $\mathcal{B}_\rho$ in the complex plane which is bounded by $\mathcal{E}_\rho$ (and which includes $\mathcal{E}_\rho$, of course). Clearly, any analytic function f over the interval $[-1,1]$ can be extended analytically to $\mathcal{B}_\rho$ for some $\rho > 1$. We thus consider the following set of analytic functions.

Definition 3.5.17. *For each $\rho > 1$ let A_ρ denote the normed space of analytic functions $A_\rho = \{f \colon f$ is analytic on $\mathcal{B}_\rho\}$ endowed with the L^∞ norm $\| \cdot \|_{L^\infty(\mathcal{B}_\rho)}$.*

Theorem 3.5.18. *For each $f \in A_\rho$ we have $((-\Delta)^s_\omega)^{-1} f \in A_\rho$. Further, the mapping $((-\Delta)^s_\omega)^{-1} : A_\rho \to A_\rho$ is continuous.*

Proof. Let $f \in A_\rho$ and let us consider the Gegenbauer expansions

$$f = \sum_{j=0}^{\infty} f_j \tilde{C}_j^{(s+1/2)} \quad \text{and} \quad ((-\Delta)^s_\omega)^{-1} f = \sum_{j=0}^{\infty} (\lambda_j^s)^{-1} f_j \tilde{C}_j^{(s+1/2)}. \tag{3.5.18}$$

In order to show that $((-\Delta)^s_\omega)^{-1} f \in A_\rho$ it suffices to show that the right-hand series in this equation converges uniformly within $\mathcal{B}_{\rho_1}$ for some $\rho_1 > \rho$. To do this we utilize bounds on both the Gegenbauer coefficients and the Gegenbauer polynomials themselves.

In order to obtain suitable coefficient bounds, we note that, since $f \in A_\rho$, there indeed exists $\rho_2 > \rho$ such that $f \in A_{\rho_2}$. It follows [85] that the Gegenbauer coefficients decay exponentially. More precisely, for a certain constant C we have the estimate

$$|f_j| \leq C \max_{z \in \mathcal{B}_{\rho_2}} |f(z)| \rho_2^{-j} j^{-s} \quad \text{for some} \quad \rho_2 > \rho, \tag{3.5.19}$$

which follows directly from corresponding bounds [85, eqns 2.28, 2.8, 1.1, 2.27] on Jacobi coefficients. (Here we have used the relation

$$C_j^{(s+1/2)} = r_j^s P_j^{(s,s)} \quad \text{with} \quad r_j^s = \frac{(2s+1)_j}{(s+1)_j} = O(j^s)$$

that expresses Gegenbauer polynomials $C_j^{(s+1/2)}$ in terms of Jacobi polynomials $P_j^{(s,s)}$.)

In order to the adequately account for the growth of the Gegenbauer polynomials, on the other hand, we consider the estimate

$$\frac{\|C_j^{(s+1/2)}\|_{L^\infty(\mathcal{B}_{\rho_1})}}{h_j^{(s+1/2)}} \leq D \rho_1^j \quad \text{for all} \quad \rho_1 > 1, \tag{3.5.20}$$

which follows directly from [82, Theorem 3.2] and equation (3.5.11), where $D = D(\rho_1)$ is a constant which depends on ρ_1.

Let now $\rho_1 \in [\rho, \rho_2)$. In view of (3.5.19) and (3.5.20) we see that the j-th term of the right-hand series in equation (3.5.18) satisfies

$$\left| \frac{\lambda_j^s f_j C_j^{(s+1/2)}(x)}{h_j^{(s+1/2)}} \right| \leq C D(\rho_1) \left(\frac{\rho_1}{\rho_2} \right)^j j^{-s} (\lambda_j^s)^{-1} \max_{z \in \mathcal{B}_{\rho_1}} |f(z)| \tag{3.5.21}$$

throughout $\mathcal{B}_{\rho_1}$. Taking $\rho_1 \in (\rho, \rho_2)$ we conclude that the series converges uniformly in $\mathcal{B}_{\rho_1}$, and that the limit is therefore analytic throughout $\mathcal{B}_\rho$, as desired. Finally, taking $\rho_1 = \rho$ in (3.5.21) we obtain the estimates

$$\|((-\Delta)^s_\omega)^{-1} f\|_{L^\infty(\mathcal{B}_\rho)} \leq CD(\rho) \sum_{j=0}^{\infty} \left(\frac{\rho}{\rho_2}\right)^j j^{-s} (\lambda_j^s)^{-1} \max_{z \in \mathcal{E}_\rho} |f(z)| \leq E \|f\|_{L^\infty(\mathcal{B}_\rho)}$$

which establish the stated continuity condition. The proof is thus complete. □

Corollary 3.5.19. *Let $f \in A_\rho$. Then the solution u of (3.1.1) can be expressed in the form $u = \omega^s \phi$ for a certain $\phi \in A_\rho$.*

Proof. Follows from Theorem 3.5.18 and Remark 3.4.2. □

Remark 3.5.20. *We can now see that, as indicated in Remark 3.3.8, the smoothness and analyticity theory presented throughout Section 3.5 cannot be duplicated with weights of exponent $2s$, in spite of the "local" regularity result of Theorem 3.3.7—that establishes analyticity of $T[y^\alpha](x)$ around $x = 0$ for both cases, $\alpha = s + n$ and $\alpha = 2s + n$. Indeed, we can easily verify that $T(y^{2s}(1-y)^{2s} y^n)$ cannot be extended analytically to an open set containing $[0, 1]$. If it could, Theorem 3.5.18 would imply that $y^s(1-y)^s$ is an analytic function around $y = 0$ and $y = 1$.*

3.5.3 Sobolev and Analytic Regularity on Multi-interval Domains

This section concerns multi-interval domains Ω of the form (3.2.2). Using the characteristic functions $\chi_{(a_i,b_i)}$ of the individual component interval, letting $\omega^s(x) = \sum_{i=1}^M (x - a_i)^s (b_i - x)^s \chi_{(a_i,b_i)}(x)$ and relying on Corollary 3.2.5, we define the multi-interval weighted fractional Laplacian operator on Ω by $(-\Delta)^s_\omega \phi = (-\Delta)^s[\omega^s \phi]$, where $\phi : \mathbb{R} \to \mathbb{R}$. In view of the various results in previous sections it is natural to use the decomposition $(-\Delta)^s_\omega = \mathcal{K}_s + \mathcal{R}_s$, where $\mathcal{K}_s[\phi] = \sum_{i=1}^M \chi_{(a_i,b_i)} K_s \chi_{(a_i,b_i)} \phi$ is a block-diagonal operator and where $\mathcal{R}_s$ is the associated off-diagonal remainder. Using integration by parts is easy to check that

$$\mathcal{R}_s \phi(x) = C_1(s) \int_{\Omega \setminus (a_j,b_j)} |x - y|^{-1-2s} \omega^s(y) \phi(y) dy \quad \text{for} \quad x \in (a_j, b_j). \tag{3.5.22}$$

Theorem 3.5.21. *Let Ω be given as in Definition 3.2.1. Then, given $f \in L^2_s(\Omega)$, there exists a unique $\phi \in L^2_s(\Omega)$ such that $(-\Delta)^s_\omega \phi = f$. Moreover, for $f \in H^r_s(\Omega)$ (resp. $f \in A_\rho(\Omega)$) we have $\phi \in H^{r+2s}_s(\Omega)$ (resp. $\phi \in A_\nu(\Omega)$ for some $\nu > 1$).*

Proof. Since $(-\Delta)^s_\omega = (\mathcal{K}_s + \mathcal{R}_s)$, left-multiplying the equation $(-\Delta)^s_\omega \phi = f$ by $\mathcal{K}_s^{-1}$ yields

$$\left(I + \mathcal{K}_s^{-1} \mathcal{R}_s\right) \phi = \mathcal{K}_s^{-1} f. \tag{3.5.23}$$

The operator $\mathcal{K}_s^{-1}$ is clearly compact in $L^2_s(\Omega)$ since the eigenvalues λ_j^s tend to infinity as $j \to \infty$ (cf. (3.4.10)). On the other hand, the kernel of the operator $\mathcal{R}_s$ is analytic, and therefore $\mathcal{R}_s$ is continuous (and, indeed, also compact) in $L^2_s(\Omega)$. It follows that the operator $\mathcal{K}_s^{-1} \mathcal{R}_s$ is compact

in $L^2_s(\Omega)$, and, thus, the Fredholm alternative tells us that equation (3.5.23) is uniquely solvable in $L^2_s(\Omega)$ provided the left-hand side operator is injective.

To establish the injectivity of this operator, assume $\phi \in L^2_s$ solves the homogeneous problem. Then $\mathcal{K}_s(\phi) = -\mathcal{R}_s(\phi)$, and since $\mathcal{R}_s(\phi)$ is an analytic function of x, in view of the mapping properties established in Theorem 3.5.18 for the self operator K_s (which coincides with the single-interval version of the operator $(-\Delta)^s_\omega$)), we conclude the solution ϕ to this problem is again analytic. Thus, a solution to (3.1.1) for a null right-hand side f can be expressed in the form be $u = \omega^s \phi$ for a certain function ϕ which is analytic throughout Ω. But this implies that the function $u = \omega^s \phi$ belongs to the classical Sobolev space $H^s(\Omega)$. (To check this fact we consider that (a) $\omega^s \in H^s(\Omega)$, since, by definition, the Fourier transform of ω^s coincides (up to a constant factor) with the confluent hypergeometric function $M(s+1, 2s+2, \xi)$ whose asymptotics [2, eq. 13.5.1] show that ω^s in fact belongs to the classical Sobolev space $H^{s+1/2-\varepsilon}(\Omega)$ for all $\varepsilon > 0$; and (b) the product fg of functions f, g in $H^s(\Omega) \cap L^\infty(\Omega)$ is necessarily an element of $H^s(\Omega)$—as the Aronszajn-Gagliardo-Slobodeckij semi-norm [61] of fg can easily be shown to be finite for such functions f and g, which implies $fg \in H^s(\Omega)$ [61, Prop 3.4]). Having established that $u = \omega^s \phi \in H^s(\Omega)$, the injectivity of the operator in (3.5.23) in $L^2_s(\Omega)$ follows from the uniqueness of H^s solutions, which is established for example in [3]. As indicated above, this injectivity result suffices to establish the claimed existence of an $L^2_s(\Omega)$ solution for each $L^2_s(\Omega)$ right-hand side.

Assuming f is analytic (resp. belongs to $H^r_s(\Omega)$), finally, the regularity claims now follow directly from the single-interval results of Sections 3.5.1 and 3.5.2, since a solution ϕ of $(-\Delta)^s_\omega \phi = f$ satisfies

$$\mathcal{K}_s(\phi) = f - \mathcal{R}_s(\phi). \tag{3.5.24}$$

The proof is now complete. □

3.6 High Order Gegenbauer-Nyström Methods for the Fractional Laplacian

This section presents rapidly-convergent numerical methods for single- and multi-interval fractional Laplacian problems. In particular, this section establishes that the proposed methods, which are based on the theoretical framework introduced above in this Chapter, converge (i) exponentially fast for analytic right-hand sides f, (ii) superalgebraically fast for smooth f, and (iii) with convergence order r for $f \in H^r_s(\Omega)$.

3.6.1 Single-Interval Method: Gegenbauer Expansions

In view of Corollary 3.4.5, a spectrally accurate algorithm for solution of the single-interval equation (3.4.5) (and thus equation (3.1.1) for $\Omega = (a, b)$) can be obtained from use of Gauss-Jacobi quadratures. Assuming $(a, b) = (-1, 1)$ for notational simplicity, the method proceeds as follows: 1) The continuous scalar product (3.5.3) with $v = f$ is approximated with spectral accuracy (and, in fact, exactly whenever f is a polynomial of degree less or equal to $n+1$) by means of the discrete

inner product

$$f_j^{(n)} := \frac{1}{h_j^{(s+1/2)}} \sum_{i=0}^{n} f(x_i) C_j^{(s+1/2)}(x_i) w_i, \tag{3.6.1}$$

where $(x_i)_{i=0}^n$ and $(w_i)_{i=0}^n$ denote the nodes and weights of the Gauss-Jacobi quadrature rule of order $2n+1$. (As is well known [43], these quadrature nodes and weights can be computed with full accuracy at a cost of $O(n)$ operations.) 2) For each i, the necessary values $C_j^{(s+1/2)}(x_i)$ can be obtained for all j via the three-term recurrence relation (3.4.8), at an overall cost of $O(n^2)$ operations. The algorithm is then completed by 3) Explicit evaluation of the spectrally accurate approximation

$$\phi_n := K_{s,n}^{-1} f = \sum_{j=0}^{n} \frac{f_j^{(n)}}{\lambda_j^s h_j^{(s+1/2)}} C_j^{(s+1/2)} \tag{3.6.2}$$

that results by using the expansion (3.5.2) with $v = f$ followed by an application of equation (3.4.11) and subsequent truncation of the resulting series up to $j = n$. The algorithm requires accurate evaluation of certain ratios of Gamma functions of large arguments; see equations (3.4.10) and (3.5.1), for which we use the Stirling's series as in [43, Sec 3.3.1]. The overall cost of the algorithm is $O(n^2)$ operations. The accuracy of this algorithm, in turn, is studied in section 3.6.3.

3.6.2 Multiple Intervals: An iterative Nyström Method

This section presents a spectrally accurate iterative Nyström method for the numerical solution of equation (3.1.1) with Ω as in (3.2.2). This solver, which is based on use of the equivalent second-kind Fredholm equation (3.5.23), requires (a) Numerical approximation of $\mathcal{K}_s^{-1} f$, (b) Numerical evaluation of the "forward-map" $(I + \mathcal{K}_s^{-1}\mathcal{R}_s)[\tilde{\phi}]$ for each given function $\tilde{\phi}$, and (c) Use of the iterative linear-algebra solver GMRES [69]. Clearly, the algorithm in Section 3.6.1 provides a numerical method for the evaluation of each block in the block-diagonal inverse operator $\mathcal{K}_s^{-1}$. Thus, in order to evaluate the aforementioned forward map it now suffices to evaluate numerically the off-diagonal operator $\mathcal{R}_s$ in equation (3.5.22).

An algorithm for evaluation of $\mathcal{R}_s[\tilde{\phi}](x)$ for $x \in (a_j, b_j)$ can be constructed on the basis of the Gauss-Jacobi quadrature rule for integration over the interval (a_ℓ, b_ℓ) with $\ell \neq j$, in a manner entirely analogous to that described in Section 3.6.1. Thus, using Gauss-Jacobi nodes and weights $y_i^{(\ell)}$ and $w_i^{(\ell)}$ $(i = 1, \ldots, n_\ell)$ for each interval (a_ℓ, b_ℓ) with $\ell \neq j$ we may construct a discrete operator R_n that can be used to approximate $\mathcal{R}_s[\tilde{\phi}](x)$ for each given function $\tilde{\phi}$ and for all observation points x in the set of Gauss-Jacobi nodes used for integration in the interval (a_j, b_j) (or, in other words, for $x = y_k^{(j)}$ with $k = 1, \ldots, n_j$). Indeed, consideration of the numerical approximation

$$R[\tilde{\phi}](y_k^{(j)}) \approx \sum_{\ell \neq j} \sum_{i=0}^{n_\ell} |y_k^{(j)} - y_i^{(\ell)}|^{-2s-1} \tilde{\phi}(y_i^{(\ell)}) w_i^{(\ell)}$$

suggests the following definition. Using a suitable ordering to define a vector Y that contains all unknowns corresponding to $\tilde{\phi}(y_i^{(\ell)})$, and, similarly, a vector F that contains all of the values $f(y_i^{(\ell)})$,

the discrete equation to be solved takes the form

$$(I + K_{s,n}^{-1} R_{s,n}) Y = K_{s,n}^{-1}[F]$$

where R_n and $K_{s,n}^{-1}$ are the discrete operator that incorporate the aforementioned ordering and quadrature rules.

With the forward map $(I + K_{s,n}^{-1} R_{s,n})$ in hand, the multi-interval algorithm is completed by means of an application of a suitable iterative linear algebra solver; our implementations are based on the Krylov-subspace iterative solver GMRES [69]. Thus, the overall cost of the algorithm is $O(m \cdot n^2)$ operations, where m is the number of required iterations. (Note that the use of an iterative solver allows us to avoid the actual construction and inversion of the matrices associated with the discrete operators in equation (3.6.2), which would lead to an overall cost of the order of $O(n^3)$ operations.) As the equation to be solved originates from a second kind equation, it is not unreasonable to anticipate that, as we have observed without exception (and as illustrated in Section 3.7), a small number of GMRES iterations suffices to meet a given error tolerance.

3.6.3 Error estimates

The convergence rates of the algorithms proposed in Sections 3.6.1 and 3.6.2 are studied in what follows. In particular, as shown in Theorems 3.6.1 and 3.6.3, the algorithm's errors are exponentially small for analytic f, they decay superalgebraically fast (faster than any power of meshsize) for infinitely smooth right-hand sides, and with a fixed algebraic order of accuracy $O(n^{-r})$ whenever f belongs to the Sobolev space $H_s^r(\Omega)$ (cf. Section 3.5.1). For conciseness, fully-detailed proofs are presented in the single-interval case only. A sketch of the proofs for the multi-interval cases is presented in Corollary 3.6.4.

Theorem 3.6.1. *Let $r > 0$, $0 < s < 1$. Then, there exists a constant D such that the error $e_n(f) = (K_s^{-1} - K_{s,n}^{-1})(f)$ in the numerical approximation* (3.6.2) *for the solution of the single interval problem* (3.4.5) *satisfies*

$$\|e_n(f)\|_{H_s^{\ell+2s}(a,b)} \leq D n^{\ell - r} \|f\|_{H_s^r(a,b)} \tag{3.6.3}$$

for all $f \in H_s^r(a,b)$. In particular, the L_s^2-bound

$$\|e_n(f)\|_{L_s^2(a,b)} \leq D n^{-r} \|f\|_{H_s^r(a,b)}. \tag{3.6.4}$$

holds for every $f \in H_s^r(a,b)$.

Proof. As before, we work with $(a,b) = (-1,1)$. Let f be given and let p_n denote the n-degree polynomial that interpolates f at the Gauss-Gegenbauer nodes $(x_i)_{0 \leq i \leq n}$. Since the Gauss-Gegenbauer quadrature is exact for polynomials of degree less or equal than $2n+1$, the approximate Gegenbauer coefficient $f_j^{(n)}$ (equation (3.6.1)) coincides with the corresponding exact Gegenbauer coefficient of p_n: using the scalar product (3.4.7) we have

$$f_j^{(n)} = \sum_{i=0}^{n} p_n(x_i) \tilde{C}_j^{(s+1/2)}(x_i) w_i = \langle p_n, \tilde{C}_j^{(s+1/2)} \rangle_s.$$

It follows that the discrete operator $K_{s,n}$ satisfies $K_{s,n}^{-1} f = K_s^{-1} p_n$. Therefore, for each $\ell \geq 0$ we have

$$\|e_n(f)\|_{H_s^{\ell+2s}(-1,1)} = \|K_s^{-1}(f - p_n)\|_{H_s^{\ell+2s}(-1,1)} \leq D_2 \|f - p_n\|_{H_s^{\ell}(-1,1)}, \tag{3.6.5}$$

where D_2 denotes the continuity modulus of the operator $K_s^{-1} : H_s^{\ell}(-1,1) \to H_s^{\ell+2s}(-1,1)$ (see Theorem 3.5.12 and equation (3.4.4)). From [42, Theorem 4.2] together with the norm equivalence established in Lemma 3.5.11, we have, for all $\ell \leq r$, the following estimate for the interpolation error of a function $f \in H_s^r(-1,1)$:

$$\|f - p_n\|_{H_s^{\ell}(-1,1)} < C n^{\ell - r} \|f\|_{H_s^r(-1,1)} \text{ for } f \in H_s^r(-1,1), \tag{3.6.6}$$

which together with (3.6.5) shows that (3.6.3) holds. The proof is complete. □

Remark 3.6.2. *A variety of numerical results in Section 3.7 suggest that the estimate* (3.6.3) *is of optimal order, and that the estimate* (3.6.4) *is suboptimal by a factor that does not exceed* $n^{-1/2}$. *In view of equation* (3.6.5)*, devising optimal error estimates in the* $L_s^2(a,b)$ *norm is equivalent to that of finding optimal estimates for the interpolation error in the space* $H_s^{-2s}(a,b)$. *Such negative-norm estimates are well known in the context of Galerkin discretizations (see e.g. [14]); the generalization of such results to the present context is left for future work.*

Theorem 3.6.3. *Let* $f \in A_\rho$ *be given (Definition 3.5.17) and let* $e_n(f) = (K_s^{-1} - K_{s,n}^{-1})(f)$ *denote the single-interval* n*-point error arising from the numerical method presented in Section 3.6.1. Then the error estimate*

$$\|e_n(f)\|_{A_\nu} \leq C n^s \left(\frac{\nu}{\rho}\right)^n \|f\|_{A_\rho}, \quad \text{for all } \nu \text{ such that } \quad 1 < \nu < \rho \tag{3.6.7}$$

holds. In particular, the operators $K_{s,n}^{-1} : A_\rho \to A_\rho$ *converge in norm to the continuous operators* K_s^{-1} *as* $n \to \infty$.

Proof. Equations (3.4.4), (3.5.18), (3.6.1) and (3.6.2) tell us that

$$(K_s^{-1} - K_{s,n}^{-1}) f = \sum_{j=0}^{n} \left(f_j - f_j^{(n)}\right) (\lambda_j^s)^{-1} \tilde{C}_j^{(s+1/2)} + \sum_{j=n+1}^{\infty} f_j (\lambda_j^s)^{-1} \tilde{C}_j^{(s+1/2)}. \tag{3.6.8}$$

In order to obtain a bound for the quantities $|f_j - f_j^{(n)}|$ we utilize the estimate

$$\left| \int_{-1}^{1} v(x)(1-x^2)^s dx - \sum_{i=0}^{n} v(x_i) w_i \right| \leq \frac{C n^s}{\rho^{2n}} \|v\|_{L^\infty(\mathcal{B}_\rho)}. \tag{3.6.9}$$

that is provided in [85, Theorem 3.2] for the Gauss-Gegenbauer quadrature error for a function $v \in \mathcal{A}_\rho$. Letting $v = f\, \tilde{C}_j^{(s+1/2)}$ with $j \leq n$, equation (3.6.9) and (3.5.20) yield

$$|f_j - f_j^{(n)}| \leq \frac{C D n^s}{\rho^n} \|f\|_{L^\infty(\mathcal{B}_\rho)}. \tag{3.6.10}$$

It follows that the infinity norm of the left-hand side in equation (3.6.8) satisfies

$$\|(K_s^{-1} - K_{s,n}^{-1})f\|_{L^\infty(B_\nu)} \leq Cn^s \left(\frac{\nu}{\rho}\right)^n \|f\|_{L^\infty(\mathcal{B}_\rho)} \text{ for all } \nu < \rho$$

for some (new) constant C, as it can be checked by considering (3.5.20), (3.6.10) and Remark 3.4.6 for the finite sum in (3.6.8), and (3.5.19) (3.5.20) and Remark 3.4.6 for the tail of the series. The proof is now complete.

□

Corollary 3.6.4. *The algebraic order of convergence established in the single-interval Theorem 3.6.1 is valid in the multi-interval Sobolev case as well. Further, an exponentially small error in the infinity norm of $C^0(\Omega)$ results in the analytic multi-interval case (cf. Theorem 3.6.3).*

Proof. It is is easy to check that the family $\{R_{s,n}\}$ $(n \in \mathbb{N})$ of discrete approximations of the off-diagonal operator $\mathcal{R}_s$ is collectively compact [46] in the space $H_s^r(\Omega)$ $(r > 0)$. Indeed, it suffices to show that, for a given bounded sequence $\{\phi_n\} \subset H_s^r(\Omega)$, the sequence $R_{s,n}[\phi_n]$ admits a convergent subsequence in $H_s^r(\Omega)$. But, selecting $0 < r' < r$, by Remark 3.5.9 we see that ϕ_n admits a convergent subsequence in $H_s^{r'}(\Omega)$. Thus, in view of the smoothness of the kernel of the operator $\mathcal{R}_s$, the bounds for the interpolation error (3.6.6) applied to the product of ϕ_n and the kernel (and its derivatives), and the fact that the Gauss-Gegenbauer quadrature rule is exact for polynomials of degree $\leq 2n+1$, $R_{s,n}[\phi_n]$ converges in $H_s^t(\Omega)$ for all $t \in \mathbb{R}$ and, in particular for $t = r$. Thus, the family $\{R_{s,n}\}$ is collectively compact in $H_s^r(\Omega)$, as claimed, and therefore so is $K_{n,s}^{-1}R_{n,s}$. Then [46, Th. 10.12] shows that, for some constant C, we have the bound

$$\|\phi_n - \phi\|_{H_s^r} \leq C\|(\mathcal{K}_s^{-1}\mathcal{R}_s - K_{n,s}^{-1}R_{n,s})\phi\|_{H_s^r} + \|\mathcal{K}_s^{-1} - K_{n,s}^{-1})f\|. \tag{3.6.11}$$

The proof in the Sobolev case now follows from (3.6.11) together with equations (3.6.5) and (3.6.6) and the error estimates in Theorem 3.6.1. The proof in the analytic case, finally, follows from the bound (3.6.9), Theorem 3.6.3 and an application of Theorem 3.5.14 to the left-hand side of equation (3.6.11). □

3.7 Numerical Results

This section presents a variety of numerical results that illustrate the properties of algorithms introduced in Section 3.6. The efficiency of these method is largely independent of the value of the parameter s, and, thus, independent of the sharp boundary layers that arise for small values of s. To illustrate the efficiency of the proposed Gegenbauer-based Nyström numerical method and the sharpness of the error estimates developed in Section 3.6, test cases containing both smooth and non-smooth right hand sides are considered. In all cases the numerical errors were estimated by comparison with reference solutions obtained for larger values of N. Additionally, solutions obtained by the present Gegenbauer approach were checked to agree with those provided by the finite-element method introduced in [3], thereby providing an independent verification of the correctness of proposed methodology.

Figure 3.7.1: Exponential convergence for $f(x) = \frac{1}{x^2+0.01}$.

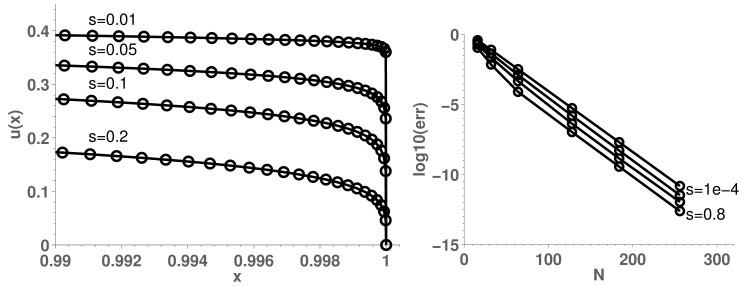

Left: Solution detail near the domain boundary for f equal to the Runge function mentioned in the text. Right: Convergence for various values of s. Computation time: 0.0066 sec. for $N = 16$ to 0.05 sec. for $N = 256$.

Figure 3.7.1 demonstrates the exponentially fast convergence that takes place for a right-hand side given by the Runge function $f(x) = \frac{1}{x^2+0.01}$—which is analytic within a small region of the complex plane around the interval $[-1, 1]$, and for values of s as small as 10^{-4}. The present Matlab implementation of our algorithms produces these solutions with near machine precision in computational times not exceeding 0.05 seconds.

Figure 3.7.2: Convergence in the $H_s^{2s}(-1,1)$ and $L_s^2(-1,1)$ norms for $f(x) = |x|$. In this case, $f \in H_s^{3/2-\varepsilon}(-1,1)$.

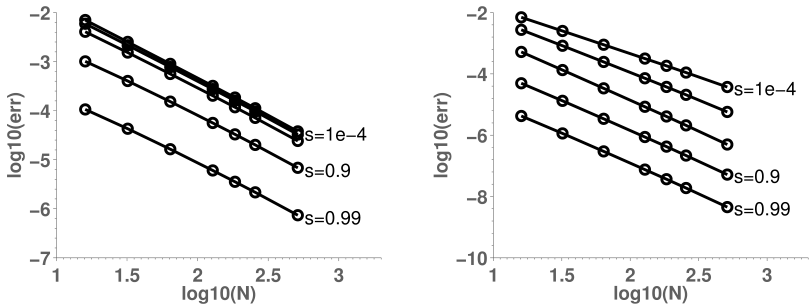

Left: errors in $H_s^{2s}(-1,1)$ norm of order 1.5. Right: errors in $L_s^2(-1,1)$ norm, orders range from 1.5 to 2.

Results concerning a problem containing the non-smooth right-hand side $f(x) = |x|$ (for which, as can be checked in view of Corollary 3.5.4 and Definition (3.5.6), we have $f \in H_s^{3/2-\varepsilon}(-1,1)$ for any $\varepsilon > 0$ and any $0 \le s \le 1$) are displayed in Fig. 3.7.2. The errors decay with the order predicted by Theorem 3.6.1 in the $H_s^{2s}(-1,1)$ norm, and with a slightly better order than predicted by that theorem for the $L_s^2(-1,1)$ error norm, although the observed orders tend to the predicted order as $s \to 0$ (cf. Remark 3.6.2).

A solution for a multi-interval (two-interval) test problem with right hand side $f = 1$ is displayed in Figure 3.7.3. A total of five GMRES iterations sufficed to reach the errors displayed for each one of the discretizations considered on the right-hand table in Figure 3.7.3. The computational times required for each one of the discretizations listed on the right-hand table are of the order of a few hundredths of a second.

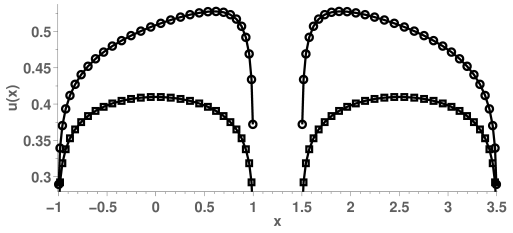

N	rel. err.
8	9.3134e-05
12	1.6865e-06
16	3.1795e-08
20	6.1375e-10
24	1.1857e-11
28	1.4699e-13

Figure 3.7.3: Multiple (upper curves) vs. independent single-intervals solutions (lower curves) with $f = 1$. A total of five GMRES iterations sufficed to achieve the errors shown on the right table for each one of the discretizations considered.

3.8 Appendix to Chapter 3

3.8.1 Proof of Lemma 3.2.4

Let

$$F_\varepsilon(x) = \int_{\Omega\setminus B_\varepsilon(x)} \Phi_s(x-y)v(y)dy.$$

Then, by definition we have

$$\lim_{\varepsilon\to 0}\frac{d}{dx}F_\varepsilon(x) = P.V.\int_\Omega \frac{\partial}{\partial x}\Phi_s(x-y)v(y)dy.$$

We note that interchanging the limit and differentiation processes on the left hand side of this equation would result precisely in the right-hand side of equation (3.2.14)—and the lemma would thus follow. Since F_ε converges throughout Ω as $\varepsilon \to 0$, to show that the order of the limit and differentiation can indeed be exchanged it suffices to show [68, Th. 7.17] that the quantity $\frac{d}{dx}F_\varepsilon(x)$ converges uniformly over compact subsets $K \subset \Omega$ as $\varepsilon \to 0$.

To establish the required uniform convergence property over a given compact set $K \subset \Omega$ let us first define a larger compact set $K^* = [a, b] \subset \Omega$ such that $K \subset U \subset K^*$ where U is an open set. Letting ε_0 be sufficiently small so that $B_{\varepsilon_0}(x) \subset K^*$ for all $x \in K$, for each $\varepsilon < \varepsilon_0$ we may then write

$$\frac{\partial}{\partial x}F_\varepsilon = \int_{\Omega\setminus K^*}\frac{\partial}{\partial x}\Phi_s(x-y)v(y)dy + \int_{K^*\setminus B_\varepsilon(x)}\frac{\partial}{\partial x}\Phi_s(x-y)v(y)dy.$$

The first term on the right-hand side of this equation does not depend on ε for all $x \in K$. To analyze the second term we consider the expansion $v(y) = v(x) + (y-x)R(x,y)$ and we write $\int_{K^*}\frac{\partial}{\partial x}\Phi_s(x-y)v(y)dy = \Gamma^1_\varepsilon(x) + \Gamma^2_\varepsilon(x)$ where

$$\Gamma^1_\varepsilon(x) = v(x)\int_{K^*\setminus B_\varepsilon(x)}\frac{\partial}{\partial x}\Phi_s(x-y)dy \quad \text{and}$$
$$\Gamma^2_\varepsilon(x) = \int_{K^*\setminus B_\varepsilon(x)}\frac{\partial}{\partial x}\Phi_s(x-y)(y-x)R(x,y)dy.$$

Since $K^* = [a, b]$, for each $\varepsilon < \varepsilon_0$ and each $x \in K$ the quantity $\Gamma^1_\varepsilon(x)$ can be expressed in the form

$$\Gamma^1_\varepsilon(x) = -v(x)\left(\Phi_s(x-y)\big|^{y=b}_{y=x+\varepsilon} + \Phi_s(x-y)\big|^{y=x-\varepsilon}_{y=a}\right)$$

which, in view of the relation $\Phi_s(-\varepsilon) = \Phi_s(\varepsilon)$, is independent of ε. The uniform convergence of $\Gamma^1_\varepsilon(x)$ over K therefore holds trivially.

The term $\Gamma^2_\varepsilon(x)$, finally, equals

$$\int_{K^*\setminus B_\varepsilon(x)} N(x-y)R(x,y),$$

where $N(x,y) = \frac{\partial}{\partial x}\Phi_s(x-y)(y-x)$. Since $v \in C^1(\Omega)$ there exists a constant C_{K,K^*} such that $|R(x,y)| < C_{K,K^*}$ for all (x,y) in the compact set $K \times K^* \subset \Omega \times \Omega$. In particular, for each $x \in K$ the product $N(x-y)R(x,y)$ is integrable over K^*, and therefore the difference between $\Gamma^2_\varepsilon(x)$ and its limit satisfies

$$\left|\Gamma^2_\varepsilon(x) - \lim_{\varepsilon\to 0}\Gamma^2_\varepsilon(x)\right| = \left|\int_{x-\varepsilon}^{x+\varepsilon} N(x-y)R(x,y)dy\right| < C_{K,K^*}\int_{-\varepsilon}^{\varepsilon}|N(z)|\,dz.$$

The uniform convergence of Γ^2_ε over the set K then follows from the integrability of the function $N = N(z)$ around the origin, and the proof is thus complete.

3.8.2 Interchange of infinite summation and P.V. integration in equation (3.3.23)

Lemma 3.8.1. *Upon substitution of* (3.3.22)*, the quantity L^s_n in equation* (3.3.19) *equals the expression on the right-hand side of equation* (3.3.23)*. In detail, for each $x \in (0,1)$ we have*

$$P.V.\int_0^1 J^s(x-y)y^{s-1}\left(\sum_{j=0}^{\infty} q_j y^j\right)y^n dy = \sum_{j=0}^{\infty}\left(P.V.\int_0^1 q_j y^j J^s(x-y)y^{s-1}y^n dy\right), \tag{3.8.1}$$

where $J^s(z) = \operatorname{sgn}(z)|z|^{-2s}$.

Proof. Let $x \in (0,1)$ be given. Then, taking $\delta < \min\{x, 1-x\}$ we re-express the left hand side of (3.8.1) in the form

$$\lim_{\varepsilon\to 0}\left[\int_0^\delta dy + \int_{[\delta,1-\delta]\setminus B_\varepsilon(x)} dy + \int_{1-\delta}^1 dy\right]\left(\sum_{j=0}^{\infty} J^s(x-y)q_j y^{s-1+n+j}\right). \tag{3.8.2}$$

The leftmost and rightmost integrals in this expression are independent of ε, and, in view of (3.3.22), they are both finite. The exchange of these integrals and the corresponding infinite sums follows easily in view of the monotone convergence theorem since the coefficients q_j are all positive.

The middle integral in equation (3.8.2), in turn, can be expressed in the form

$$\lim_{\varepsilon\to 0}\int_{[\delta,1-\delta]\setminus B_\varepsilon(x)} J^s(x-y)\left(\lim_{m\to\infty} v_m(y)\right)dy, \tag{3.8.3}$$

where

$$v_m(y) = y^{s-1}y^n\sum_{j=0}^{m} q_j y^j. \tag{3.8.4}$$

In view of (3.3.22), v_m converges (uniformly) to the smooth function $v_\infty(y) = y^{s-1}y^n(1-y)^{s-1}$ for all y in the present domain of integration. As shown below, interchange of this uniformly convergent series with the PV integral will then allow us to complete the proof of the lemma.

In order to justify this interchange we replace the expansion

$$v_m(y) = v_m(x) + (x-y)R_m(x,y), \quad \text{where } R_m(x,y) = \frac{v_m(y) - v_m(x)}{x-y}.$$

in (3.8.3) and we define

$$F_\varepsilon^1 = v_\infty(x) \int_{[\delta,1-\delta]\setminus B_\varepsilon(x)} J^s(x-y)dy \tag{3.8.5}$$

$$F_\varepsilon^2 = \int_{[\delta,1-\delta]\setminus B_\varepsilon(x)} J^s(x-y)(x-y) \lim_{m\to\infty} R_m(x,y)dy; \tag{3.8.6}$$

clearly the expression in equation (3.8.3) equals $\lim_{\varepsilon\to 0}\left(F_\varepsilon^1 + F_\varepsilon^2\right)$.

The exchange of $\lim_{\varepsilon\to 0}$ and infinite summation for F_ε^1 (in (3.8.5)) follows immediately since $v_m(x)$ does not depend on ε. In order to perform a similar exchange for F_ε^2 in (3.8.6) we first note that

$$\lim_{\varepsilon\to 0} F_\varepsilon^2 = \int_\delta^{1-\delta} J^s(x-y)(x-y) \lim_{m\to\infty} R_m(x,y)dy \tag{3.8.7}$$

in view of the integrand's integrability—which itself follows from the bound

$$\left| J^s(x-y)(x-y) \lim_{m\to\infty} R_m(x,y) \right| \le M \left| J^s(x-y)(x-y) \right|, \tag{3.8.8}$$

(where M is a bound for the derivative $[v_\infty(y)]'$ in the interval $[\delta, 1-\delta]$) together with the integrability of the product $|J^s(x-y)(x-y)|$. But (3.8.7) equals

$$\begin{aligned} \lim_{m\to\infty} \int_\delta^{1-\delta} & J^s(x-y)(x-y)R_m(x,y)dy = \\ & = \lim_{m\to\infty} \lim_{\varepsilon\to 0} \int_{[\delta,1-\delta]\setminus B_\varepsilon(x)} J^s(x-y)(x-y)R_m(x,y)dy. \end{aligned} \tag{3.8.9}$$

Indeed, the first expression results from an application of the dominated convergence theorem—which is justified in view of (3.8.8) since $R_m(x,y)$ is an increasing sequence—while the second equality, which puts our integral in "principal value" form, follows directly in view of the integrand's integrability.

The lemma now follows by substituting first $R_m(x,y) = (v_m(y) - v_m(y))/(x-y)$ and then equation (3.8.4) in the right-hand integral of equation (3.8.9) and combining the result with corresponding sums for F_ε^1 and for the leftmost and rightmost integrals in (3.8.2)—to produce the desired right-hand side in equation (3.8.1). The proof is now complete. □

3.8.3 Interchange of summation order in (3.3.25) for $x \in (0,1)$

Letting

$$a_{jk} = \frac{(1-s)_j}{j!} \frac{(2s)_k}{k!} \frac{1}{s-n-j+k} x^k,$$

in order to show that the summation signs in (3.3.25) can be interchanged it suffices to show that the series $\sum_{j,k} a_{jk}$ is absolutely convergent. To do this we write

$$\sum_{j=0}^{\infty}|a_{jk}| = \frac{(2s)_k}{k!}\, x^k \sum_{j=0}^{\infty} \frac{(1-s)_j}{j!}\frac{1}{|s-n-j+k|} =$$

$$= \frac{(2s)_k}{k!}x^k \left(\sum_{j=0}^{k-n} \frac{(1-s)_j}{j!}\frac{1}{s-n-j+k} + \sum_{j=k-n+1}^{\infty} \frac{(1-s)_j}{j!}\frac{1}{-s+n+j-k} \right).$$

Since $\frac{(1-s)_j}{j!} \sim j^{-s}$ as $j \to \infty$ we obtain

$$\sum_{j=k-n+1}^{\infty} \frac{(1-s)_j}{j!}\frac{1}{-s+n+j-k} \leq C \sum_{j=k-n+1}^{\infty} \frac{j^{-s}}{-s+n+j-k} \leq C(s)$$

and, in view of the fact that, in particular, $\frac{(1-s)_j}{j!}$ is bounded,

$$\sum_{j=0}^{k-n} \frac{(1-s)_j}{j!}\frac{1}{s-n-j+k} \leq \sum_{\ell=0}^{k-n} \frac{1}{s+\ell} = \frac{1}{s} + \sum_{\ell=1}^{k-n} \frac{1}{s+\ell}.$$

It follows that

$$\sum_{k=0}^{\infty}\sum_{j=0}^{\infty}|a_{jk}| \leq \sum_{k=0}^{\infty} \frac{(2s)_k}{k!} \left(C(s) + \sum_{\ell=1}^{k-n} \frac{1}{\ell} \right) x^k$$

and, since $\frac{(2s)_k}{k!} \sim k^{2s-1}$ and $\sum_{\ell=1}^{k-n} \frac{1}{\ell} \sim \ln k$ as $k \to \infty$, the sum $\sum_{j,k} a_{jk}$ is absolutely convergent for every $x \in (0,1)$, as needed.

Chapter 4

Fast 3D Maxwell solvers for bi-periodic structures, including Wood anomalies

This chapter presents high-order Nyström algorithms for the solution of three-dimensional bi-periodic electromagnetic scattering problems at all frequencies. These algorithms, which rely on use of spectral collocation and high-order quadrature rules which accurately capture the Green function singularities, include a three-dimensional version of the shifted Green function approach described in Chapter 2 as well as an associated FFT-based acceleration strategy. The algorithm introduced in this chapter is thus the first effective three dimensional bi-periodic scattering solver which is applicable throughout the spectrum, including Wood anomalies.

This chapter is organized as follows: after a few preliminaries are considered in Section 4.1, Section 4.2 provides an outline of the Nyström-based numerical framework on which the solvers are based, including the construction of the required meshes, high-order quadrature rules and implementation test cases that demonstrate the accuracy of the presented numerical routines. Building upon these elements, Section 4.3 then constructs a hybrid spatial-spectral solver for the electromagnetic bi-periodic scattering problem, and presents a numerical convergence test for the unaccelerated version of the algorithm at and around Wood-anomaly frequencies. Sections 4.4, outlines the acceleration strategy, and it presents numerical results that demonstrate the efficiency of the proposed approach in the present three-dimensional context.

4.1 Problem setup

We consider the problem of evaluating the scattered electromagnetic field (E^{scat}, H^{scat}) that results as an incident field (E^{inc}, H^{inc}) impinges upon the boundary Γ of a perfectly conducting scatterer D. The scatterer D is assumed to be periodic, that is, if $\mathbf{x} \in D$ then $\mathbf{x} + (nd_1, md_2, 0) \in D$ for all $n, m \in \mathbb{Z}$. All three fields, the incident field $(E, H) = (E^{inc}, H^{inc})$, the scattered field $(E, H) = (E^{scat}, H^{scat})$ and the total field $(E^{tot}, H^{tot}) = (E^{scat} + E^{inc}, H^{scat} + H^{inc})$, satisfy the

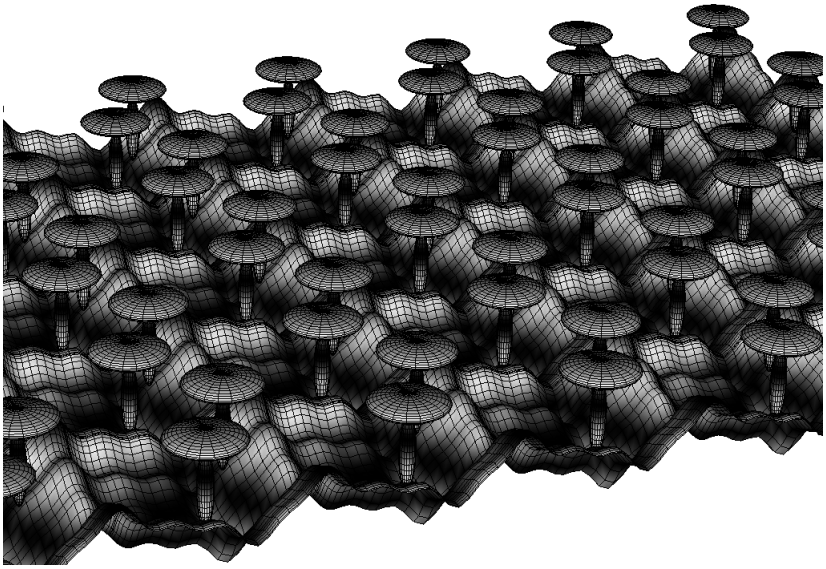

Periodic configuration illuminated by a plane wave.

Maxwell's equations

$$\nabla \times E - ikH = 0, \qquad \nabla \times H - ikE = 0 \qquad \text{in } \mathbf{R}^3 \setminus D. \tag{4.1.1}$$

Throughout this chapter we consider incident fields E^{inc} given by a plane-wave solution of Maxwell's equations—that is, for certain mutually orthogonal vectors $\mathbf{E_i}$ and $\mathbf{k_i}$ we have

$$E^{inc}(\mathbf{x}) = \mathbf{E}_i e^{ik_i \cdot \mathbf{x}}, \quad \text{where} \quad k_i = (\alpha, \beta, -\gamma) \quad \text{and} \quad \mathbf{E}_i = [e_1, e_2, e_3]. \tag{4.1.2}$$

In terms of the azimuth and elevation angles ψ and ϕ and the polarization angle δ, the components of the vectors $\mathbf{E_i}$ and $\mathbf{k_i}$ are given by

$$\alpha = k \sin(\phi) \cos(\psi) \qquad e^1 = \cos(\delta)\cos(\phi)\cos(\psi) + \sin(\delta)\sin(\psi) \tag{4.1.3}$$

$$\beta = k \sin(\phi) \sin(\psi) \qquad e^2 = \cos(\delta)\cos(\phi)\sin(\psi) - \sin(\delta)\cos(\psi) \tag{4.1.4}$$

$$\gamma = k \cos(\phi) \qquad e^3 = \cos(\delta)\sin(\phi) \tag{4.1.5}$$

For $\delta = 0$ (resp. $\delta = \frac{\pi}{2}$) the incident field is said to be H-polarized, or horizontally polarized (resp. V-polarized or vertically polarized).

4.1.1 3D Quasi-Periodic Green Function

In the bi-periodic case, it is known that the scattered $E^{scat}(\mathbf{x})$ admits a Rayleigh expansion of the form

$$E^{scat}(\mathbf{x}) = \sum_{n,m} B_{nm} e^{i\omega_{nm} \cdot \mathbf{x}}, \quad \text{with} \quad B_{nm} \cdot \omega_{nm} = 0, \tag{4.1.6}$$

where, letting U denote the finite set of integers (n,m) such that $\mathrm{k}^2-(\alpha_n)^2-(\beta_m)^2>0$, the wavenumbers $\omega_{nm}=(\alpha_n,\beta_m,\gamma_{nm})$ are given by

$$\alpha_n := \alpha + n\frac{2\pi}{d_1}, \qquad \beta_m := \beta + m\frac{2\pi}{d_2}, \qquad \gamma_{nm} := \begin{cases} \sqrt{\mathrm{k}^2-(\alpha_n)^2-(\beta_m)^2} & , \quad n \in U \\ i\sqrt{(\alpha_n)^2+(\beta_m)^2-\mathrm{k}^2} & , \quad n \notin U. \end{cases} \tag{4.1.7}$$

Calling

$$G_j(X,Y,Z) = \sum_{s=0}^{j}(-1)^s C_s^j\, G(X,Y,Z+mh), \quad \text{where} \quad C_m^j = \binom{j}{s} = \frac{j!}{s!(j-s)!}, \tag{4.1.8}$$

the three-dimensional shifted Green function for a given integer value j, for all $j\geq 3$ the spatial lattice sum

$$\tilde{G}_j^{qper}(X,Y) = \sum_{n=-\infty}^{\infty}\sum_{m=-\infty}^{\infty} e^{-\mathrm{i}\alpha n d_1 - \mathrm{i}\beta m d_2} G_j(X+nd_1, Y+md_2, Z) \tag{4.1.9}$$

provides [22] a rapidly (algebraically) convergent quasi-periodic Green function series defined for all (X,Y,Z) outside the periodic shifted-pole lattice

$$P_j^{qper} = \{(X,Y,Z)\in\mathbb{R}^3 : (X,Y,Z) = (nd_1, md_2, -sh) \text{ for some } n,m\in\mathbb{Z} \text{ with } 1\leq s\leq j\}. \tag{4.1.10}$$

The proposed algorithm also utilizes the spectral representation of the quasi-periodic Green function

$$\tilde{G}^{qper}(X,Y,Z) = \frac{i}{2d_1d_2}\sum_{n,m}\frac{1}{\gamma_{nm}} e^{i(\alpha_n X+\beta_m Y+\gamma_{nm}|Z|)}, \tag{4.1.11}$$

as well as the corresponding shifted version:

$$\tilde{G}_j^{qper}(X,Y,Z) = \frac{i}{2d_1d_2}\sum_{n,m}\frac{(1-e^{i\gamma_{nm}h})^j}{\gamma_{nm}} e^{i\omega_{nm}\cdot(X,Y,Z)}, \quad \text{for} \quad Z>0. \tag{4.1.12}$$

4.1.2 Perfectly conducting case: integral equations

A variety of integral equations for problems of scattering under the perfect-conductor boundary conditions

$$\nu\times E^{tot} = 0 \qquad \text{on } \Gamma, \tag{4.1.13}$$

exist, including those arising from the direct method (which, based on the Stratton–Chu representation formulas [74], express the scattered fields in terms of the physical surface current), as well as those arising from the indirect method (that relies on an integral representation based on a non-physical surface density). Reference [60] provides an extensive discussion of integral representations for electromagnetic problems. In the proposed approach, we will rely in the so-called "indirect MFIE" (Magnetic Field Integral Equation) which follows from a representation of the field given by the operator

$$\nabla\times\int_\Gamma G(\mathbf{x}-\mathbf{y})a(\mathbf{y})d\sigma(\mathbf{y}), \tag{4.1.14}$$

where the density a is a vector field that is tangential to the scattering surface Γ ($\nu(\mathbf{y})\cdot a(\mathbf{y})=0$).

In the present shifted-Green-function treatment of the quasi-periodic problem, however, such a formulation would give rise to a non-trivial null-space in the resulting integral equation system. As mentioned in Section 2.3.1, a possible solution lies in re-incorporating the modes deleted as a result of the shifting approach. This can be accomplished by utilizing the following "complete" Green Function

$$G_j^{qper} = \tilde{G}_j^{qper} + \sum_{n,m \in U^\eta} e^{i\omega_{nm}} \tag{4.1.15}$$

where

$$U^\eta = \left\{ n \in \mathbb{Z} : |(1 - e^{\mathrm{i}\beta_n h})^j \beta_n^{-1}| < \eta \right\} \tag{4.1.16}$$

which leads to the alternative representation

$$E^{scat}(\mathbf{x}) = \nabla \times \int_\Gamma \left(G_j^{qper}(\mathbf{x} - \mathbf{y}) \cdot (\mathbf{x} - \mathbf{y}) \right) a(\mathbf{y}) d\sigma(\mathbf{y}) \tag{4.1.17}$$

of the electric field, where the density a is, once again, a tangential vector field. Applying the boundary conditions (4.1.13) to the representation (4.1.17) we obtain the vector integral equation

$$\frac{a(\mathbf{x})}{2} - \mathcal{K}[a] = -\nu \times E^{inc} \tag{4.1.18}$$

where letting

$$\tilde{\mathcal{K}}[a](\mathbf{x}) = \nu(\mathbf{x}) \times \int_\Gamma \nabla_y \tilde{G}_j^{qper}(\mathbf{x} - \mathbf{y}) \times a(\mathbf{y}) d\sigma(\mathbf{y}) \tag{4.1.19}$$

and

$$\mathcal{K}^M[a](\mathbf{x}) = \nu(\mathbf{x}) \times \sum_{(n,m) \in U^\eta} \int_\Gamma i e^{i\omega_{nm} \cdot (\mathbf{x} - \mathbf{y})} \left(\omega_{\mathbf{nm}} \times a(\mathbf{y}) \right) d\sigma(\mathbf{y}), \tag{4.1.20}$$

we have set

$$\mathcal{K} = \tilde{\mathcal{K}}[a](\mathbf{x}) - \mathcal{K}^M[a](\mathbf{x}). \tag{4.1.21}$$

Clearly $\mathcal{K}^{\mathcal{M}}$ is a finite rank operator, and the operators $\tilde{\mathcal{K}}$ and $\mathcal{K}^{\mathcal{M}}$ (and, thus, $\mathcal{K}$) map tangential vector fields into tangential fields. In view of the condition $\nu(\mathbf{y}) \cdot a(\mathbf{y}) = 0$ and the well known vector identity $a \times (b \times c) = (a \cdot c)b - (a \cdot b)c$, equation (4.1.19) can easily be recast in the form

$$\tilde{\mathcal{K}}[a](\mathbf{x}) = \int_\Gamma \left((\nu(\mathbf{x}) - \nu(\mathbf{y})) \cdot a(\mathbf{y}) \nabla_y \tilde{G}_j^{qper}(\mathbf{x} - \mathbf{y}) + \frac{\partial \tilde{G}_j^{qper}(\mathbf{x} - \mathbf{y})}{\partial n_x} a(\mathbf{y}) \right) d\sigma(\mathbf{y}), \tag{4.1.22}$$

whose kernel is weakly singular.

4.1.3 Evaluation of the Rayleigh Expansion

After solving equation (4.1.18) for a, in order to obtain the coefficients B_{nm} of the expansion (4.1.6), we first replace (4.1.12) in equation (4.1.17), to obtain

$$E_{per}^{scat}(\mathbf{x}) = \sum_{n,m} \left(\frac{i}{2d_1 d_2} \frac{(1 - e^{i\gamma_{nm} h})^j}{\gamma_{nm}} + \mathbb{I}_{\{(n,m) \in U^\eta\}} \right) \nabla \times \int_\Gamma e^{i\omega_{nm} \cdot (\mathbf{x} - \mathbf{y})} a(\mathbf{y}) d\sigma(\mathbf{y}). \tag{4.1.23}$$

For notational convenience, we define the vector $\mathbf{A_{nm}} = (A^{(1)}_{nm}, A^{(2)}_{nm}, A^{(3)}_{nm})$ by

$$A^{(j)}_{nm} = \int_{\Gamma} e^{-\mathrm{i}\omega_{nm}\cdot\mathbf{y}} a^{(j)} d\sigma(\mathbf{y}), \tag{4.1.24}$$

which, upon replacement in (4.1.23) and after applying the curl operator, leads to

$$E^{scat}_{per}(\mathbf{x}) = \sum_{n,m} \left(\frac{-1}{2d_1 d_2} \frac{(1 - e^{\mathrm{i}\gamma_{nm}h})^j}{\gamma_{nm}} + \mathrm{i}\chi_{\eta,n,m} \right) (\omega_{\mathbf{nm}} \times \mathbf{A}) e^{i\omega_{\mathbf{nm}}\cdot\mathbf{x}}. \tag{4.1.25}$$

where

$$\chi_{\eta,n,m} = \begin{cases} 1 & \text{for } (n,m) \in U^{\eta} \\ 0 & \text{otherwise.} \end{cases}$$

Finally, equating the right hand side of this expression with the right hand side of (4.1.6), by orthogonality of the Rayleigh modes in the plane $\mathbf{x} = (x_1, x_2, 0)$, we obtain an expression for each of the Rayleigh coefficients B_{nm} of the expansion (4.1.6):

$$B_{nm} = \left(\frac{-1}{2d_1 d_2} \frac{(1 - e^{\mathrm{i}\gamma_{nm}h})^j}{\gamma_{nm}} + \mathrm{i}\chi_{\eta,n,m} \right) (\omega_{\mathbf{nm}} \times \mathbf{A}). \tag{4.1.26}$$

4.2 Outline of the Proposed Nyström Solver

4.2.1 Basic algorithmic structure

In order to obtain numerical solutions of the surface integral equations (4.1.18) we utilize a Nyström discretization strategy which is based on the recently introduced singular quadrilateral integration [16], a version of which is described in what follows.

This algorithm relies on

1. A discrete set of nodes $\{r_i : 1 \leq i \leq N\}$ on the surface which are used for both interpolation into (finer) integration grids (Section4.2.3), and collocation.

2. High-order integration rules which, using a given discrete set $\{a(x_i) : 1 \leq i \leq N\}$ of accurate approximate values of a smooth surface density a, produce accurate approximations of the quantities $\mathcal{K}[a](x_i)$ $(1 \leq i \leq N)$ in equations (4.1.21) and (4.1.22).

3. (Accelerated version only). A three-dimensional version of the acceleration strategy introduced in Chapter 2.

4. The iterative linear algebra solver GMRES.

Once a solution is obtained, the Rayleigh expansion of the solution is evaluated and the diffraction efficiencies are reported.

4.2.2 Patch partitioning and Chebyshev-Nyström discretization

As a first step in the algorithm, we require that the specified geometry be expressed as a union of curved quadrilaterals (an industry standard which is ubiquitous in commercial and non-commercial CAD-representation methods), each one of which is mapped from a reference square domain. That is to say, the discretization strategy relies on use of a set of non-overlapping local parametrizations

$$\gamma_p : [-1,1]^2 \to \Gamma \subset \mathbb{R}^3 \qquad p = 1, \cdots, n_p, \tag{4.2.1}$$

of the surface Γ. We will further assume that the specified geometries are sufficiently smooth (i.e. do not contain corners or edges), but the methodology can be easily extended to enable treatment of domains containing corners and/or edges [16].

Each of the curved quadrilaterals is discretized by employing a corresponding discretization of the reference square. In order to do this, we employ the two-dimensional tensor product of one-dimensional Fejer's type I quadrature in an interval, (also called "open Chebyshev" quadrature, since the nodes it utilizes, which are given by explicit expressions, do not contain the interval endpoints). The corresponding quadrature weights can be computed efficiently (by means of the FFT algorithm) as detailed in [79]. The patch-partitioning and Chebyshev discretization is depicted, for the case of a sphere, in Figure 4.2.1.

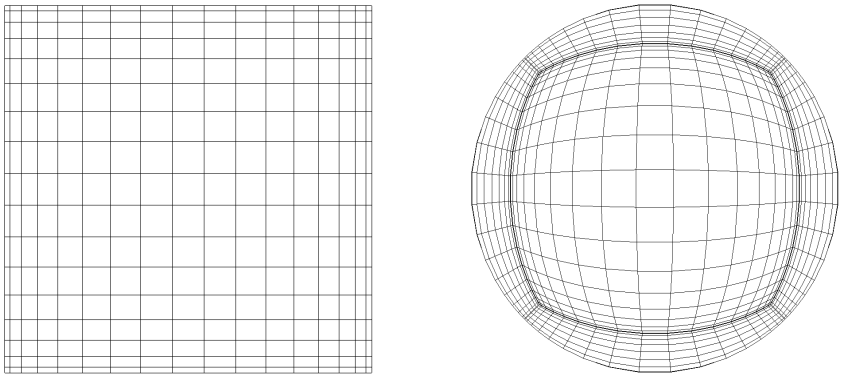

(a) (b)

Figure 4.2.1: (a) Chebyshev points in a reference square domain. (b) 6-patch mesh of the sphere.

4.2.3 High-order singular quadrature

This section outlines the singular quadrature Nyström approach we will use. The section proceeds by considering examples of increasing complexity for the case of bounded scatterers, and illustrates the properties of the proposed approach with numerical examples. Finally, a discussion of the computational cost of the singular (and near-singular) integration problems we require is included.

A simple integration example

As our first example of the integration problems that require treatment in order to implement discrete versions of operators such as (4.1.22), we consider the following integral, that corresponds to an acoustic single layer operator in the rectangular flat patch $(-1,1)\times(-1,1)\times\{0\}$, in which the integrand contains a singularity that lies at the point $(u',v')=(u,v)$,

$$f_{\rm k}(u,v)=\int_{-1}^{1}\int_{-1}^{1}\frac{e^{{\rm i}{\rm k}\sqrt{(u-u')^2+(v-v')^2)}}}{\sqrt{(u-u')^2+(v-v')^2}}du'dv' \tag{4.2.2}$$

In the case $|u|,|v|>>1$ the resulting integral is regular, and thus, the Fejer quadrature weights provide an accurate integration method. In the case $(u,v)\in(-1,1)\times(-1,1)$ the integral is singular, and when (u,v) is sufficiently close to $(-1,1)\times(-1,1)$, the integral is said to be near-singular.

For both singular and near-singular integration problems, the method for singular integration that we use relies on the polynomial change of variables.

$$\left\{\begin{array}{ll} u'= & u+t^\tau \\ v'= & v+s^\tau \end{array}\right. \quad \text{with derivatives} \quad \left\{\begin{array}{ll} du'/dt= & \tau t^{\tau-1} \\ dv'/ds= & \tau s^{\tau-1}m \end{array}\right. \tag{4.2.3}$$

which clusters the mesh around the point (u,v). The resulting "vanishing" Jacobian derivatives provide additional degrees of integrand regularity around $(t,s)=(0,0)$. Applying the polynomial change of variables (4.2.3) to equation (4.2.2), we obtain the smooth integrand

$$f_{\rm k}(u,v)=\tau^2\int_{t_a}^{t_b}\int_{s_a}^{s_b}\frac{e^{{\rm i}{\rm k}\sqrt{t^{2\tau}+s^{2\tau}}}}{\sqrt{t^{2\tau}+s^{2\tau}}}t^{\tau-1}s^{\tau-1}dsdt, \tag{4.2.4}$$

where the corresponding integration boundaries are given by

$$\left\{\begin{array}{ll} t_a= & |-1-u|^{\frac{1}{\tau}}{\rm sgn}(-1-u) \\ t_b= & |1-u|^{\frac{1}{\tau}}{\rm sgn}(-1-u) \end{array}\right. \quad \left\{\begin{array}{ll} s_a= & |-1-v|^{\frac{1}{\tau}}{\rm sgn}(-1-v) \\ s_b= & |1-v|^{\frac{1}{\tau}}{\rm sgn}(1-v). \end{array}\right. \tag{4.2.5}$$

To compute this smooth integration problem, we resport to an m-point Fejer quadrature rule along each variable t and s. That is, we employ the approximation

$$f_{\rm k}(u,v)\approx\tau^2\sum_{i=1}^{m}\sum_{j=1}^{m}\frac{e^{{\rm i}{\rm k}\sqrt{t_i^{2\tau}+s_j^{2\tau}}}}{\sqrt{t_i^{2\tau}+s_j^{2\tau}}}t_i^{\tau-1}s_j^{\tau-1}w_iw_j, \tag{4.2.6}$$

where $\{t_i,w_i:1\le i\le m\}$ and $\{s_j,w_j:1\le j\le m\}$ are sets of Fejer quadrature nodes and weights of the interval (t_a,t_b) and (s_a,s_b), respectively. Table 4.2.1 below displays the accuracies obtained for various values of τ and m.

Example 2: Discretization of the Single-Layer operator in the sphere

This section demonstrates the quadrilateral integration strategy we use, for the simplest scattering integral operator, namely, the single layer potential (1.1.28) for a bounded scatterer, and it demonstrates its performance for the simplest three-dimensional scatterer: the sphere.

	Integration of $f_0(0,0)$			Integration of $f_\pi(0,0)$		
m	$\tau = 7$	$\tau = 9$	$\tau = 11$	$\tau = 7$	$\tau = 9$	$\tau = 11$
20	3.8e-04	4.3e-04	5.5e-04	6.7e-04	6.3e-04	7.2e-04
40	7.4e-06	5.6e-06	5.9e-06	1.4e-05	1.0e-05	1.1e-05
60	5.6e-07	2.8e-07	2.2e-07	1.0e-06	5.1e-07	4.1e-07
80	8.3e-08	2.8e-08	1.7e-08	1.5e-07	5.1e-08	3.1e-08
100	1.8e-08	4.3e-09	2.0e-09	3.4e-08	8.0e-09	3.8e-09
120	5.3e-09	9.2e-10	3.3e-10	9.8e-09	1.7e-09	6.2e-10

Table 4.2.1: Example integration of $f_0(0,0)$ and $f_\pi(0,0)$. In the first case, an existing closed form expression is used for error evaluation, while in the second case, which corresponds to a patch of one wavelength in size, a numerical reference solution is used instead.

Given discrete values $\phi(\mathbf{r}_{ij}^p)$ for $1 \leq i,j \leq n$ at points $\mathbf{r}_{ij}^p \in \Gamma$

$$\mathbf{r}_{ij}^p = \gamma_p(u_i, v_j) \tag{4.2.7}$$

on the p-th patch, the discrete forward map provides an approximation of the quantities

$$S[\phi](\mathbf{r}_{ij}^p) = \sum_{p'=0}^{n_p} \int_{-1}^{1}\int_{-1}^{1} G(\mathbf{r}_{ij}^p, \gamma_{p'}(u',v'))\phi(u',v')J_{p'}(u',v')du'dv' \tag{4.2.8}$$

where $J_{p'}(u',v')du'dv'$ denotes the area element of the underlying surface parametrization at the point (u',v') of the integration patch p'.

Note that, as is customary in the Nyström discretization approach, the function ϕ is only known at a discrete set of points. In order to produce the desired integrals, the proposed approach combines a Chebyshev interpolation strategy with the singular (or regular) integration strategy described in the previous example. A way of producing this discrete forward-map, follows by specifying the values of the linear function

$$\phi(\mathbf{r}_{ij,p}^p) \to S[\phi](\mathbf{r}_{ij,p}^p) \tag{4.2.9}$$

in a 2D-Chebyshev basis. For that reason, we consider density functions $\phi_{ij}(u,v) = T_i(u)T_j(v)$, where T_i is the Chebyshev polynomial of order i, and we thus compute the integrals

$$S[\phi_{ij}](\mathbf{r}_{ij,p}^p) = \sum_{p'=0}^{n_p} \int_{-1}^{1}\int_{-1}^{1} G(\mathbf{r}_{ij}^p, \gamma_{p'}(u',v'))T_i(u')T_j(v')J_{p'}(u',v')du'dv' \tag{4.2.10}$$

by the proposed change-of-variables clustered-grid approach.

The algorithm proceeds by finding the closest point in the integration patch p' to the observation point $\mathbf{r}_{ij}^p$, namely

$$(u_\star^{p'}, v_\star^{p'}) = \underset{(u',v')}{\arg\min} \|\gamma_{p'}(u',v') - \mathbf{r}_{ij}^p\|, \tag{4.2.11}$$

around of which the integration grid is clustered. In the case that the observation point is contained within the integration patch, $(u_\star^{p'}, v_\star^{p'})$ coincides with the coordinates of the observation

point. Otherwise, the point $(u_\star^{p'}, v_\star^{p'})$ could be sufficiently close to the observation point, and then the grid-clustering described in the previous section could be beneficial in dealing with a near-singular integration problem. For conciseness, this section restricts attention to the most demanding algorithm—which treats all integrals as either singular or near/singular, whereas an optimized version, that determines if the clustering procedure is convenient or not, is used later in this Chapter.

Applying the change of variables (4.2.3) with $u = u_\star^{p'}$ and $v = v_\star^{p'}$, we obtain

$$S[\phi](\mathbf{r}_{ij}^p) = \tau^2 \sum_{p'=0}^{n_p} \int_{t_a}^{t_b} \int_{s_a}^{s_b} G(\mathbf{r}_{ij}^p, \gamma_{p'}(u_\star^{p'}+t^\tau, v_\star^{p'}+s^\tau)) T_i(u_\star^{p'}+t^\tau) T_j(v_\star^{p'}+s^\tau) J_{p'}(u_\star^{p'}+t^\tau, v_\star^{p'}+s^\tau) s^{\tau-1} t^{\tau-1} ds dt. \tag{4.2.12}$$

Using the Fejer quadrature rule of m points in each of the variables s and t, and denoting $r'_{k\ell} = \gamma_{p'}(u_\star^{p'} + t_k^\tau, v_\star^{p'} + s_\ell^\tau)$, we then obtain

$$S[\phi](\mathbf{r}_{ij}^p) \approx \tau^2 \sum_{p'=0}^{n_p} \sum_{k=1}^{m} \sum_{\ell=1}^{m} G(\mathbf{r}_{ij}^p, r'_{k\ell}) T_i(u_\star^{p'} + t_k^\tau) T_j(v_\star^{p'} + s_\ell^\tau) J_{p'}(u_\star^{p'} + t_k^\tau, v_\star^{p'} + s_\ell^\tau) s_\ell^{\tau-1} t_k^{\tau-1}. \tag{4.2.13}$$

which provide the desired approximation.

As is known [29], the spherical harmonics Y_ℓ^m are eigenfunctions, with known eigenvalues, of the relevant integral operators we consider in this thesis, which provides a natural test case for out implementation of the singular quadrature routine. Figure 4.2.2 and Table 4.2.2 below demonstrate the accuracies obtained as the proposed discrete quadrature is applied to approximate the forward map $S[Y_5^2](r)$ on the six-patch discretization, depicted in Figure 4.2.1(b), of the sphere of radius 2.707λ.

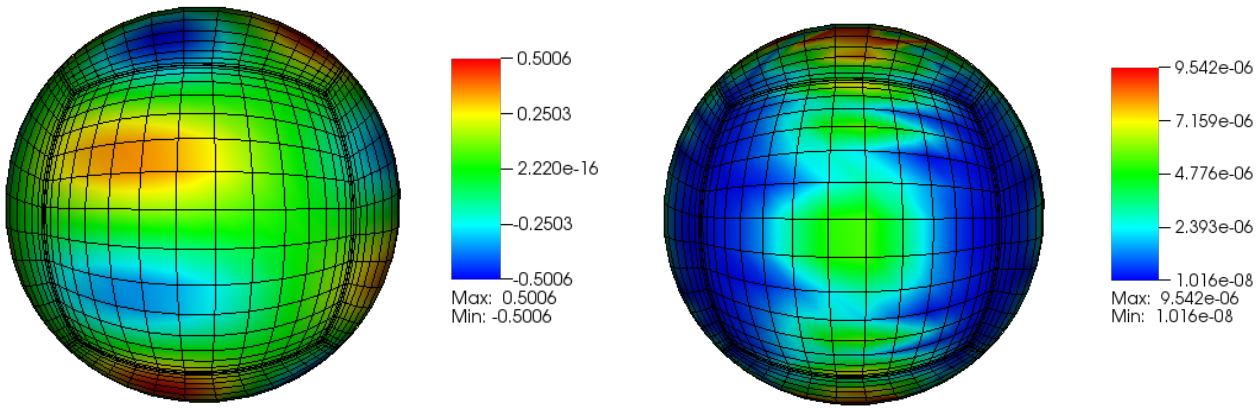

(a) (b)

Figure 4.2.2: (a) Spherical harmonic density Y_5^2 over the surface of a sphere, (b) Errors in the approximation of $S[Y_5^2]$

Computing cost

Regarding the computing cost of this simplified (all-singular) approach, it is clear that the evaluation of the discrete operator $S[\phi](\mathbf{r}_{ij}^p)$ $(1 \le i, j \le n)$ in (4.2.13) requires

n	m	Total unknowns	Max rel error in $S[Y_5^2]$	Time (sec)
8	40	$8 \times 8 \times 6$	2.92e-02	0.30
12	60	$12 \times 12 \times 6$	1.76e-03	1.53
16	80	$16 \times 16 \times 6$	6.38e-05	4.8
20	100	$20 \times 20 \times 6$	1.27e-06	12.4
24	120	$24 \times 24 \times 6$	9.77e-08	25.8

Table 4.2.2: The discrete forward map $\phi(\mathbf{r}_{ij}^p) \to S[\phi](\mathbf{r}_{ij}^p)$ applied to $\phi = Y_5^2$.

1. A number n^2m^2 of evaluations of exponentials and surface area element functions.

2. For each pair (i, j) a double sum over the indexes (k, ℓ).

The last operation, however, can be performed in $O(n^2m)$ operations, by precomputing the inner sum in (4.2.13), for each k. The overall cost, however, is still $O(n^2m^2)$ in virtue of the evaluation of the required exponential functions at all pairs $(\mathbf{r}_{ij,p}^p, r'_{k\ell})$, and the evaluation of surface area elements in all clustered grids. In practice, values of n and m such as $n = 16$ and $m = 80$ are used for each patch, which provide a sufficiently high order of convergence: whenever more discretization and/or integration points are required, either higher values of n, m can be considered, or certain patches in the geometry can be partitioned into two or more patches, as convenient, to ensure high-order convergence while maintaining a cost effective overall algorithm.

4.3 Unaccelerated Nyström solver applicable at Wood Anomalies

The discretization strategy for the operator $\tilde{\mathcal{K}}$ in (4.1.22) relies on both the spatial and spectral representations of the quasi-periodic Green function G_j^{qper}. As was done in Section 2.4.2 for the operator $\tilde{D}$, the contributions to the integral operator $\mathcal{K}(\mathbf{x})$ are divided, for each $\mathbf{x}$, in singular/near-singular interactions (patches which are close to $\mathbf{x}$) and regular interactions (patches that are far from $\mathbf{x}$); the former ones are evaluated by means of the algorithm described in the previous section, while the latter ones are treated directly by means of Fejer's quadrature, without resorting to changes of variables and/or oversampling.

As we will only evaluate $\mathcal{K}(\mathbf{x})$ for points $\mathbf{x}$ in a periodicity cell, the regular integration arises from an infinite number of patches: expressing such series in terms of the quasi-periodic Green function, which can be evaluated by resorting to its spectral representation, leads to reduced computational costs. The following expression, which follows directly from (4.1.12),

$$\nabla_x \tilde{G}_{per}^j(\mathbf{x}) = \frac{-1}{2d_1d_2} \sum_{n,m} \sum_{s=0}^{j} \frac{C_s^j}{\gamma_{nm}} e^{i(\alpha_n x_1 + \beta_m x_2 + \gamma_{nm}|x_3+sh|)} \left(\alpha_n, \beta_m, \text{sign}(x_3 + sh)\gamma_{nm}\right) \tag{4.3.1}$$

is exponentially convergent for $x_3 + sh$ away from zero for $s = 0, \ldots, j$.

4.3.1 Unaccelerated Wood-capable solver: Numerical results

The following table presents solver statistics for a bisinusoidal surface

$$\Gamma = \{(u, v, f(\mathbf{x}, y)); u, v \in \mathbb{R}\} \qquad \text{with} \qquad f(u, v) = \frac{H}{4}\left(\cos(2\pi u) + \cos(2\pi v)\right) \tag{4.3.2}$$

illuminated at an angle $\phi = 20^\circ$ and using the Wood-frequency $k = 4.78$. The peak-to-peak height H is set to $H = 0.5$. The number of shifts $j = 6$ was used in all cases.

N	n_{per}	Cons. error ε ($\delta = 0^\circ$)	Cons. error ε ($\delta = 90^\circ$)
10×10	25	8.26e-03	7.87e-02
12×12	30	3.88e-03	3.39e-03
14×14	40	3.54e-03	2.534e-03
16×16	100	1.61e-03	2.431e-03
18×18	125	4.11e-04	5.53e-04

Table 4.3.1: Convergence of unaccelerated solver at a Wood-frequency. See Section 4.4 for corresponding performance data on accelerated solutions.

4.4 Accelerated Nyström solver applicable at Wood Anomalies

4.4.1 Shifted equivalent sources and FFT acceleration in three dimensions

One of the most important aspects of the acceleration strategy of Chapter 2 is its direct extensibility to three-dimensional problems. This section presents a brief outline of the three-dimensional version of the acceleration strategy, which closely follows that presented in Chapter 2.

The equivalent source representation involves three sets of parallel faces of a cube; one of such pairs is depicted in Figure 4.4.1 below together with the corresponding set of collocation points, which are the three-dimensional analogs of the two-dimensional set $\{x_t^q\}$ of collocation points used in equation (2.5.8). We also note that, in order to accelerate the operator $\tilde{\mathcal{K}}$ in (4.1.19), the cross product in the integrand of (4.1.19),

$$\nabla_y \tilde{G}_j^{qper}(\mathbf{x} - \mathbf{y}) \times a(\mathbf{y}) = \varepsilon_{ijk} \frac{\partial \tilde{G}_j^{qper}}{\partial y_j}(\mathbf{x} - \mathbf{y}) a_k(\mathbf{y}) \tag{4.4.1}$$

leads to a six scalar soulutions of the Helmholtz equation with respect to x. The equivalent-source scalar-representation of the form (2.5.7) is applied to each of these components. After solving the corresponding least squares problems, the equivalent sources are merged into local and global convolution grids, and the necessary convolutions are performed as in Section 2.5.5. Finally, the plane wave expansion method is completely analogous to that in Section 2.5.6. With the various elements in hand, routines that apply the corresponding forward map in a reduced computational cost are obtained.

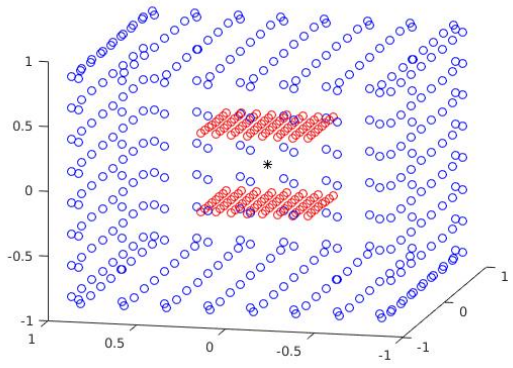

Figure 4.4.1: Equivalent Sources: geometric setup.

4.4.2 Accelerated Wood-capable solver: Numerical Results

Table 4.4.1 presents solver statistics for the scattering of a bi-sinusoidal perfectly conducting surface considered in Section 4.3.1 at the Wood-frequency $k = 4.78$. The table includes timings resulting from use of both the accelerated and unaccelerated solver. The errors produced by the two solvers coincide, and the marked improvements in computing times resulting from use of the acceleration procedure are clearly demonstrated by the timings provided in the table.

N	n_{per}	Energy Error ε	Unaccel. time (sec)	Accel. Time (sec)
10×10	50	1.1e-01	22.4	10.5
12×12	60	3.3e-02	132.2	13.2
14×14	75	7.0e-03	165.5	20.5
16×16	100	2.9e-03	443.2	34.4
18×18	125	3.9e-05	1099.8	59.3

Table 4.4.1: Solver statistics for the accelerated and un-accelerated solvers at a Wood-frequency.

Figure 4.4.2 displays a physically observable quantity, namely, the scattered energy in the specular direction, as a function of the frequency of the problem—including points around Wood Anomaly frequencies.

As a demonstration of the applicability of the proposed algorithm for more general geometries, Figure 4.4.3 displays the solution density for a problem containing surfaces and particles. Using $N = 1200$, $j = 4$, $n_{\text{per}} = 50$ the solver produced the scattered field with an energy-balance error $\varepsilon = 4.23e-04$ using 177 GMRES iterations in a total computational time of 232 seconds in a single core of an 3.4GHz Intel i7-6700 processor with 4 Gb of memory.

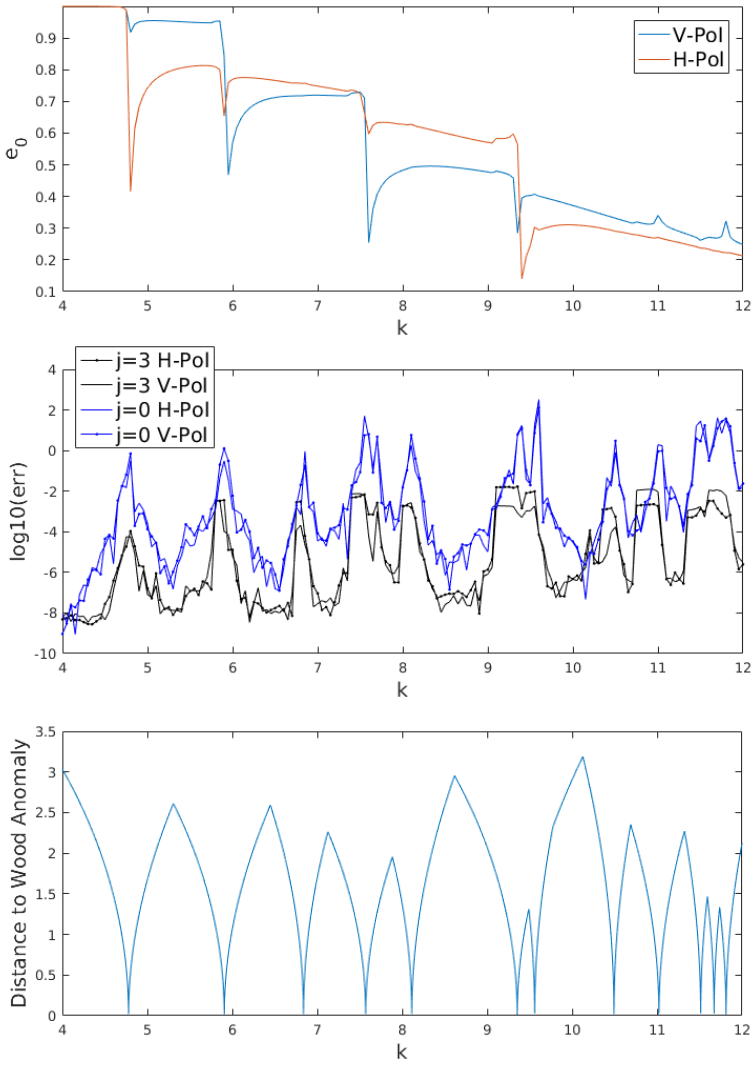

Figure 4.4.2: Energy scattered in the specular direction, HH and VV cases . Sharp drops indicate a Wood anomaly frequency.

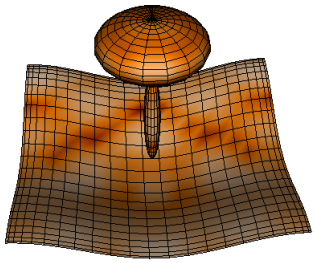

Figure 4.4.3: Solution density in the periodicity cell

Chapter 5

Related contributions and future work

The topics presented in this thesis have given rise to a number of collaborations, some of which have extended into long-term efforts concerning significant applications. These collaborative efforts and related future mathematical work are described in what follows.

5.1 Non-Rayleigh anomalies in remote sensing

The electromagnetic scattering from rough surfaces, such as agricultural soils or the surface of the ocean, is of considerable interest in radar remote sensing applications. Historically, studies of scattering from ocean surfaces has been linked to periodic surfaces. For example, Crombie [32] identified backscattering from the sea with that produced by diffraction gratings. Similarly, the Bragg resonance condition derived by Wright [81] is equivalent for a periodic surface to produce backscattering returns. Periodic and randomly perturbed periodic surfaces have been considered as well for the case of agricultural soils [77, 84], specially to consider the effect of the tilling structure.

More recently, the increased availability of polarization discriminate radar data has drawn the attention to a very peculiar feature. Namely, it has been observed in both ocean and agricultural surfaces, that radar cross sections for HH polatizations can exceed radar cross sections for VV polarizations. Regarding ocean surfaces, rigorous electromagnetic computations on wave pulse profiles have been shown in [71] to give rise to HH/VV ratios larger than 1, with values consistent with those observed experimentally, as a result of strong scattering anomalies. The case of agricultural surfaces, in turn, is much less explored. The radar data displayed in Figure 5.1, suggests that, for bare agricultural soils (without vegetation) HH/VV ratios are a common phenomena in C-Band, and less common in L-band.

This fact contradicts existing solutions based on Gaussian surfaces or the like, whether numerical or approximate methods are used. Empirical methods such as [63] have also reproduced this predicted theoretical behavior. These unexpected behauviour could be justified on the basis of subsurface effects such as the layered structure of the soil or particulate scattering within it, or

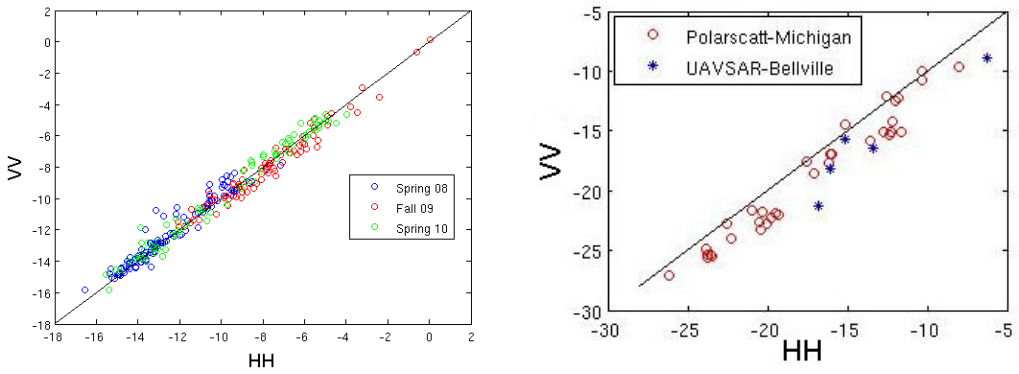

Figure 5.1.1: Radar data of agricultural surfaces. Left: RadarSAT-2 Casselman Campaign (C-Band) in Canada [59], Right: L-Band Data from UAVSAR and SARAT over the Pampas Region

the effect of mild vegetation such as the residue cover. On the other hand, the numerical methods developed in this thesis show that such anomalies can arise due to surface scattering only, if the geometry of a tilled soil is properly taken into account. In fact, the numerical methods developed in the present thesis enables computation of scattering of surface geometries that adequately capture the various scales present in agricultural soils, and is efficient even in the case when the height of the surface is comparable or larger than the incident wavelength. It is precisely this kind of resonant geometries which are away from the validity range of usual approximations—and also beyond the grasp of most of the existing numerical methods—that can give rise to "polarization anomalies".

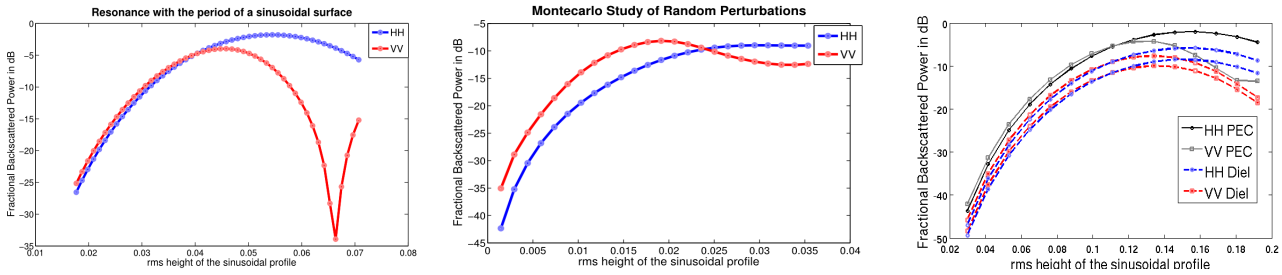

(a) (b) (c)

Figure 5.1.2: (a) Simulations of the scattering from a sinusoidal surface (Period=80cm, λ =25cm), (b) montecarlo study of random perturbations (c) Effect of dielectric constant

Figure 5.1.2 shows that the often overlooked surface-scattering mechanism of the VV-resonance with the tilling period can have an important effect on the polarization ratio. In particular, Figure 5.1.2(a) displays the backscattering intensity from a sinusoidal geometry of a fixed period and increasing height, which gives rise to a strong resonance in VV. Figure 5.1.2(b) show that this effect persists under random perturbations of the surface, and Figure 5.1.2(c) studies the effect of dielectric constants in the order or $\epsilon = 4 - 20$ for large sinusoidal profiles in L band, and shows that

the same behauviour holds throughout the whole range of dielectric constants.

5.2 Transmission problems

The methods presented in this thesis are directly applicable to more general boundary conditions. In fact, a closed-surface version of the algorithm proposed in Chapter 4 have already been applied to the study of sonar backscattering of fish swimbladders of arbitrary three-dimensional shapes in the collaboration [40]. That collaboration involved the solution of the transmission problem detailed in Section 5.2.1, and the implementation of the integral equation operators mentioned in Section 1.1.4, as well as the so-called Muller integral operator, which is described in Section 5.2.1. The implementation of the corresponding operators for electromagnetic transmission problems, described in Section 5.2.2 are a subject of ongoing/future work.

5.2.1 Acoustic transmission

In the transmission problem, two functions u_1, u_2 satisfying Helmholtz equation in a domain D and its complement D^c, with wavenumbers k_1 and k_2 respectively, radiation boundary conditions in $\pm\infty$ and the following boundary conditions in ∂D:

$$\left\{ \begin{array}{cc} u_1 - u_2 & = f \\ \mu_1 \frac{\partial}{\partial n} u_1 - \mu_2 \frac{\partial}{\partial n} u_2 & = g \end{array} \right. \tag{5.2.1}$$

where usually f represents an incident plane-wave: $f = e^{i\hat{k}\cdot\mathbf{x}}$, $g = \frac{\partial}{\partial n} f$.

We represent the solutions as combined potential with constants d_1, d_2, s_1, s_2 to be chosen conveniently.

$$\left\{ \begin{array}{lll} u_1 = & d_1 D_{k_1}(\psi) + s_1 S_{k_1}(\phi) & \text{in } D \\ u_2 = & d_2 D_{k_2}(\psi) + s_2 S_{k_2}(\phi) & \text{in } D^c \end{array} \right. \tag{5.2.2}$$

Replacing (5.2.2) in (5.2.1) and applying the corresponding jump conditions [60], we obtain the equation system

$$\left\{ \begin{array}{cc} \frac{1}{2}(d_1 + d_2)\psi + (d_1 D_{k_1} - d_2 D_{k_2})\psi + (s_1 S_{k_1} - s_2 S_{k_2})\phi & = f \\ -\frac{1}{2}(\mu_1 s_1 + \mu_2 s_2)\phi + (\mu_1 d_1 \mathcal{N}_{k_1} + \mu_2 d_2 \mathcal{N}_{k_2})\psi + (\mu_1 s_1 K'_{k_1} - \mu_2 s_2 K'_{k_2})\phi & = g \end{array} \right. \tag{5.2.3}$$

where we denote

$$K'_k = \frac{\partial}{\partial n_r} S_k \tag{5.2.4}$$

$$\mathcal{N}_k = \frac{\partial}{\partial n_r} D_k \tag{5.2.5}$$

Importantly, the operator $\mathcal{N}_k$ is hypersingular. Choosing $d_1 = \frac{1}{\mu_1}, d_2 = \frac{1}{\mu_2}$, however, leads to the difference $\mathcal{N}_{k_1} - \mathcal{N}_{k_2}$, which is known as the Muller operator and is weakly integrable, as shown in the next section.

In order to reach a succinct expression, we also choose $s_1 = \frac{1}{\mu_1^2}, s_2 = \frac{1}{\mu_2^2}$. Now, defining

$$A := \begin{bmatrix} -(\mu_1^{-1} D_{k_1} - \mu_2^{-1} D_{k_2}) & -(\mu_1^{-2} S_{k_1} - \mu_2^{-2} S_{k_2}) \\ (T_{k_1} - T_{k_2}) & (\mu_1^{-1} K'_{k_1} - \mu_2^{-1} K'_{k_2}) \end{bmatrix} \qquad \chi = \begin{pmatrix} \psi \\ \phi \end{pmatrix} \qquad h = \begin{pmatrix} f \\ -g \end{pmatrix}$$

We have the system of equations, which are known as "Muller's equations".

$$\frac{1}{2}\left(\frac{1}{\mu_1} + \frac{1}{\mu_2}\right)\chi - A\chi = h \tag{5.2.6}$$

Acoustic Muller operators

As shown above, Muller's equations require the implementation of the following integral operators: Single Layer, Double Layer, Normal-Derivative-Single-Layer and the so-called Muller operator (the difference of two hypersingular operators). In what follows we describe the implementation of the Muller operator

$$\mathcal{M}_{k_1 k_2} = \mathcal{N}_{k_1} - \mathcal{N}_{k_2}, \tag{5.2.7}$$

which contains, as we shall see, a weakly integrable kernel, and where the hypersingular operator $\mathcal{N}_k$ is given by

$$\mathcal{N}_k \phi = PV \int_\Gamma \frac{\partial^2}{\partial n_r \partial n_{r'}} G_k(r - r')\phi(r') dS' \tag{5.2.8}$$

We compute the double normal derivative $\frac{\partial^2}{\partial n_r \partial n_{r'}} \left(G_{k_1} - G_{k_2}\right)(R)$. We start with

$$\frac{\partial^2}{\partial n_r \partial n_{r'}}\left(\frac{e^{ikR}}{R}\right) = \frac{\partial}{\partial n_r}\left[\nabla^{r'}\left(\frac{e^{ikR}}{R}\right) \cdot n_{r'}\right] \tag{5.2.9}$$

$$= \frac{\partial}{\partial n_r}\left[\left(\frac{e^{ikR}}{R} - ike^{ikR}\right)\frac{\langle r - r', n_{r'}\rangle}{R^2}\right] \tag{5.2.10}$$

$$= \frac{\partial}{\partial n_r}\left[\frac{e^{ikR}}{R^3} - ik\frac{e^{ikR}}{R^2}\right]\langle r - r', n_{r'}\rangle + \left(\frac{e^{ikR}}{R^3} - ik\frac{e^{ikR}}{R^2}\right)\langle n_r, n_{r'}\rangle \tag{5.2.11}$$

We now compute the gradient

$$\nabla^r\left[\frac{e^{ikR}}{R^3} - ik\frac{e^{ikR}}{R^2}\right] = (r - r')e^{ikR}\left(\frac{ik}{R^3} - \frac{k^2 - 2}{R^4} + \frac{3ik}{R^5}\right) \tag{5.2.12}$$

$$\nabla^r\left[\frac{e^{ikR}}{R^3} - ik\frac{e^{ikR}}{R^2}\right] = (r - r')e^{ikR}\left(\frac{k^2}{R^3} + \frac{3ik}{R^4} - \frac{3}{R^5}\right) \tag{5.2.13}$$

And then

$$\frac{\partial^2}{\partial n_r \partial n_{r'}}\left(\frac{e^{ikR}}{R}\right) = e^{ikR}\left[\left(\frac{k^2}{R^3} + \frac{3ik}{R^4} - \frac{3}{R^5}\right)Q(r, r') + \left(\frac{1}{R^3} - \frac{ik}{R^2}\right)\langle n_r, n_{r'}\rangle\right] \tag{5.2.14}$$

where

$$Q(r,r') = \langle r - r', n_r \rangle \langle r - r', n_{r'} \rangle. \tag{5.2.15}$$

Given that the function $Q \sim R^4$, we observe that the above expression (5.2.14) has a singularity of order $O(R^{-3}) + O(R^{-2})$. But the Muller operator $\mathcal{M}$ involves the difference of two of such double-normal derivative operators, and it is known [60] that singularities cancel. We wish to obtain an exact expressions that captures this behavior.

Lets consider the function

$$F_k(R) = e^{ikR}\left(\frac{1}{R^3} - \frac{ik}{R^2}\right). \tag{5.2.16}$$

We want to evaluate $(F_{k_1} - F_{k_2})(R)$. For that reason, we consider the Taylor series

$$F_k(R) = \sum_{n=0}^{\infty} \frac{(ik)^n}{n!}\left(R^{(n-3)} - ikR^{(n-2)}\right). \tag{5.2.17}$$

Then,

$$(F_{k_1} - F_{k_2})(R) = \sum_{n=0}^{\infty}\left(\frac{(ik_1)^n - (ik_2)^n}{n!}R^{(n-3)} - \frac{(ik_1)^{n+1} - (ik_2)^{n+1}}{n!}R^{(n-2)}\right) \tag{5.2.18}$$

Singularities of order $O(R^{-3}) + O(R^{-2})$ are effectively cancelled, and we obtain

$$(F_{k_1} - F_{k_2})(R) = \sum_{n=2}^{\infty}\left(\frac{(ik_1)^n - (ik_2)^n}{n!}R^{(n-3)} - \frac{(ik_1)^{n+1} - (ik_2)^{n+1}}{n!}R^{(n-2)}\right) + \left(k_1^2 - k_2^2\right)R^{-1} \tag{5.2.19}$$

which gives rise to a weakly singular (integrable) kernel.

The (acoustic) Muller operator can be implemented, then, by use of the following expressions

$$\mathcal{M}_{k_1 k_2}\phi = \mathcal{M}^1_{k_1}\phi - \mathcal{M}^1_{k_2}\phi + \mathcal{M}^{\text{diff}}_{k_1,k_2}\phi \tag{5.2.20}$$

where we have defied the operators

$$\mathcal{M}^1_k\phi = \int_\Gamma e^{ikR}\left(\frac{k^2}{R^3} + \frac{3ik}{R^4} - \frac{3}{R^5}\right)\langle r - r', n_{r'}\rangle\langle r - r', n_r\rangle\phi(r')dS' \tag{5.2.21}$$

$$\mathcal{M}^{\text{diff}}_{k_1,k_2}\phi = \int_\Gamma \left(F_{k_1} - F_{k_2}\right)(R)\langle n_r, n_{r'}\rangle\phi(r')dS' \tag{5.2.22}$$

and the function

$$(F_{k_1} - F_{k_2})(R) = e^{ik_1R}\left(\frac{1}{R^3} - \frac{ik_1}{R^2}\right) - e^{ik_2R}\left(\frac{1}{R^3} - \frac{ik_2}{R^2}\right) \tag{5.2.23}$$

which, for sufficiently large R is evaluated using equation (5.2.23), and, when $R << 1$, using equation (5.2.19).

5.2.2 Electromagnetic transmission

Electromagnetic Muller operators

In the electromagnetic case, the required operators are K (MFIE) and the Electromangetic Muller operator

$$\mathcal{MT} = \nabla \times \nabla \times S_e - \nabla \times \nabla \times S_d \tag{5.2.24}$$

where the operator S_k is a vector version of the single layer operator, given by

$$S_k = \int_\Gamma G_k(r - r')\mathbf{a}(r')dS' \tag{5.2.25}$$

Algebraic manipulations similar to those of the previous section lead to

$$\nabla \times \nabla \times S_e = \int_\Gamma \left[\frac{3 - 3ikR - k^2R^2}{R^4}\mathbf{R} \times (\mathbf{R} \times \mathbf{a}) - 2\frac{ikR - 1}{R^2}\mathbf{a} \right] G_k dS' \tag{5.2.26}$$

Using the identiy

$$\mathbf{R} \times (\mathbf{R} \times \mathbf{a}) = (\mathbf{R} \cdot \mathbf{a})\mathbf{R} - (\mathbf{R} \cdot \mathbf{R})\mathbf{a}, \tag{5.2.27}$$

and defining

$$A(R) = \frac{3 - 3ikR}{R^4}(\mathbf{R} \cdot \mathbf{a})\mathbf{R} \tag{5.2.28}$$

$$B(R) = -\frac{3 - 3ikR}{R^2}\mathbf{a} \tag{5.2.29}$$

$$C(R) = \frac{2 - 2ikR}{R^2} \tag{5.2.30}$$

$$Q(R) = -\frac{k^2R^2}{R^4}(\mathbf{R} \cdot \mathbf{a})\mathbf{R} - k^2\mathbf{a} \tag{5.2.31}$$

the integrand in (5.2.26) can be expressed as $[A(R) + B(R) + C(R) + Q(R)]\, G_k$. By the Taylor expansion in R,

$$G_k(R) = \sum_{n=0}^{\infty} \frac{(ik)^n}{n!} R^{(n-1)} \tag{5.2.32}$$

we can see that the kernel in the integral operator equals

$$\sum_{n=0}^{\infty} \frac{(ik)^n}{n!} R^{(n-1)} \left[A(R) + B(R) + C(R) + Q(R)\right] \tag{5.2.33}$$

and that it contains terms of order R^{-3} and R^{-2} (thanks to the terms $A(R), B(R), C(R)$) that cancel when we take a difference of such operators with wavenumbers $k = e, k = d$.

In detail, the term $Q(R)$ contains only terms of order R^{-1}, and more regular. In A, B, C, it is easy to check that the terms of order R^{-3} cancel: the corresponding coefficients do not depend on k in this case. In the terms of order R^{-2}, in turn, an analogous situation to the acoustic case takes place: the corresponding coefficients are multiples of (ik).

Lets write down the terms appearing in A in detail. The difference among two wave-numbers leads to the expressions

$$(A_e - A_d) = \sum_{n=0}^{n} \left[\frac{(ie)^n}{n!} R^{(n-1)} \left(\frac{3 - 3ieR}{R^4} (\mathbf{R} \cdot \mathbf{a})\mathbf{R} \right) - \frac{(id)^n}{n!} R^{(n-1)} \left(\frac{3 - 3idR}{R^4} (\mathbf{R} \cdot \mathbf{a})\mathbf{R} \right) \right] \quad (5.2.34)$$

$$(A_e - A_d) = 3 \sum_{n=0}^{n} \left[\frac{(ie)^n - (id)^n}{n!} R^{(n-3)} - \frac{(ie)^{n+1} - (id)^{n+1}}{n!} R^{(n-2)} \right] \frac{(\mathbf{R} \cdot \mathbf{a})\mathbf{R}}{R^2} \quad (5.2.35)$$

$$(A_e - A_d) = 3 \left(F_e(R) - F_d(R) \right) \frac{(\mathbf{R} \cdot \mathbf{a})\mathbf{R}}{R^2} \quad (5.2.36)$$

where $F_e(R)$ is the same function that appeared in equations (5.2.16) and (5.2.18) of the acoustic case.

To summarize, in order to evaluate the EM Muller operator, it suffices to evaluate $F_e(R) - F_d(R)$ as in the acoustic case, and multiply by the vector magnitudes that appear in (5.2.28).

5.3 Validity of Kirchhoff approximation

The high accuracy attainable by convergent numerical methods, in particular, enables the study of the so-called region of validity of physics-based approximations. For example, in our contribution [38], a detailed comparison between the predictions arising from use of the Kirchhoff's approximation and those resulting from an arbitrarily accurate numerical method, is presented for the case of doubly periodic three-dimensional surfaces.

5.4 Future Work: Summary

This thesis work points to a variety of interesting future research projects, involving more general boundary conditions, time-dependent problems (based on the solution of a large number of time-harmonic problems), the elastic wave equations, and processing of geometries defined via standard CAD specifications.

Bibliography

[1] N. Abatangelo. Large s-harmonic functions and boundary blow-up solutions for the fractional laplacian. *Discrete and Continuous Dynamical Systems*, 35(12):5555–5607, 2015.

[2] M. Abramowitz and I. Stegun. *Handbook of Mathematical Functions*. Dover Publications, 1965.

[3] G. Acosta and J. P. Borthagaray. A fractional Laplace equation: Regularity of solutions and finite element approximations. *SIAM Journal on Numerical Analysis*, 55(2):472–495, 2017.

[4] G. Acosta, J. P. Borthagaray, O. P. Bruno, and M. Maas. Regularity theory and high order numerical methods for the (1d)-fractional laplacian. *Mathematics of Computation*, 2017.

[5] G. Albanese, A. Fiscella, and E. Valdinoci. Gevrey regularity for integro-differential operators. *Journal of Mathematical Analysis and Applications*, 428(2):1225 – 1238, 2015.

[6] T. Arens, S. N. Chandler-Wilde, and J. A. DeSanto. On integral equation and least squares methods for scattering by diffraction gratings. *Communications in Computational Physics*, 1(6):1010–1042, 2006.

[7] T. Arens, K. Sandfort, S. Schmitt, and A. Lechleiter. Analysing ewald's method for the evaluation of Green's functions for periodic media. *IMA Journal of Applied Mathematics*, pages 405–431, 2011.

[8] I. Babuska and B. Guo. Direct and inverse approximation theorems for the p-version of the finite element method in the framework of weighted Besov spaces. part I: Approximability of functions in the weighted Besov spaces. *SIAM Journal on Numerical Analysis*, 39(5):1512–1538, 2002.

[9] W. N. Bailey. *Generalized Hypergeometric Series*. Cambrigde University Press, 1935.

[10] B. B. Baker and E. T. Copson. *The Mathematical Theory of Huygens' Principle*. Oxford University Press, 1939.

[11] A. Barnett and L. Greengard. A new integral representation for quasi-periodic scattering problems in two dimensions. *BIT Numerical mathematics*, 51(1):67–90, 2011.

[12] J. Bergh and J. Löfström. *Interpolation spaces: an introduction*. Springer-Verlag, Berlin, 1976.

[13] C. Brändle, E. Colorado, A. de Pablo, and U. Sánchez. A concave-convex elliptic problem involving the fractional laplacian. *Proceedings of the Royal Society of Edinburgh: Section A Mathematics*, 143:39–71, 2 2013.

[14] S. Brenner and L. R. Scott. *The mathematical theory of finite element methods*, volume 15 of *Texts in Applied Mathematics*. Springer-Verlag, New York, 1994.

[15] O. P. Bruno and B. Delourme. Rapidly convergent quasi-periodic Green function throughout the spectrum - including Wood anomalies. *Journal of Computational Physics*, January 2014.

[16] O. P. Bruno and E. Garza. Rectangular integration method for surface scattering problems in three dimensions. 2018.

[17] O. P. Bruno and M. Haslam. Efficient high-order evaluation of scattering by periodic surfaces: deep gratings, high frequencies, and glancing incidences. *J. Opt. Soc. Am. A*, 26(3):658–668, Mar 2009.

[18] O. P. Bruno and L. Kunyansky. A fast, high-order algorithm for the solution of surface scattering problems: Basic implementation, tests, and applications. *Journal of Computational Physics*, 169:80–110, 2001.

[19] O. P. Bruno and Stéphane K. Lintner. Second-kind integral solvers for TE and TM problems of diffraction by open arcs. *Radio Science*, 47(6):n/a–n/a, 2012. RS6006.

[20] O. P. Bruno and M. Maas. Fast 3D Maxwell solvers for bi-periodic structures, including Wood anomalies. In preparation, 2018.

[21] O. P. Bruno, S. Shipman, C. Turc, and S.Venakides. Superalgebraically convergent smoothly windowed lattice sums for doubly periodic Green functions in three-dimensional space. *Proc. R. Soc. A*, 2016.

[22] O. P. Bruno, S. Shipman, C. Turc, and S.Venakides. Three-dimensional quasi-periodic shifted Green function throughout the spectrum–including Wood anomalies. *Proc. R. Soc. A*, 473(2207):20170242, 2017.

[23] L. Caffarelli and L. Silvestre. An extension problem related to the fractional Laplacian. *Comm. Partial Differential Equations*, 32(7-9):1245–1260, 2007.

[24] F. Capolino, D. R. Wilton, and W. A. Johnson. Efficient computation of the 2-D Green's function for 1-D periodic structures using the Ewald method. *IEEE Transactions on Antennas and Propagation*, 53(9):2977–2984, 2005.

[25] M. Cavendish. *Illustrated Dictionary of the Muslim World*. Marshall Cavendish Corp., New York, 2011.

[26] R. Cecchini and G. Pelosi. Diffraction: the first recorded observation. *IEEE Antennas and Propagation Magazine*, 32(2):27–30, April 1990.

[27] R. Chen and J. C. West. Analysis of scattering from rough surfaces at large incidence angles using a periodic-surface moment method. *IEEE transactions on geoscience and remote sensing*, 33(5):1206–1213, 1995.

[28] D. Colton and R. Kress. *Integral equation methods in scattering theory*. John Wiley and Sons, 1983.

[29] D. Colton and R. Kress. *Inverse acoustic and electromagnetic scattering theory*, volume 93 of *Applied Mathematical Sciences*. Springer, second edition, 1997.

[30] Matteo Cozzi. Interior regularity of solutions of non-local equations in sobolev and nikol'skii spaces. *Annali di Matematica Pura ed Applicata (1923 -)*, pages 1–24, 2016.

[31] H. Crew. *Wave theory of light: Memoires by Huygens, Young and Fresnel*. American Book Company, 1900.

[32] D. Crombie. Doppler spectrum of sea echo at 13.56 mc./s. *Nature*, 175(4459):681, 1955.

[33] M. D'Elia and M. Gunzburger. The fractional laplacian operator on bounded domains as a special case of the nonlocal diffusion operator. *Computers & Mathematics with Applications*, 66(7):1245 – 1260, 2013.

[34] J. DeSanto, G. Erdmann, W. Hereman, and M. Misra. Theoretical and computational aspects of scattering from rough surfaces: one-dimensional surfaces. *Waves Random Med.*, 8(4), 1998.

[35] K. Ding, L. Tsang, J. Kong, C. Ao, and J. Kong. Scattering of electromagnetic waves, numerical simulation. *Remote Sensing*, 2001.

[36] M. Dobson, F. T. Ulaby, M. T. Hallikainen, and M. A. El-Rayes. Microwave dielectric behavior of wet soil-part ii: Dielectric mixing models. *IEEE Transactions on Geoscience and Remote Sensing*, (1):35–46, 1985.

[37] B. Dyda, A. Kuznetsov, and M. Kwaśnicki. Fractional Laplace operator and Meijer G-function. *Constructive Approximation*, pages 1–22, 2016.

[38] M. Franco, M. Barber, M. Maas, O. Bruno, F. Grings, and E. Calzetta. Validity of the kirchhoff approximation for the scattering of electromagnetic waves from dielectric, doubly periodic surfaces. *J. Opt. Soc. Am. A*, 34(12):2266–2277, Dec 2017.

[39] G. H. Golub and C. F. Van Loan. *Matrix Computations (3rd Ed.)*. Johns Hopkins University Press, Baltimore, MD, USA, 1996.

[40] J. D. Gonzalez, E. F. Lavia, M. Maas, and R. Marques Rojo. Scattering acústico 3d de vejigas natatorias de formas arbitrarias: Resultados numéricos. In *Matemática Aplicada, Computacional e Industrial*, volume 6, 2017.

[41] G. Grubb. Fractional Laplacians on domains, a development of Hörmander's theory of μ-transmission pseudodifferential operators. *Advances in Mathematics*, 268:478 – 528, 2015.

[42] B. Guo and L. Wang. Jacobi approximations in non-uniformly Jacobi-weighted Sobolev spaces. *Journal of Approximation Theory*, 128(1):1–41, 2004.

[43] N. Hale and A. Townsend. Fast and accurate computation of Gauss–Legendre and Gauss–Jacobi quadrature nodes and weights. *SIAM Journal on Scientific Computing*, 35(2):A652–A674, 2013.

[44] Y. Huang and A. Oberman. Numerical methods for the fractional laplacian: A finite difference-quadrature approach. *SIAM J. Numer. Anal.*, 52(6):3056–3084, 2014.

[45] J. T. Johnson. A numerical study of low-grazing-angle backscatter from ocean-like impedance surfaces with the canonical grid method. *IEEE transactions on antennas and propagation*, 46(1):114–120, 1998.

[46] R. Kress. *Linear integral equations*. Springer-Verlag, New York, third edition, 2014.

[47] R. Graham L, D. E. Knuth, and O. Patashnik. *Concrete mathematics: a foundation for computer science*. Addison-Wesley Publishing Company, second edition, 1998.

[48] N. N. Lebedev. *Special functions and their applications*. Prentice-Hall, New Jersey, 1965.

[49] D. C. Lindberg. Alhazen's theory of vision and its reception in the west. *Isis*, 58(3):321–341, 1967.

[50] S. K. Lintner and O. P. Bruno. A generalized Calderón formula for open-arc diffraction problems: theoretical considerations. *Proc. Roy. Soc. Edinburgh Sect. A*, 145:331–364, 4 2015.

[51] C. M. Linton. The Green's function for the two-dimensional Helmholtz equation in periodic domains. *Journal of Engineering Mathematics*, 33(4):377–401, 1998.

[52] Y. Liu and A. Barnett. Efficient numerical solution of acoustic scattering from doubly-periodic arrays of axisymmetric objects. *Journal of Computational Physics*, 324:226 – 245, 2016.

[53] A. Macfarlane and G. Martin. *Glass: a world history*. University of Chicago Press, 2002.

[54] J. C. Mason and D. C. Handscomb. *Chevyshev Polynomials*. Chapman & Hall CRC, 2003.

[55] D. Maystre. Rigorous vector theories of diffraction gratings. In E. Wolf, editor, *Progress in optics*, volume XXI, chapter 1, pages 3–65. Elsevier science publishers, 1983.

[56] D. Maystre. Theory of Wood's anomalies. In *Plasmonics*, pages 39–83. Springer, 2012.

[57] R. C. McPhedran, G. H. Derrick, and L. C. Botten. Theory of crossed gratings. In *Electromagnetic Theory of Gratings*, pages 227–276. Springer, 1980.

[58] Thomas Meissner and Frank J Wentz. The complex dielectric constant of pure and sea water from microwave satellite observations. *IEEE Transactions on Geoscience and remote Sensing*, 42(9):1836–1849, 2004.

[59] A. Merzouki, H. McNairn, and A. Pacheco. Mapping soil moisture using radarsat-2 data and local autocorrelation statistics. *Selected Topics in Applied Earth Observations and Remote Sensing, IEEE Journal of*, 4(1):128–137, March 2011.

[60] Jean-Claude Nédélec. *Acoustic and electromagnetic equations: integral representations for harmonic problems*, volume 144. Springer Science & Business Media, 2001.

[61] E. Di Nezza, G. Palatucci, and E. Valdinoci. Hitchhiker's guide to the fractional Sobolev spaces. *Bull. Sci. Math.*, 136(5):521–573, 2012.

[62] Ricardo H. Nochetto, Enrique Otárola, and Abner J. Salgado. A PDE approach to fractional diffusion in general domains: A priori error analysis. *Foundations of Computational Mathematics*, pages 1–59, 2014.

[63] Y. Oh. Quantitative retrieval of soil moisture content and surface roughness from multipolarized radar observations of bare soil surfaces. *IEEE Trans. Geosci. Remote Sens.*, 42(3):596–601, March 2004.

[64] R. Petit. *Electromagnetic theory of gratings*, volume 22. Springer Science & Business Media, 2013.

[65] John William Strutt Baron Rayleigh. *The theory of sound*, volume 2. Macmillan, 1896.

[66] Lord Rayleigh. Note on the remarkable case of diffraction spectra described by Prof. Wood. *The London, Edinburgh, and Dublin Philosophical Magazine and Journal of Science*, 14(79):60–65, 1907.

[67] X. Ros-Oton and J. Serra. The Dirichlet problem for the fractional Laplacian: Regularity up to the boundary. *Journal de Mathématiques Pures et Appliquées*, 101(3):275 – 302, 2014.

[68] W. Rudin. *Principles of mathematical analysis*, volume 3. McGraw-Hill New York, 1964.

[69] Y. Saad and M. Schultz. GMRES: A generalized minimal residual algorithm for solving non-symmetric linear systems. *SIAM Journal on Scientific and Statistical Computing*, 7(3):856–869, 1986.

[70] M. Saillard and G. Soriano. Rough surface scattering at low-grazing incidence: A dedicated model. *Radio Science*, 46(5), 2011.

[71] A. Sei, O. P. Bruno, and M. Caponi. Study of polarization dependent scattering anomalies with application to oceanic scattering. *Radio Science, Volume*, 2(34):385–411, 1999.

[72] R. Servadei and E. Valdinoci. On the spectrum of two different fractional operators. *Proc. Roy. Soc. Edinburgh Sect. A*, 144(4):831–855, 2014.

[73] J. E. Stewart and W. S. Gallaway. Diffraction anomalies in grating spectrophotometers. *Applied Optics*, 1(4):421–430, 1962.

[74] J. A. Stratton and L. J. Chu. Diffraction theory of electromagnetic waves. *Phys. Rev.*, 56:99–107, Jul 1939.

[75] G. T. Symm. Integral equation methods in potential theory. ii. *Proceedings of the Royal Society of London A: Mathematical, Physical and Engineering Sciences*, 275(1360):33–46, 1963.

[76] G. Szegö. *Orthogonal polynomials, Fourth Edition*. American Mathematical Society, Colloquium publications, 1975.

[77] L. Tsang, Ja Kong, Kh Ding, and Ao Co. *Scattering of electromangetic waves. 3 volume set*. John Wiley and Sons, 2001.

[78] E. Valdinoci. From the long jump random walk to the fractional Laplacian. *Bol. Soc. Esp. Mat. Apl. S͡eMA*, 49:33–44, 2009.

[79] J. Waldvogel. Fast construction of the fejér and clenshaw–curtis quadrature rules. *BIT Numerical Mathematics*, 43(1):1–18, 2003.

[80] R. W. Wood. On a remarkable case of uneven distribution of light in a diffraction grating spectrum. *The London, Edinburgh, and Dublin Philosophical Magazine and Journal of Science*, 4(21):396–402, 1902.

[81] J. W. Wright. A new model for sea clutter. *IEEE Transactions on antennas and propagation*, 16(2):217–223, 1968.

[82] Z. Xie, L. Wang, and X. Zhao. On exponential convergence of Gegenbauer interpolation and spectral differentiation. *Mathematics of Computation*, 82(282):1017–1036, 2013.

[83] Y. Yan and I.H. Sloan. On integral equations of the first kind with logarithmic kernels. *J. Integral Equations Applications*, 1(4):549–580, 12 1988.

[84] H. A. Yueh, R. T. Shin, and J. A. Kong. Scattering of electromagnetic waves from a periodic surface with random roughness. *Journal of Applied Physics*, 1657(64), 1988.

[85] X. Zhao, L. Wang, and Z. Xie. Sharp error bounds for Jacobi expansions and Gegenbauer–Gauss quadrature of analytic functions. *SIAM Journal on Numerical Analysis*, 51(3):1443–1469, 2013.